A SHIFT-VARIANT RESTORATION TECHNIQUE LEVERAGING HIGH-RESOLUTION INTERFACE MODELING IN LIDAR-BASED SEAFLOOR IMAGING

A Thesis
Presented to
The Academic Faculty

by

Domenic A. Carr

In Partial Fulfillment
of the Requirements for the Degree
Doctor of Philosophy in the
School of Electrical and Computer Engineering

Georgia Institute of Technology
August 2016

A SHIFT-VARIANT RESTORATION TECHNIQUE LEVERAGING HIGH-RESOLUTION INTERFACE MODELING IN LIDAR-BASED SEAFLOOR IMAGING

Approved by:

Dr. Gisele Bennett, Advisor
School of Electrical and Computer Engineering
Georgia Institute of Technology

Dr. Grady Tuell, Co-Advisor
Georgia Tech Research Institute
Georgia Institute of Technology

Dr. Jennifer Michaels
School of Electrical and Computer Engineering
Georgia Institute of Technology

Dr. Thomas Michaels
School of Electrical and Computer Engineering
Georgia Institute of Technology

Dr. George Vachtsevanos
School of Electrical and Computer Engineering
Georgia Institute of Technology

Dr. Brian Gunter
School of Aerospace Engineering
Georgia Institute of Technology

Date Approved: 13 May 2016

To my parents, for their unconditional love and unfailing support.

ACKNOWLEDGEMENTS

It is only appropriate to start by thanking my co-advisors, Dr. Gisele Bennett and Dr. Grady Tuell. Without their patience and support, this dissertation would not be possible. I am so thankful that Dr. Bennett offered me a research assistantship at EOSL. My decision to attend Georgia Tech was a direct result of that offer, and these past five years have been truly rewarding. She has helped provide me with a well-rounded graduate experience in which I have served in student leadership positions and attended various conferences, to name just a few opportunities she made possible. Likewise, Dr. Tuell has helped make my experience at EOSL very rewarding. Four years ago, he took me under his wings and patiently allowed me to learn the intricacies of airborne lidar bathymetry. I am so thankful for the countless hours he provided, during and outside of work, to help me complete this research. His efforts have far exceeded normal expectations, and the researcher I have become is undoubtedly due to his teaching and support.

Next, I would like to thank Dr. George Vachtsevanos for his instrumental role in my working at EOSL. When I first arrived at Georgia Tech, he agreed to meet with me and shortly thereafter provided a recommendation on my behalf to Dr. Bennett. Without the role he played, my graduate school experience would have been completely different.

To my proposal and defense reading-committee members, Dr. Jennifer Michaels, Dr. Tom Michaels, and Dr. Vachtsevanos, thank you all very much for the time you spent reviewing my research. Your instructive feedback was an essential part of the way I investigated this research problem, and it greatly enhanced the work.

To all my colleagues at EOSL, especially those on the AEO-ISR IRAD, thank you

all so much for your enthusiasm and support. Building Pathfinder and BRDL was the collective result of over 25 of us working together in a unified way. My research, leveraging Pathfinder's unique capabilities, would not have been possible without each of your contributions. Special thanks to several of you who worked directly with me: to Robert Ortman, thank you for your dedicated efforts in building an incredible real-time processing engine and for your invaluable assistance debugging various Bathy-m problems; to Eric Brown, in addition to all your amazing design work, thank you for all the extra time you put in making sure experiments at the water tank went as smoothly as possible; to Ryan James, thank you for all your various contributions to Pathfinder's hardware and software, and for your enthusiasm that helped keep me thinking positively; to Nicholas Guida, thank you for your efforts working with the GmAPD camera and helping perform the water tank experiments; to Matthew O'Shaughnessy, thank you for your efforts working with Bathy-m and with the witness camera, and for helping perform the water tank experiments; to Jack Wood, thank you for your optical engineering efforts, helping turn Pathfinder into the world's first hybrid lidar; to Christopher Valenta, thank you for your excellent detector and amplifier work; and to Daniel Long, thank you for your efforts with the real-time computing engine's GPU.

Thank you to all the people who strongly suggested I use LaTex for this document. I cannot even imagine how many hours or weeks that decision saved me. Special thanks to Keith Prussing who organized such a great template and made it available on GitHub. Keith, along with Christopher Valenta, provided very helpful insights on how to fix problems I was experiencing, which saved a lot of time. Thank you both for your assistance with LaTex.

Thank you to Georgia Tech's Mechanical Engineering Department for allowing EOSL to perform experiments at the Love Building's Water Tank Facility. Special thanks to Michael Gray and James Martin who were very welcoming hosts and very

accommodating with our changing schedules.

Thank you to all the pioneers of the field of airborne lidar bathymetry. Your contributions helped pave the way for researchers like me to learn about the technology. I would especially like to thank Dr. Gary Guenther for all of his contributions. His research presented in "the blue book" and his subsequent publications helped established my foundation in the field.

I would like to acknowledge the various organizations that funded the path leading to my degree: GTRI, for providing three years of AEO-ISR IRAD funding; NOAA/Dewberry, for providing funds to perform wavy water experiments; and, EOSL for providing one year of funding intended for me to complete this research.

To my parents, no words can adequately express the depth of my thanks. You are my biggest supporters. Even from afar, your love has buoyed my success. During my moments of doubt, you continually instilled confidence in me, helping me overcome any adversity. I would not be where I am today without both of you. Thank you, both, from the bottom of my heart.

To my loving yiayia, who passed away before seeing me accomplish this, thank you for all the wonderful years we enjoyed together. Her personality is forever etched within me and I carry her memory wherever I go.

To my loving grandparents, Raymond and Carolyn, thank you for all your love and support over the years. You both are such an inspiration to me and to the rest of our family. I am so proud to be your grandson.

To all my other family and friends, thank you so much for continually supporting me during this long academic adventure. Each of you played an important role during this trek, knowingly or not, and I sincerely thank you.

Finally, and most importantly, I would like to thank my Lord and Savior, Jesus Christ. Through Him all things are possible, and it is only through His blessings that I have produced this document and completed this degree.

TABLE OF CONTENTS

LIST OF TABLES

LIST OF FIGURES

LIST OF SYMBOLS OR ABBREVIATIONS

cm	centimeter.
Hz	Hertz.
kHz	kilohertz.
m	meter.
$mrad$	mrad.
ms	millisecond.
MW	Megawatt.
nm	nanometer.
ns	nanosecond.
ps	picosecond.
W	Watt.
3D	Three-dimensional.
ALB	Airborne Lidar Bathymetry.
BLTF	Bathymetric-Lidar Transfer Function.
BRDL	Bantam Real-time Dual-use Lidar.
COTS	Commercial-off-the-shelf.
CPU	Central Processing Unit.
CZMIL	Coastal Zone Mapping and Imaging Lidar.
DARPA	Defense Advanced Research Projects Agency.
DSM	Digital Surface Model.
ENOB	Effective number of bits.
EOSL	Electro-Optical Systems Laboratory.
FOV	Field-of-view.
FPA	Focal plane array.
FPGA	Field-programmable Gate Array.

FWHM	Full-width Half Maximum.
GmAPD	Geiger-mode Avalanche Photodiode.
GPS	Global Positioning System.
GPU	Graphics Processing Unit.
GT	Georgia Tech.
HDF	Hierarchical Data Format.
IBF	Inertial body frame.
IHO	International Hydrographic Organization.
IMU	Inertial Measurement Unit.
IR	Infrared.
JALBTCX	Joint Airborne Lidar Bathymetry Technical Center of Expertise.
LADAR	Laser Detection and Ranging.
LADS	Laser Airborne Depth Sounder.
LAS	LASer file format.
LGF	Local geodetic frame.
LIDAR	Light Detection and Ranging.
Nd:YAG	Neodymium-doped Yttrium Aluminum Garnet.
NED	Northing, Easting, and Down.
NGA	National Geospatial-Intelligence Agency.
OLS	Ordinary Least Squares.
PCA	Principal Component Analysis.
PMT	Photomultiplier tube.
SBF	Sensor body frame.
SHOALS	Scanning Hydrographic Operational Airborne Lidar Survey.
SST	Sea Surface Topography.
SWAP	Size, weight, and power.
TIA	Transimpedance amplifier.

TMS	Thermal Management System.
TOF	Time-of-flight.
TPU	Total Propagated Uncertainty.
UAV	Unmanned aerial vehicle.
USACE	United States Army Corps of Engineers.
USGS	United States Geological Survey.

SUMMARY

Airborne-lidar bathymetry systems provide intelligence, surveillance, and reconnaissance capabilities reliably and cost-effectively in coastal areas. Recently, systems have shown the ability to produce seafloor reflectance imagery. This imagery depends on the accuracy of seafloor coordinates and reflectance estimates comprising them. One accuracy-limiting factor is wavy sea surface topography, affecting seafloor reflectance images in two ways. First, images are geometrically distorted by uncompensated beam steering; second, images are radiometrically distorted by uncompensated pulse stretching. These two interface-induced distortions manifest themselves as image blur. This thesis presents a restoration technique addressing both of these distortions, treating them as the effects of a shift-variant linear system. This system's transfer function may be identified for each laser pulse by using a novel, hybrid-lidar processing architecture combining Geiger-mode and waveform-resolved systems' data. In this architecture, high-resolution interface models constructed from Geiger-mode system measurements are registered with co-temporal waveforms, enabling ray tracing through wavy interfaces and identifying interface-induced pulse stretching. Seafloor coordinates may then be geometrically reconstructed and reflectance estimates may be radiometrically restored. Unifying these two aspects into one restoration procedure significantly enhances the resolution of seafloor reflectance images degraded by wavy sea surface topography.

CHAPTER I

INTRODUCTION

Airborne lidar bathymetry (ALB) is a fascinating remote-sensing technique used to measure water depth in coastal and littoral areas. A high-power laser transmits pulsed beams of light from an aircraft hundreds of meters above the water and the system's receiver measures the resulting backscattered energy from each pulse as a function of time. ALB systems operate similarly to their topographic counterparts, but have the added complexity of accounting for refraction at the air-water interface, dealing with extensive scattering during the pulse's propagation in water, and handling returned powers spanning many orders of magnitude in a very short period of time. The design space for ALB systems is vast; to design, build, and operate effective systems requires multi-disciplinary cooperation between electrical, mechanical, optical, and computer engineers. The research reported in this thesis centers on the largely unaddressed problem of robustly compensating for sea surface effects when using ALB to image the seafloor. A unique aspect of the research is the development of a novel ALB processing architecture that combines two seemingly disparate modes of lidar, Geiger and linear, into one, hybrid system. This thesis shows that such a system can effectively compensate for wavy sea surfaces, thereby improving the quality of and extending the operational window of lidar-based seafloor imaging.

This chapter introduces ALB and details system development over time. This is done to motivate why systems need to account for sea surface effects when imaging the seafloor, which is the focus of this thesis. The chapter begins with a historical background of ALB, discusses the current trends in the ALB community, and concludes with an overview of the research presented in this document.

1.1 Historical Background

The field of ALB is a subset of a larger field known as Light Detection and Ranging (LIDAR) or Laser Detection and Ranging (LADAR). LIDAR, LADAR, laser radar, and all of the various various ways of capitalizing lidar (e.g. LiDAR, LIDAR, or Lidar) refer to the same concept of illuminating a target scene with a laser and then measuring the backscattered energy with a photodetector. Lidar research began in the 1960's when the newly invented laser was combined with radar principles [1]. The motivation was to leverage a laser's shorter wavelength to detect smaller features [2]. From this research, three main types of lidar technology developed: (1) range-finding, (2) differential absorption, and (3) Doppler [2]. ALB is a range-finding technique.

Range-finding lidars operate by measuring the time-of-flight (TOF) difference between a transmitted laser pulse and the backscattered return signal. By accounting for positional information and pointing configuration, 3D coordinates corresponding to the origin of the backscattered signal may be computed. A coordinate point cloud of the surveyed area, as seen in Figure 1, may then be produced by scanning the laser and aggregating the computed coordinates. Lidars can be stationary or mobile when performing TOF measurements; ALB systems are mobile. Such systems must actively monitor and record their position and orientation while operating to produce accurate point clouds. The two main branches of airborne lidar are topographic (on-land measurements) and bathymetric (water depth measurements).

ALB is a relatively young technology. In 1969, Hickman and Hogg produced the field's seminal work confirming a laser's ability to perform coastal bathymetry [3]. Their work was made possible from prior research in that decade investigating a laser's potential to detect submarines [4, 5]. Since then, ALB has grown and evolved. Guenther provides a detailed history in [6] of ALB system development in various countries through the year 2000. Guenther's account can be summarized as follows: the first ALB systems were successfully tested in the early 1970's in the

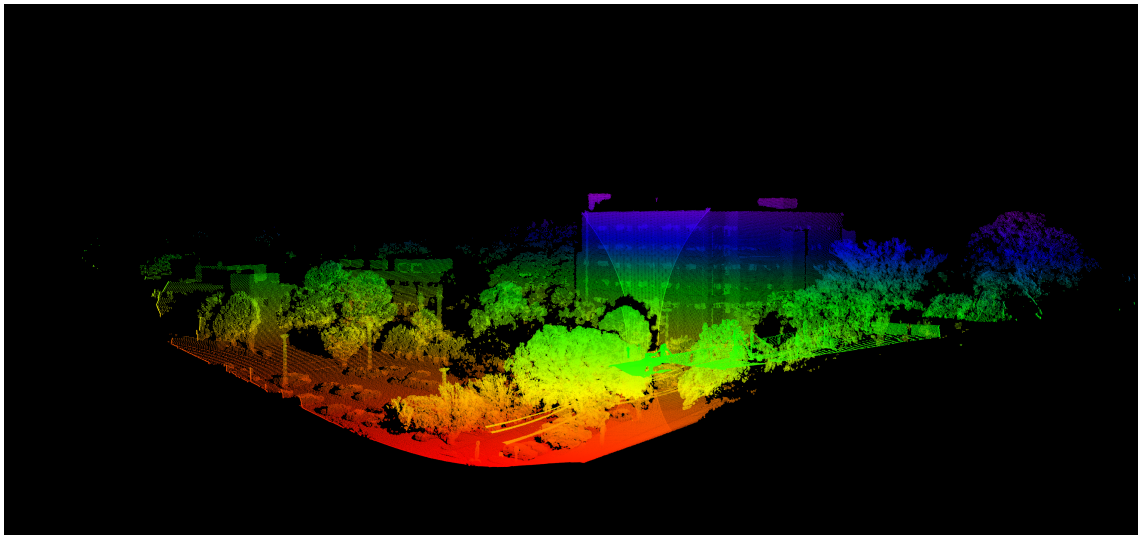

Figure 1: A topographic point cloud, produced by GTRI's Bantam Dual-use Real-time Lidar (BRDL), contains thousands of coordinates corresponding to individual TOF measurements.

United States [7, 8], Canada[9], and Australia [10]; in the 1980's, Canada's Larsen-500 system [11] became the first operational airborne bathymeter; in the 1990's, the United States' SHOALS system [12], Australia's LADS system [13], and Sweden's Hawk Eye system [14] became operational as well. Since the year 2000, updated versions of these systems have been deployed along with many new systems. Figure 2, using information from [6], [15], and [16], shows a condensed history and timeline of ALB research and system development from 1969 to 2015. Listed systems are arranged by the country that originated the system's development, not by where the system was built. For example, SHOALS is grouped in the U.S.A. box even though it was built in Canada because the United States Army Corps of Engineers (USACE) commissioned its development.

ALB adoption and proliferation occurred for three main reasons. First, ALB systems have faster area-coverage rates than shipborne systems, making them a quick and cost-effective surveying technique. It has been shown that ALB systems can reduce the cost of coastal surveys by 50 to 80 percent [6]. Second, ALB systems can perform safer surveys of shallow water areas because they do not have to account for

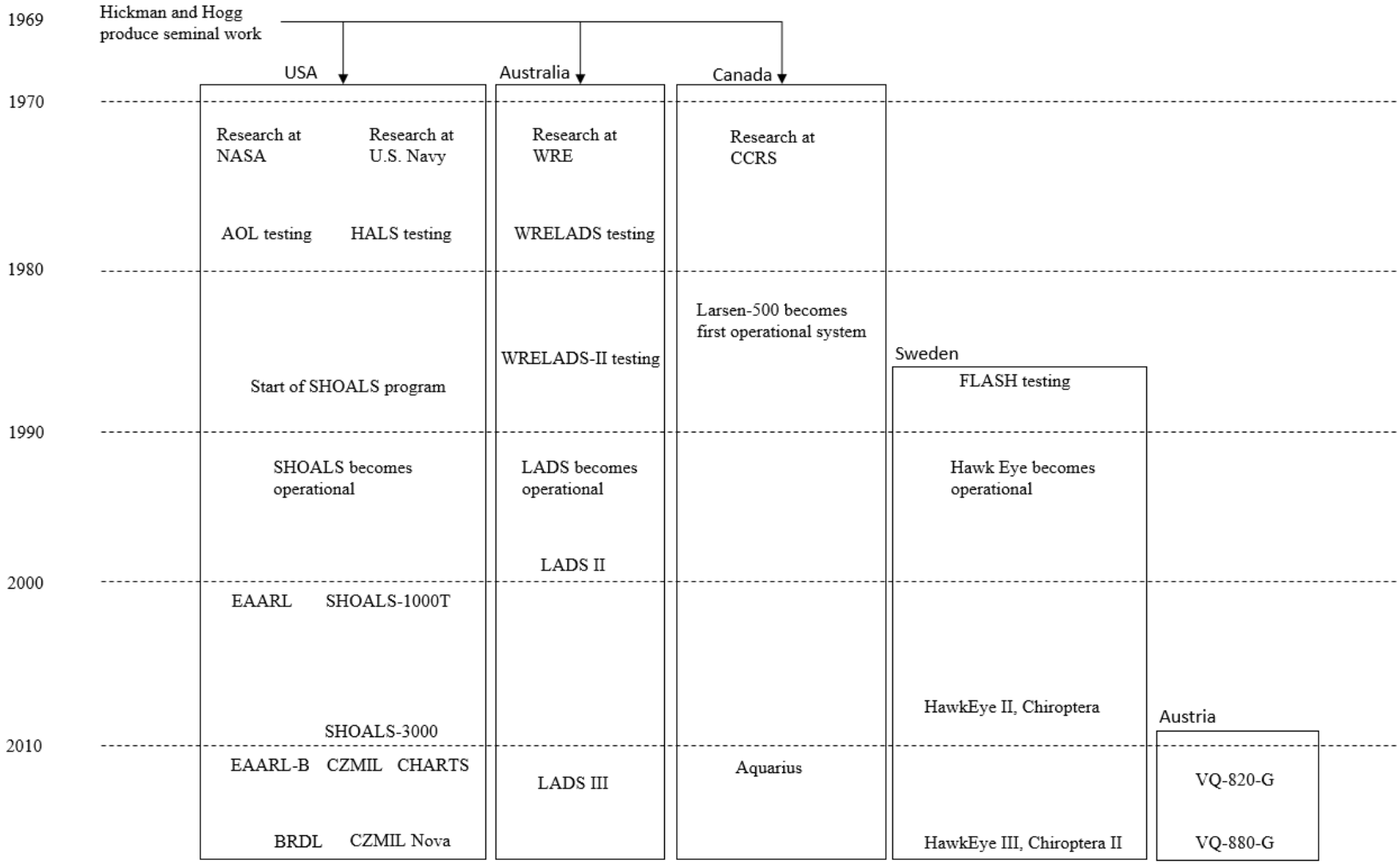

Figure 2: A condensed history of ALB system research and development from 1969 to 2015.

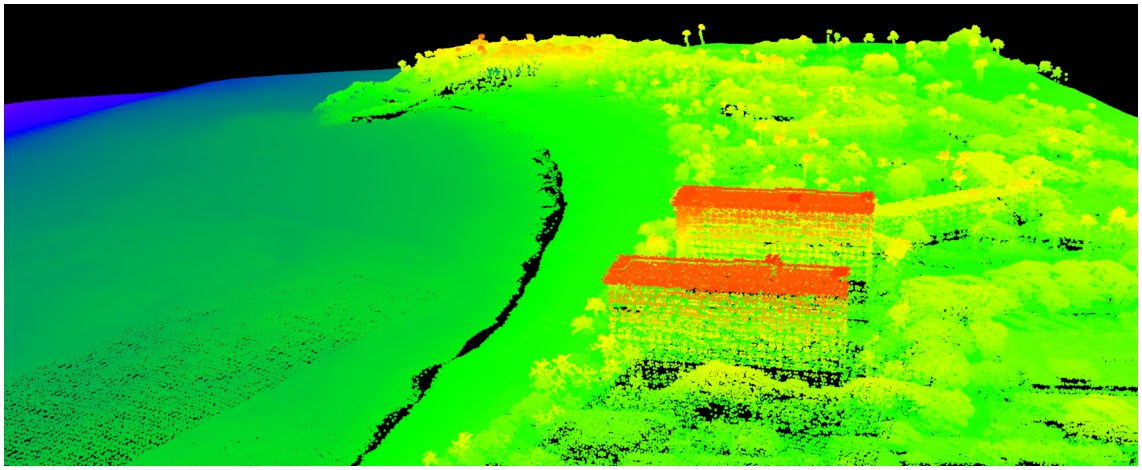

Figure 3: A coastal point cloud, produced from CZMIL data, contains nearly seamless topographic and bathymetric measurements.

the underwater obstructions or dangers that shipborne systems must avoid. Third, ALB systems can survey extremely shallow waters, areas unreachable by shipborne systems, and can survey the adjoining beach and land areas. This final reason is very important because ALB point clouds do not need to be stitched together with land-only, topographic-system point clouds. Instead, ALB systems can produce a complete point cloud of the entire coastal area, providing a near-seamless transition between bathymetric and topographic data. Figure 3 shows an example of such a point cloud, produced from data collected by the Coastal Zone Mapping and Imaging Lidar (CZMIL) in Maui, Hawaii [1].

Once ALB systems showed their surveying potential, the main catalyst for system progress was improvements in laser, electronics, and optics technologies. Early systems struggled to detect the water surface reliably, causing depth measurement biases from incorrect compensation of the beam's changes in direction and speed [17]. Additionally, very shallow waters presented challenges because surface and floor returns blended together, resulting in measurement dropouts at the shoreline [18]. Shaped by these challenges, later systems began utilizing lasers with shorter pulse

[1] JALBTCX provided GTRI with LAS data collected from a 2012 CZMIL collection campaign, from which I created the point cloud using GTRI software and algorithms.

widths, integrating new electronics that reduced system response times, and developing new shallow-water depth algorithms to improve surface detection reliability and shallow water performance [19]. In the early 2000s, newer systems began incorporating emerging global positioning system (GPS), inertial measurement unit (IMU), and spectrometer technologies to improve system accuracy and to yield new data products for applications such as environmental-monitoring [20, 21] and counter-mine detection [22]. Data produced by these more complex systems was geo-referenced and fused with hyperspectral measurements, resulting in the first ALB-produced coastal imagery [23, 24].

1.2 Current Trends

At the time of this thesis, the field of airborne lidar as a whole is rapidly evolving. The community's vision is to reduce system size, weight, and power (SWAP), potentially moving systems from their current platforms (e.g. twin-prop planes) to smaller aircraft, such as unmanned aerial vehicles (UAVs), and achieve greater coverage rates by flying higher. Consequently, a new mode of lidar operation has developed – Geiger-mode. Geiger-mode is a high-sensitivity, low-power mode of operation [25]. Instead of producing TOF measurements from individual laser beams, as is done in traditional, linear-mode systems, Geiger-mode systems produce TOF measurements from individual photons. These systems pulse more quickly and transmit less power per pulse than linear-mode systems [26]. Furthermore, they are usually array-based, producing thousands of TOF measurements per pulse [26]. As a result of these differences, Geiger-mode systems have higher area-coverage rates and higher point densities than linear-mode systems. Undoubtedly, interest in this new technology has grown considerably in recent years.

Geiger-mode technology has not yet entered the field of ALB however. The principal reason is that there are no commercially-available, Geiger-mode detectors that

operate in green wavelengths, the operational wavelength of ALB systems. There is a DARPA-sponsored, green, Geiger-mode system called Jigsaw that is used for foliage-penetration applications [27], but there are no published results of bathymetric testing. Nonetheless, the field of ALB is rapidly evolving as well. A number of new ALB systems have emerged (e.g. Optech's CZMIL and Aquarius; AHAB's Hawkeye III and Chiroptera; the United States Geological Survey (USGS) EAARL-B, and Riegl's VQ-820-G), introducing new approaches to data collection, management of dynamic range, and computation of coordinates. Interestingly, most of the new advances have required increases in SWAP, contradicting the trend present in the general LIDAR community. For example, Optech's CZMIL, weighing 837 pounds and requiring 100 amps at 28 volts [28], replaced the SHOALS-3000 system, which weighed 478 pounds and required 80 amps at 28 volts. Other new systems exhibit similar SWAP increases from their predecessors. This contradictory trend can be explained by an ALB system's need to satisfy the following requirements simultaneously:

(1) detecting the water surface reliably;

(2) managing over six orders of magnitude in returned powers; and,

(3) meeting accuracy and point density requirements.

Reliable surface detection generally has required a multi-wavelength approach because green wavelengths penetrate the water surface unsystematically before producing a detectable signal [18]. EAARL-B, VQ-820G, and LADS-III, green-only systems, are the lone exceptions. Fortunately, using additional receivers is only required to rectify this problem. Systems may use a Raman channel, detecting red returns produced by green wavelength interaction with water molecules, or an infrared channel, using the green laser's fundamental output (e.g. 1064 nm for a frequency-doubled Nd:YAG laser) that barely penetrates the water surface. The latter has become the predominant method for surface detection [6], but in either case, dedicated analog-to-digital

converters (hereafter called digitizers) for each receiver must be used, adding to systems' SWAP.

ALB systems must be able to process strong topographic returns in addition to deep, weak bathymetric returns to enable seamless transitions between topography and bathymetry. Processing these extremes, and the six orders of magnitude between them, must occur within the span of several hundred nanoseconds. Multiple strategies for doing so have emerged. The first method involves using logarithmic compression, either on the amplifier [17] or on the detector [29], to compress the signal into a manageable dynamic range for the digitizer. The second method involves partitioning the full dynamic range into smaller, manageable segments and using different receivers for each one [17]. The third method involves using multiple lidars in a single integrated system, having each lidar specialized for one task (e.g. topography, shallow-water, deep-water, etc.) [30]. Each of these methods, or combinations of these methods, have been employed in newer systems, requiring high-power lasers with short pulse widths and high repetition rates, receivers with high front-end bandwidth and gain, and digitizers with high sampling rates and bit depth. The result of these changes has been an increase in system SWAP.

Meeting accuracy and point density requirements is inherently tied to the issues discussed in the previous two paragraphs. Consequently, the same hardware additions used to solve those problems also help ALB systems meet their accuracy and point density requirements. Systems will not produce accurate depth measurements without reliable surface detection and they will not meet point density requirements if they cannot manage the dynamic range of returned powers appropriately. However, other system-level design choices such as pulse repetition rate, scanning rate and pattern, and receiver area and field-of-view also affect systems' SWAP. For example, CZMIL introduced a circular scanning pattern [31], quickly followed by HawkEye III's similar elliptical scanning patterns [30], increasing point density at the cost of higher

mechanical and optical complexity [16]. In general, system-level design decisions and improvements requiring additional SWAP have been integrated into systems because of their accuracy and point density payoffs. For example, these design goals have led to using high-power (30 W), diode-pumped, solid-state lasers, requiring liquid cooling; the thermal management systems (TMS) for these lidars may add as much as 150 pounds to the system's weight [28]. However, despite progress in ALB system design that has improved performance, an important problem common to all systems that has not been widely discussed is the robust compensation for sea surface effects when computing 3D coordinates of seafloor returns. This thesis helps address that problem.

ALB systems must meet exacting accuracy requirements for nautical charting applications. These requirements are stated in terms of the 3D positional accuracy of the point clouds, and are computed by propagating uncertainties from the measurements onto the coordinates [32]. These assessments are usually computed *a posteriori* by comparing the lidar points to those surveyed with shipborne acoustic systems [33]. Such comparisons yield bulk accuracy assessments for entire data collection campaigns or for specific areas of interest within them. In light of the National Geospatial-Intelligence Agency (NGA) recently mandating 3D uncertainty assessments for every lidar point [34], the current assessment method has two drawbacks. First, it is slow, which can be costly. Ships must scan the surveyed area acoustically to verify the airborne measurements, and if the surveyed data is unacceptable, it must be discarded and the survey re-performed. Second, this method provides no way to identify or quantify the contributions to seafloor coordinate error from individual aspects of the system and the environment. This latter aspect is important to my research, as there is no current way to assess the effect of air-water interface uncertainty on seafloor coordinate error. This thesis introduces a new, and faster, way to perform accuracy assessments for every lidar point even in the presence of sea surface waves.

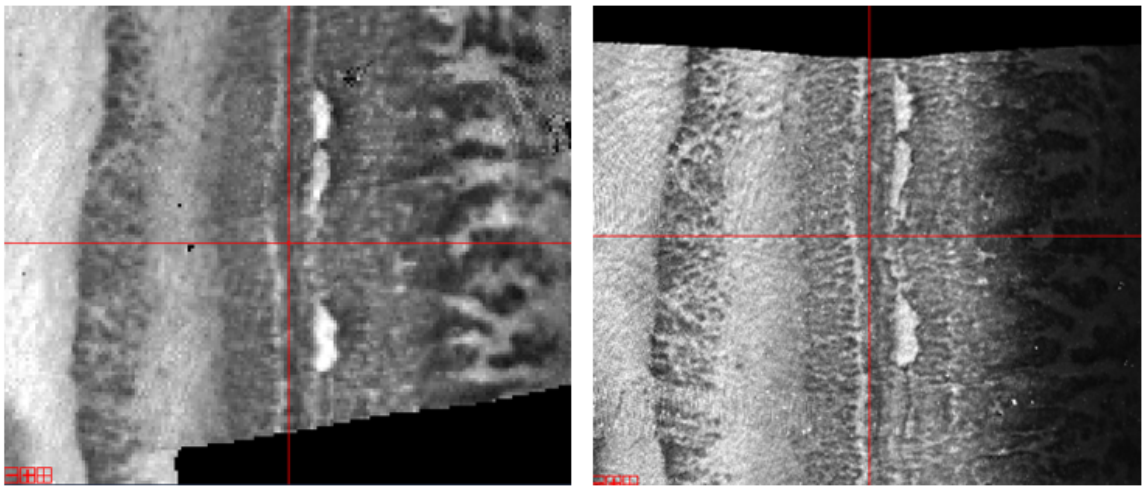

Figure 4: The resolution of seafloor reflectance imagery has improved from 3-meters per pixel (left) to 1-meter per pixel (right) as ALB system accuracy has improved.

As ALB systems have become more accurate, seafloor image resolution has improved as well. The first true, seafloor-reflectance image was produced in 2007 by SHOALS off the coast of Fort Lauderdale, Florida [35]. This image had a resolution of 3 meters per pixel. In 2012, CZMIL performed the same survey as SHOALS and produced a new image with 1-meter-per-pixel resolution [36]. Figure 4 shows these two images side-by-side [2]. Clearly, CZMIL's 1-m resolution image is sharper than the SHOALS image, resolving smaller features on the seafloor. This capability, and future improvements to it, is highly applicable to the military and to environmental groups interested in surveying the near-shore seafloor. This thesis, introducing geometric and radiometric corrections of sea surface effects in seafloor returns, will continue the trend of enhancing seafloor image resolution.

1.3 Research Overview

The objective of this research was to develop a restoration technique for lidar-based seafloor imaging that compensates for irregular air-water interfaces. Irregular interfaces, which contain arbitrary low- and high-frequency content, steer and disperse

[2] This figure was made by editing the original from [36].

lidar-transmitted laser pulses in ways flat (regular) interfaces do not. Uncompensated steering and dispersion can degrade reflectance-image quality by introducing seafloor-coordinate and reflectance-estimation errors. Current ALB systems do not compensate for these errors when producing seafloor reflectance images, resulting in images susceptible to interface-induced artifacts. The restoration technique detailed in this work compensates for steering and dispersion introduced by irregular interfaces at the waveform level for each transmitted pulse, thereby improving the accuracy of each seafloor coordinate and reflectance estimate. The reflectance images produced from these seafloor coordinates and reflectance estimates contain fewer interface-induced artifacts, resulting in higher quality seafloor images. The following chapters detail how this is accomplished.

Chapter 2 presents the fundamentals of ALB. It contains a discussion of system architecture and all of the important components required for successful operation. It also presents the current math models for seafloor coordinate computation and seafloor reflectance estimation. Finally, it details the newest method for assessing 3D coordinate accuracy.

Chapter 3 presents the new, hybrid lidar system and its novel, seafloor-imaging capabilities. It explains how a Geiger-mode lidar and a linear-mode lidar, when combined into one system, may measure continuous variation of sea surface topography (SST) and use those measurements to improve linear-mode system accuracy. It contains derivations of new math models to compute seafloor coordinates, seafloor reflectance estimates, and 3D coordinate uncertainty. These new math models may be viewed as replacements for their respective counterparts in Chapter 2.

Chapter 4 details the experiments performed with the new system and documents the results.

Chapter 5 concludes the thesis, summarizing the original contributions and offering directions for future work.

CHAPTER II

FUNDAMENTALS OF AIRBORNE LIDAR BATHYMETRY

This chapter introduces ALB system operation, showing how seafloor coordinates may be computed, seafloor reflectance may be estimated, and systems' accuracy may be assessed. This enables identifying and discussing each math model's limitations during wavy conditions. The chapter begins by detailing ALB systems' major components and their purposes. The chapter then discusses how ALB measurements may be used to compute seafloor coordinates and estimate seafloor reflectance, which are the two main features of seafloor images. Finally, the chapter discusses how system accuracy is assessed.

2.1 System Architecture

ALB systems are highly complex systems integrating cutting-edge electronic, optical, mechanical, laser, and software technologies to produce intelligence, surveillance, and reconnaissance capabilities in shallow coastal waters. These aircraft-based systems transmit laser pulses in a fixed scanning pattern as the aircraft moves. Each transmitted pulse propagates to the air-water interface and is partially reflected and transmitted according to Maxwell's equations. The transmitted beam refracts into the water and propagates to the seafloor where it is partially reflected and absorbed depending on seafloor composition. The water's inherent optical properties affect the spread and decay of the propagating pulse in water; Figure 5 shows their effects during underwater propagation [37][1]. Throughout the pulse's round-trip propagation, the receiving optics collect backscattered photons returned within the telescope's

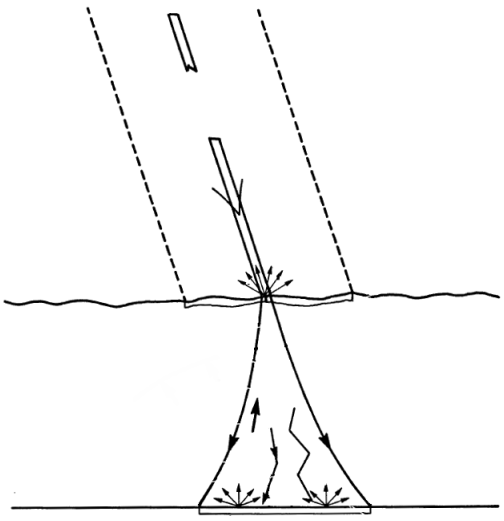

Figure 5: As it propagates to the seafloor, the refracted laser pulse is absorbed and scattered into an increasing cone whose shape is determined by the water's inherent optical properties.

field of view (FOV). Wavelength-specific detectors, usually avalanche photodiodes or photomultipler tubes, convert the photons into electrical current [29]. Processing this electrical signal is system-specific, and two types of processing paradigms exist: waveform-resolved and TOF. For both cases, the goal of system processing is to decompose the signal into in-air and in-water ranges [6]. These ranges may then be time-synchronized with GPS and IMU data from the aircraft to compute sea surface and seafloor coordinates [6]. Aggregating these coordinates produces 3D point clouds containing valuable information about the surveyed area.

ALB systems consist of a laser transmitter and its associated transmitting optics, a scanning mechanism, a receiver telescope and its associated receiving optics, a photon detector, a signal processor, GPS and IMU devices, and dedicated computer hardware and software. All these instruments and devices are integrated into an aircraft flying 200-500 meters above the water surface [6]. Device timing and synchronization is paramount for successful operation, as each subsystem operates at a different rate. This difference can be orders of magnitude in some cases. For example, GPS and

[1]This figure was made by editing the original from [37].

IMU subsystems may produce data at a rate of 200 Hz, while the laser may operate at a rate of 10 kHz. Despite data rate differences, systems must be able to record correct data across subsystems each time the laser transmits a pulse to compute the backscattered energy's origin accurately. Thus, a dedicated timing unit controls system timing and synchronization. The following paragraphs discuss each subsystem on the pulse's path in more detail.

The laser transmitter, pulsed thousands of times per second, samples the coastal area beneath the aircraft in a fixed pattern set by the scanning mechanism. The laser transmits a pulse each time it receives a synchronized trigger signal from the central timing unit. The system must then record the laser's firing time, known as t0, with sub-nanosecond accuracy to enable range estimation to the water surface. To maximize depth penetration, ALB systems use green wavelengths because the diffuse attenuation coefficient, K_D, which defines the pulse's exponential decay during water column propagation, is close to its spectral minimum in that wavelength region for coastal water types [38]. While these wavelengths are not optimal for depth penetration in clear ocean waters or extremely turbid waters, frequency-doubled Nd:YAG lasers produce 532-nm light cheaply and reliably, representing a good compromise for most waters. The laser must also be high energy, have short pulse duration, and have a high repetition rate to satisfy survey resolution requirements [31, 39]. Commercially-available lasers that best fit these characteristics are solid-state infrared lasers that can be frequency-doubled to produce the desired green pulse. ALB systems employing such lasers typically transmit approximately 1 MW of peak power per pulse [40]. This power level is necessary because the airborne receiver captures only a very small portion of the backscattered signal and because the laser beam's attenuation in coastal seawater is relatively high. A consequence of this, though, is that systems' transmitting optics must diverge the beam to a spot size of approximately 3 meters at the water surface to comply with eye safety regulations. The implications of this

are discussed when detailing the receiver subsystem.

The system's scanner is responsible for scanning the transmit beam in a repeated pattern. The pattern's width, shape, and period considerably affect a system's area coverage and point density [31]. Typically, ALB systems employ fixed, off-nadir patterns to create a consistent, wide, coverage swath; the off-nadir angle itself is system-specific. A common choice is 20 degrees, which reduces sea surface return and maximizes transmission into the water [41]. Systems using this off-nadir angle and operating at an altitude of 400 meters can attain a maximum swath diameter of 290 meters. Aircraft motion creates scan coverage in the direction of travel. Assuming an aircraft velocity of 70 meters-per-second, area coverage rates surpass 20,000 square meters per second! Clearly, this coverage rate represents a major advantage over shipborne systems, which travel much slower and have much smaller swath diameters. Pattern shape and period vary across systems. Until recently, the most common scan pattern was a forward-looking arc, but now circular and elliptical patterns have become increasingly popular because of their higher point densities [31, 16]. Regardless of pattern, the scanner's rotation angle about the nadir axis must be encoded with high accuracy so that its orientation can be determined each time the laser transmits a pulse.

During pulse propagation, ALB systems' receiving optics collect photons within the telescope's FOV. Good receivers should be very efficient, should mitigate background noise to enable detection of deep, weak bathymetric returns, and should assist in managing the wide dynamic range of returned powers [29]. Often, ALB systems operate coaxially; the transmit and receive paths are nearly identical. Thus, systems' optical efficiency is essentially the round-trip transmission through the optics, meaning signal loss is proportional to the one-way, optical-efficiency squared. Polishing mirrors, reducing vignetting, and using a high-transmission scanner are the best ways to maintain high optical efficiency. The receiver telescope is the most important

optical element pertaining to collecting photons from deep, weak, seafloor returns. As previously mentioned, the transmit beam is roughly 3 meters in diameter at the water surface and continues to grow at an increasing rate while scattering during water column propagation. Thus, the telescope must have a sufficiently large FOV to collect as many returning photons as possible. A system's FOV loss function determines how many photons it can capture for specific environmental conditions [42, 43]. However, the trade-off when using a larger FOV is higher noise because more photons arising from the background environment are detected [37, 44]. A narrowband, spectral filter may be used to mitigate this effect, but non-trivial analyses comparing FOV loss to background noise should be performed when modeling system performance [33]. Finally, if detectors or amplifiers are not used to compress their inputs into manageable outputs, then the receiving optics have the additional task of managing the dynamic range of returned powers. In this scenario, one strategy is to distribute incoming photons to multiple channels (i.e. a shallow-water channel or a deep-water channel) and use a gating mechanism to prevent damage from excessive incident-power levels.

Once systems collect the backscattered photons and generate a representative electronic signal, they must be processed. Two distinct approaches have developed: waveform-resolved processing and TOF processing. Waveform-resolved processing involves sampling, digitizing, operating on, and recording the backscattered signal. It has inherent advantages over TOF processing in high volumetric-scattering applications like ALB because the signal can be observed and conditioned. It also provides information such as signal magnitude, enabling estimation of seafloor reflectance [21, 45]. However, waveform-resolved processing produces significantly more data than TOF processing as systems continuously sample the backscattered signal at high sampling rates and analog front-end bandwidths. Moreover, typical dynamic range requirements necessitate high bit depth and low noise. Producing terabytes of data per hour is not uncommon [29, 46]. On the other hand, TOF processing

involves recording one range or series of ranges directly in the detector circuitry. Consequently, it is challenging to distinguish signal from noise in volumetric scattering applications. Because only a few ranges need to be recorded per pulse, TOF processing is well-suited for array-based systems. For these systems, photons are incident upon a focal plane array (FPA), whose individual pixels report the range(s). In general, current linear-mode systems operate using waveform-resolved processing while current Geiger-mode systems operate using TOF processing. The remainder of this chapter focuses on waveform-resolved processing, because the platform for my restoration technique is a linear-mode system. However, Chapter 3 revisits TOF processing when discussing augmenting a linear-mode system with a Geiger-mode system.

Waveform-resolved systems employ wavelength-specific detectors to convert detected photons into electrical current and signal amplifiers to convert the current into voltage. Detectors and amplifiers should have high analog bandwidth, to discriminate between sea surface and floor returns in extremely shallow waters, have low noise, to enable detection of deep, weak bathymetric returns, and be capable of managing the six orders of dynamic range inherent to ALB [6]. Systems typically use photomultiplier tube (PMT) detectors, as they satisfy these requirements quite well. They may even be operated in log mode, when biased appropriately, to help compress the range of returned optical powers into a manageable current output [29, 47]. If operated traditionally (i.e. PMT ouput behaves linearly), the dynamic range may be managed by either "stacking" the receiver architecture, partitioning the dynamic range into a shallow water channel and a deep water channel, or using a logarithmic amplifier. Because logarithmic amplifiers have less bandwidth [29] [48], the first approach is more common. DC-coupled, high-voltage or transimpendance amplifiers may then be used to perform signal amplification into the digitizer's acceptable range [29]. The ideal configuration for this detector-amplifier chain is a single, integrated chip so as to

minimize noise, but most ALB systems use discrete commercial-off-the-shelf (COTS) components.

Waveform-resolved systems use dedicated digitizers for each receiver channel. For a stacked receiver architecture, each of the t0, shallow water, deep water, and infrared channels would have its own digitizer. After receiving the timing unit's synchronized trigger signal, the digitizers begin sampling analog input produced by the photodetectors and quantizing the voltage into discrete bins. They must have high bit depth and low noise while sampling at high rates. A good metric for assessing digitizer capabilities is its effective number of bits (ENOB). This value informs how many bits of resolution the digitizer has at various input frequencies. Digitizers with ENOB values close to 10 and sampling rates over 1 GS/s are ideal for ALB applications [49]. Figure 6 shows a digitized ALB waveform from a device with these characteristics. Once a signal is digitized, it may be processed by algorithms on the dedicated computer and stored on the hard drive. Recently, field-programmable gate array (FPGA) technology on the digitizers have been utilized as well [49]. FPGA-based algorithms can quickly perform signal conditioning and ranging on the recorded waveforms, enabling real-time computation and display of point cloud coordinates. One such "mixed-mode" computing architecture, using the digitizer's FPGA in tandem with the computer's central processing unit (CPU) and graphics processing unit (GPU), can achieve real-time computation and display of point cloud coordinates up to 40 kHz [46], well above current pulse frequencies for typical high-power green lasers. The next section details how coordinates may be computed in waveform-resolved processing.

2.2 Computing Seafloor Coordinates

Waveform-resolved systems decompose individual waveforms into in-air and in-water path lengths (also called ranges). The in-air path length (l_A) is determined by first

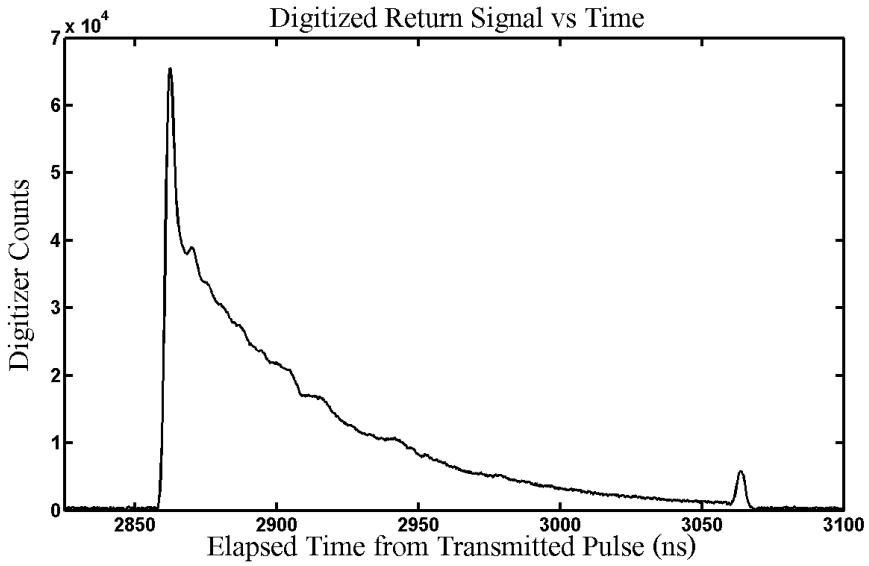

Figure 6: Linear-mode, waveform-resolved bathymetric lidars produce a waveform for each transmitted pulse by converting received, backscattered photons into digitized electrical voltages versus time.

computing the time-of-flight difference between the sea surface signal and the transmitted pulse (t_A), halving it to account for round-trip propagation, and converting the result to length using the speed of light, c, as the propagation velocity. In-water path length (l_W) is determined similarly by computing the time-of-flight difference between the seafloor signal and the sea surface signal (t_W), but using the appropriate speed of light in water. Figure 7 shows the ranges and their corresponding time-of-flight difference values as would be computed from an ALB system's return waveform.[2] In this example, signal peaks determine the surface and floor signal locations; often, a peak's leading inflection point is used in the measurement of these locations, since the inflection points are less susceptible to noise and pulse broadening [50].

By using these ranges and accounting for the lidar's pointing angles, seafloor 3D positional coordinates may be computed in the lidar's sensor body frame (SBF). ALB systems may then produce coordinates geo-referenced to the local geodetic frame (LGF) by using the aircraft GPS and IMU data and by correcting for appropriate boresight alignments to first order with Equation 1 [51, 52]

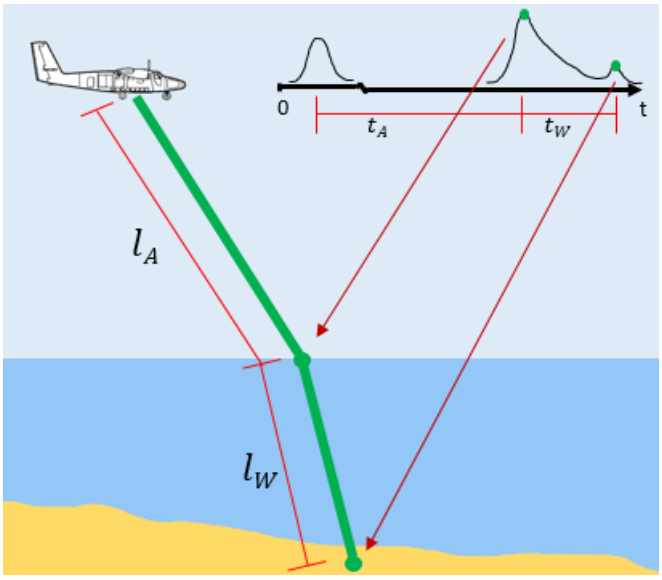

Figure 7: Bathymetric-lidar signal waveforms contain peaks corresponding to sea surface and seafloor returns.

$$\begin{bmatrix} N_P \\ E_P \\ D_P \end{bmatrix} = R_Z(\kappa)R_Y(\phi)R_X(\omega)\left(R_Z(\Delta\kappa)R_Y(\Delta\phi)R_X(\Delta\omega)\left(R_Z(\theta)\left(R_Y(\phi_A)\begin{bmatrix}0\\0\\l_A\end{bmatrix}+R_Y(\phi_w)\begin{bmatrix}0\\0\\l_w\end{bmatrix}\right)\right)+\begin{bmatrix}\Delta X\\ \Delta Y\\ \Delta Z\end{bmatrix}\right)+\begin{bmatrix}N_T\\ E_T\\ D_T\end{bmatrix}, \quad (1)$$

where:

N_P : Northing coordinate of lidar point on seafloor,
E_P : Easting coordinate of lidar point on seafloor,
D_P : Down coordinate of lidar point on seafloor,
κ : Aircraft heading,
ϕ : Aircraft roll,
ω : Aircraft pitch,
N_T : Aircraft northing coordinate,
E_T : Aircraft easting coordinate,
D_T : Aircraft down coordinate,
$\Delta\kappa$: Boresight alignment angle in κ,
$\Delta\phi$: Boresight alignment angle in ϕ,
$\Delta\omega$: Boresight alignment angle in ω,

[2]Airplane in Figure 7 was taken from www.aoc.noaa.gov.

ΔX : Inertial-to-sensor body frame x-lever arm,
ΔY : Inertial-to-sensor body frame y-lever arm,
ΔZ : Inertial-to-sensor body frame z-lever arm,
θ : Scan angle,
ϕ_A : In-air, off-nadir angle,
l_A : In-air path length,
ϕ_w : In-water, off-nadir angle
l_w : In-water path length,

and, R_X, R_Y, and R_Z, are 3x3, right-hand-rule, rotation matrices about the x-, y-, and z-axis, respectively.

Equation 1 is a series of rotations, scales, and translations accomplishing the transformation of coordinates from the SBF to the inertial body frame (IBF), and then to the LGF. Most of its parameters are measured with high certainty during a campaign, except one: the in-water, off-nadir angle, ϕ_w. This angle determines the transmitted pulse's new trajectory resulting from refraction at the air-water interface. Usually, it is assumed to be constant [53], and is calculated using Snell's Law with θ_1 as ϕ_A, n_1 as the index of refraction of air, and n_2 as the index of refraction of water (e.g. when $\phi_A = 20°$, ϕ_w is 14.9° for $n_{air} = 1.00$ and $n_{water} = 1.33$). This assumption is correct only when the air-water interface is perfectly flat. As the interface becomes wavy, the assumption breaks down, the uncertainty increases, and the accuracy of seafloor coordinates computed using Equation 1 decreases.

Coordinate accuracies achieved with Equation 1 also depend on reliably detecting the air-water interface. Since the transmitted pulse's velocity and direction change at the interface, it is paramount to compute accurate in-air ranges. Early system designers paid particular attention to overestimates of in-air ranges [37]. Because green pulses have relatively small in-water attenuation coefficients, the observed surface signals in return waveforms were generated by a superposition of the interface and water column returns, resulting in peaks corresponding to locations beneath the true air-water interface [37]. To account for this phenomenon, multi-wavelength detection

strategies were developed that augmented the green receiver channel with infrared and Raman channels [18]. Currently, with improvements in system transfer functions and with increased digitizer sampling rates, dual-wavelength (infrared and green) or single-wavelength (green) interface-detection strategies have superseded those using Raman channels. The best interface detection strategies are now accurate to within a decimeter [6], but the spatial resolution of surface coordinates is low. Low surface resolution presents a problem during post-processing of ALB data, as surface coordinates are used to generate sea surface topography (SST) models that help determine the pulse's true refracted angle into water (ϕ_w). Intuitively, lower resolution SST's should produce less accurate estimates of ϕ_W than what higher resolution SST's produce, though there is no published work quantifying this. Furthermore, to my knowledge, there is no published work describing the process of post-processing refraction correction, nor is there any published work regarding the accuracy improvements made by performing post-processing refraction correction. The research presented in this thesis fills these three voids in the field in addition to improving SST resolution and the accuracy of ϕ_w.

2.3 Estimating Seafloor Reflectance

When radiometrically calibrated, waveform-resolved systems can estimate seafloor reflectance from individual waveforms. The signal reflected from the seafloor at in-water-path-length l_w may be modeled as

$$P_r = \frac{P_t \eta \rho A T^2 F e^{-2 l_A \tau_A}}{\pi (n_w l_A + l_w)^2 (STF)} \exp(-2(a + b_b) l_w), \tag{2}$$

where:

P_t : Transmitted peak power,
η : Optical efficiency of receiving optics,
ρ : Seafloor reflectance at laser wavelength,

A : Area of receiver aperture,
T : Transmittance at air-water interface,
F : Field-of-view loss,
τ_A : In-air attenuation coefficient,
l_A : In-air path length,
n_w : Index of refraction of water,
l_w : In-water path length,
a : Absorption coefficient of water,
b_b : Backward scattering coefficient of water, and
STF : Stretch Factor.

Equation 2 is a radiative transfer equation describing the received peak power by the lidar after the pulse's round-trip propagation [21]. The equation may be equivalently written in terms of energy [37], but the only term in either formulation that contains information about the seafloor is ρ, the seafloor reflectance at the transmitted pulse's wavelength, typically near 532 nm [6]. ALB systems can estimate seafloor reflectance for each transmitted pulse by inverting this equation to solve for ρ, shown in Equation 3 as

$$\hat{\rho} = \frac{P_r \pi (n_w l_A + l_w)^2 (STF)}{P_t \eta A T^2 F e^{-2 l_A \tau_A}} \exp(2(a + b_b) l_w), \tag{3}$$

and create attributed point clouds by assigning the value to the corresponding seafloor coordinate [21]. In practice, this inversion is accomplished with several assumptions and constraints. For example, atmospheric effects, the field-of-view loss function, and the two-way transmittance at the air-water interface may be assumed to be constant throughout a campaign [21]. The four estimates that must be made, which depend on preferred algorithm, are the peak power received, the background noise power, the stretch factor, and the system attenuation factor, $a + b_b$. After constraining the inversion in this way, seafloor reflectance estimates may be assigned to each coordinate and a rasterized, seafloor-reflectance image can be generated. Since the

coordinates are irregularly spaced, generating the raster image involves interpolating the reflectance estimates onto a regular grid by binning, tinning, or kriging [54].

Since Lee and Tuell [54] demonstrated the first successful ALB seafloor-reflectance images, the community has made considerable progress in seafloor reflectance imaging. Most of the progress was made by radiometrically calibrating the lidar, removing some of Lee's and Tuell's assumptions about Equation 2 and by improving estimates of the system attenuation factor and the stretch factor [21, 53]. Another important advancement was using the lidar's waveform data to constrain the inversion of simultaneously-acquired, passive hyperspectral data, resulting in better estimates of parameters in Equation 2 [55, 56]. Clearly, the most important parameter to estimate accurately is $a + b_b$, since it appears in the exponent. The second-most important parameter is the stretch factor term, arising from environmental and system stretching of the transmitted pulse [37]. This term, if ignored, can result in overestimates of seafloor reflectance by a factor of 2-4 [53].

The origin of the stretch factor can be understood in the following way. A return waveform can be viewed as the output of a linear system whose input is an impulse response convolved with the transmitted pulse shape. Viewed in this way, ALB system waveforms are the result of convolving transmitted pulses with a transfer function, which I name the bathymetric lidar transfer function (BLTF). The BLTF, shown schematically in Figure 8, varies for each pulse, and is composed of two transfer functions cascaded in series: the environmental and system transfer functions [57]. The environmental transfer function is a cascade of transfer functions in series, composed of the atmospheric, air-water-interface, water-column, and seafloor transfer functions; similarly, the system transfer function is a cascade of transfer functions in series corresponding to the different receiver components: the detector, amplifier, and digitizer [57]. Guenther [37] was the first to present bathymetric lidar as a linear system, and named the convolution of the transmitted pulse and the environmental

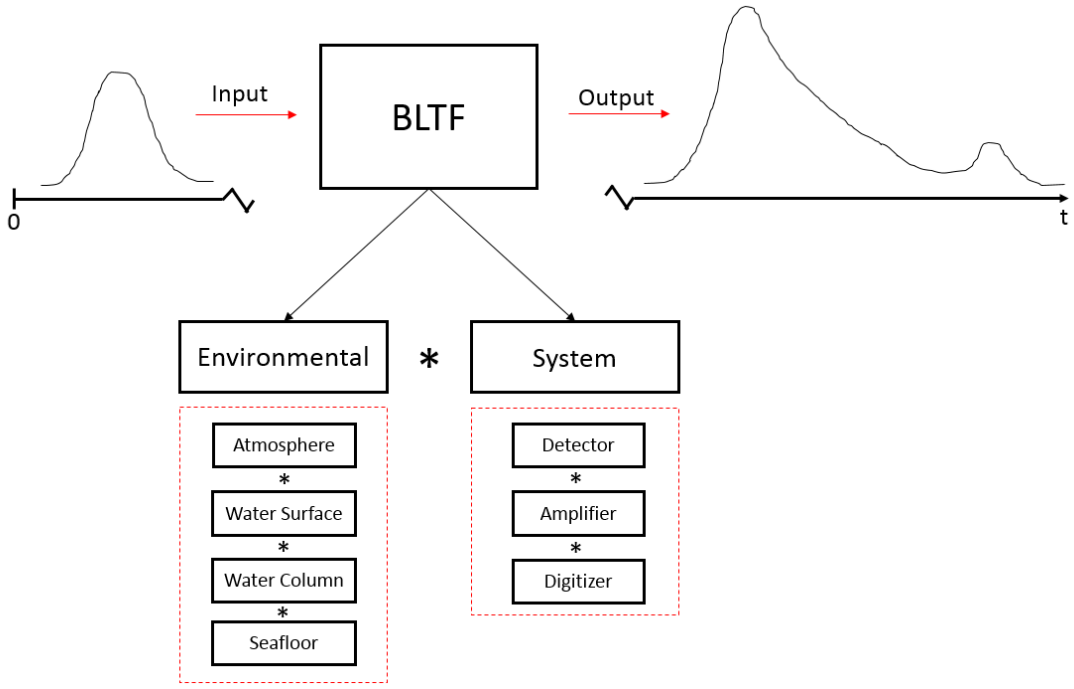

Figure 8: Convolving transmitted laser pulses with the bathymetric-lidar transfer function produces bathymetric return signals.

transfer function as the environmental response function. I call this signal the optical domain signal for simplicity. Ramnath et. al [57] extended this model to account for electronics, showing that optical domain signals are then convolved with the system transfer function to produce digital signals similar to the one in Figure 6.

When viewed in the context of linear systems theory, then, the stretch factor in Equation 2 can be thought of as a broadening of the transmitted pulse resulting from its convolution with the BLTF. The two system parameters that affect this broadening are the in-air, off-nadir angle, ϕ_A, and the system's channel response function (which I call the system transfer function in Figure 8) [37]. The in-air, off-nadir angle, causing an inclined incidence of the pulse at the air-water interface and on the seafloor, produces geometric stretching due to the pulse's 3-meter footprint. The system transfer function, which converts the incident optical signal to an electrical signal also introduces stretching due to bandwidth limitations of each component [57]. The environmental parameters that affect the stretching arise from in-water propagation,

from the seafloor, and from the air-water interface. In-water propagation causes pulse broadening because the beam spreads into an expanding cone as it travels deeper in the water due to the water's scattering properties (recall Figure 5). Thus, in-water propagation produces depth-dependent pulse broadening that is difficult to characterize [18]. The seafloor introduces pulse stretching when it is not uniform (rugose) or when its orientation is not normal to the incident pulse. These seafloor characteristics disperse incident photons differently than uniform, planar seafloors, causing a broadening of the seafloor return. Seafloor rugosity and slope and their effects on the observed signal have been explored and modeled with some success [58, 53]. The air-water interface introduces pulse stretching when it is not flat, though no published work exists regarding this stretching. Intuitively from geometric optics, irregular interfaces cause different parts of an incident beam to refract into the new medium at different angles. In this case, different parts of the laser beam refract into the water differently. While some work has been published regarding the correction of the system response and stretching due to inclined incidence [57] [53], there is no published work regarding the correction of stretching effects due to irregular air-water interfaces. This thesis introduces the first published technique correcting stretching resulting from irregular air-water interfaces. Stretching caused by in-water propagation and the seafloor is outside the scope of this thesis.

2.4 Assessing System Accuracy

Because ALB point clouds are used to make or update marine navigation charts, there is growing interest in assessing their accuracy. In fact, International Hydrographic Organization (IHO) standards for hydographic surveying actually require positioning accuracy assessment for survey data [32]. Furthermore, NGA recently released a mandate requiring 3D uncertainty assessments for every computed lidar point [34]. These assessments are usually computed *a posteriori* by comparing the lidar points to those

surveyed with shipborne acoustic systems. Drawbacks of this method are detailed in Chapter 1. A more robust approach is to propagate measurement uncertainties onto coordinates through a Total Propagated Uncertainty (TPU) framework.

Tuell [59] introduced such a framework for waveform-resolved ALB, yielding assessments and error contributions for every lidar point. It is shown in Equation 4 as,

$$\Sigma_P = J\Sigma_M J^T \tag{4}$$

where:

Σ_P : TPU matrix (3x3) filled with positional variances and covariances,
J : Jacobian matrix (3x17) formed with partial derivatives, and
Σ_M : Cofactor matrix (17x17) formed with measurement variances and covariances.[3]

The Jacobian and cofactor matrices, J and Σ_M, may be constructed as

$$J = \begin{bmatrix} \frac{\partial N}{\partial \kappa} & \frac{\partial N}{\partial \phi} & \dots & \dots & \frac{\partial N}{\partial \phi_w} \\ \frac{\partial E}{\partial \kappa} & \frac{\partial E}{\partial \phi} & \dots & \dots & \frac{\partial E}{\partial \phi_w} \\ \frac{\partial D}{\partial \kappa} & \frac{\partial D}{\partial \phi} & \dots & \dots & \frac{\partial D}{\partial \phi_w} \end{bmatrix} \tag{5}$$

$$\Sigma_M = \begin{bmatrix} \sigma_\kappa^2 & \sigma_\kappa\sigma_\phi & \dots & \dots & \sigma_\kappa\sigma_{\phi_w} \\ \sigma_\phi\sigma_\kappa & \sigma_\phi^2 & \dots & \dots & \sigma_\phi\sigma_{\phi_w} \\ . & & . & & . \\ . & & & . & . \\ . & & & . & . \\ \sigma_{\phi_w}\sigma_\kappa & \sigma_{\phi_w}\sigma_\phi & \dots & \dots & \sigma_{\phi_w}^2 \end{bmatrix}. \tag{6}$$

The order of variables used in these matrices is arbitrary, so long as it is consistent, but I used the following order: κ, ϕ, ω, $\Delta\kappa$, $\Delta\phi$, $\Delta\omega$, ΔX, ΔY, ΔZ, N_T, E_T, D_T, θ, ϕ_A,

[3] In this thesis, the notation $\sigma_X\sigma_Y$ is defined to mean $cov(X, Y)$.

l_A, l_w, ϕ_w. The reason for this order becomes apparent in Chapter 3. Computation with Equation 4 results in a TPU matrix containing the variances and covariances of a point's northing, easting, and down coordinates, shown in Equation 7 as,

$$\Sigma_P = \begin{bmatrix} \sigma_N^2 & \sigma_N\sigma_E & \sigma_N\sigma_D \\ . & \sigma_E^2 & \sigma_E\sigma_D \\ (sym) & . & \sigma_D^2 \end{bmatrix}. \tag{7}$$

.

This procedure requires *a priori* knowledge of the variances and co-variances of the measured data used in Equation 1 [33]. Although most of the variances can be estimated from calibrations or are computed by the navigation system's Kalman filter, many of the co-variances are unknown. For this reason, development of the full matrix of Equation 6 is an important and active area of research because the robust implementation of this error propagation fulfills IHO's requirement of propagating measurement uncertainties onto coordinates and fits nicely with NGA's mandate requiring 3D uncertainty assessments for every lidar point [34]. Assessments using this model can be performed much quicker than acoustic validation campaigns, reducing response time and cutting costs. In fact, the previously-mentioned "mixed-mode" computing architecture that computes and visualizes coordinates at 40 kHz can also compute Σ_P for each lidar point as well [46]. This revolutionary capability can provide ALB system operators instantaneous feedback regarding survey accuracy, instead of waiting hours or days. By reducing Σ_P to a single parameter, points in the cloud may then be colored by their uncertainty. One possible color configuration would be to color points that do not meet accuracy standards red and to color those that do green. Operators may then easily locate areas with poor accuracy and re-survey them if necessary. A possible accuracy metric could be SAS_{99}, a single scalar value defined as the radius of a sphere centered at the true position, containing the position

estimate in 3D, with the probability 99 percent [60]. It is computed as

$$SAS_{99} = 1.122(\sigma_N + \sigma_E + \sigma_D) \tag{8}$$

where σ_N, σ_E, and σ_D are the standard deviations of the coordinates computed as the square roots of the main diagonal of Σ_P.

Another nice feature of this model is that it can identify and quantify each individual contribution to seafloor coordinate uncertainty. Consequently, system designers may use this framework to identify error-prone aspects of the system and adjust them accordingly by reducing their contributions. However, Tuell's model does not include air-water-interface measurement variances, as it assumes a flat air-water interface. This assumption is not surprising; while some work has been published regarding modeling the sea surface as a function of wind speed and depth [61, 62, 63] or as a function of surface facets [64, 65] and its subsequent effects on transmission and steering into water, no published work details the uncertainty introduced by an irregular air-water interface on a lidar's refracted pointing vector. In Chapter 3, this thesis derives a way to characterize an airborne lidar's air-water-interface measurement uncertainty and characterizes its effect on seafloor-coordinate positional uncertainty by developing a new TPU framework.

CHAPTER III

SEAFLOOR IMAGING USING A NOVEL LIDAR SYSTEM

This chapter derives new math models to compute seafloor coordinates, to estimate seafloor reflectance, and to assess ALB systems' accuracy. These math models robustly account for sea surface effects and may be viewed as replacements for the math models presented in Chapter 2. The chapter begins by specifically explaining how wavy water surfaces affect ALB systems' transmitted laser pulses. The chapter then details a novel, hybrid-lidar processing architecture, wherein high-resolution interface models constructed from Geiger-mode system measurements are registered with co-temporal waveforms. The chapter then explains how data produced by this new architecture may be used in the new coordinate-computation and reflectance-estimation techniques to compensate for sea surface effects, enhancing ALB-systems' seafloor imaging capabilities. Finally, the chapter concludes by detailing the new accuracy assessment technique.

Transmitted lidar pulses interact with the air-water interface whose orientation changes because of ocean waves. Sea surface topography (SST), i.e. the height, slope, and complexity of the wave structure, depends on many different factors, which is outside the scope of this work. However, in a general sense, ocean waves can be classified into three different subsets relative to a transmitted pulse's footprint on the air-water interface: low-frequency waves, high-frequency waves, and waves resulting from the superposition of low- and high-frequency waves. Low-frequency waves act as tilted interfaces, steering the entire beam in a different direction than a flat air-water interface would. High-frequency waves act as dispersive interfaces, steering different

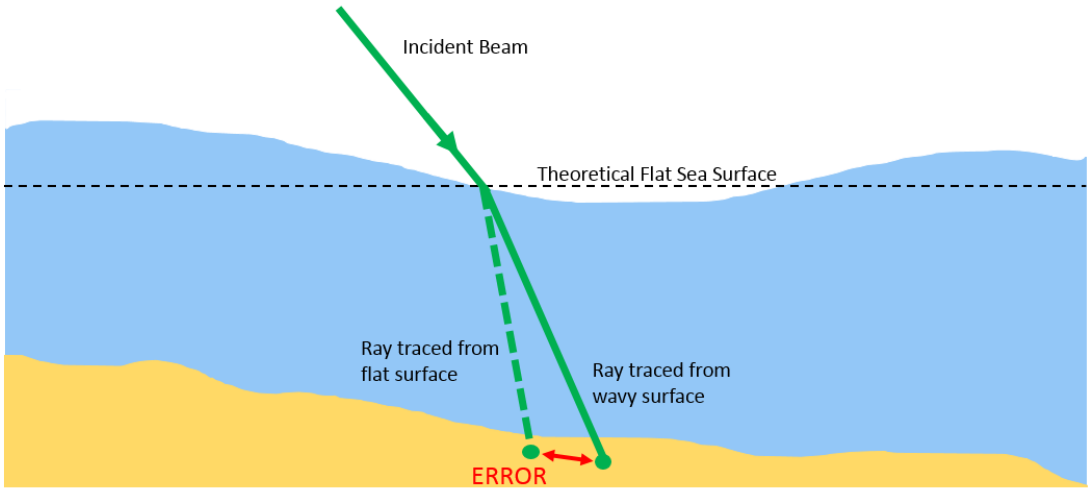

Figure 9: Uncompensated variation in air-water interface orientation causes seafloor coordinate error.

parts of the beam in different directions. This can also result in an overall change of the beam trajectory. Superposed waves steer and disperse transmitted pulses.

Consider the scenario depicted in Figure 9 in which the air-water interface is tilted. This represents the case of a pulse interacting with a low-frequency wave. The lidar's transmitted beam is steered to a different position on the seafloor because of the non-flat tilted orientation. In general, low-frequency tilts can have arbitrary orientation, as opposed to the in-plane tilt in Figure 9. This means that the beam's refracted trajectory can be steered arbitrarily, consistent with Snell's Law, after interacting with the interface. In the context of this example, arbitrary surface tilt may produce coordinates that do not lie in the plane of this page. Instead, they may lie in or out of the page depending on the tilt's 3D orientation. The current coordinate-computation technique, Equation 1, only allows the transmitted pulse to vary in one direction, which is along the path of the incident vector. This limitation arises because of the flat-water assumption and does not accommodate a scenario in which the interface steers the beam in some other direction.

High-frequency waves contain SST features smaller than the laser's footprint.

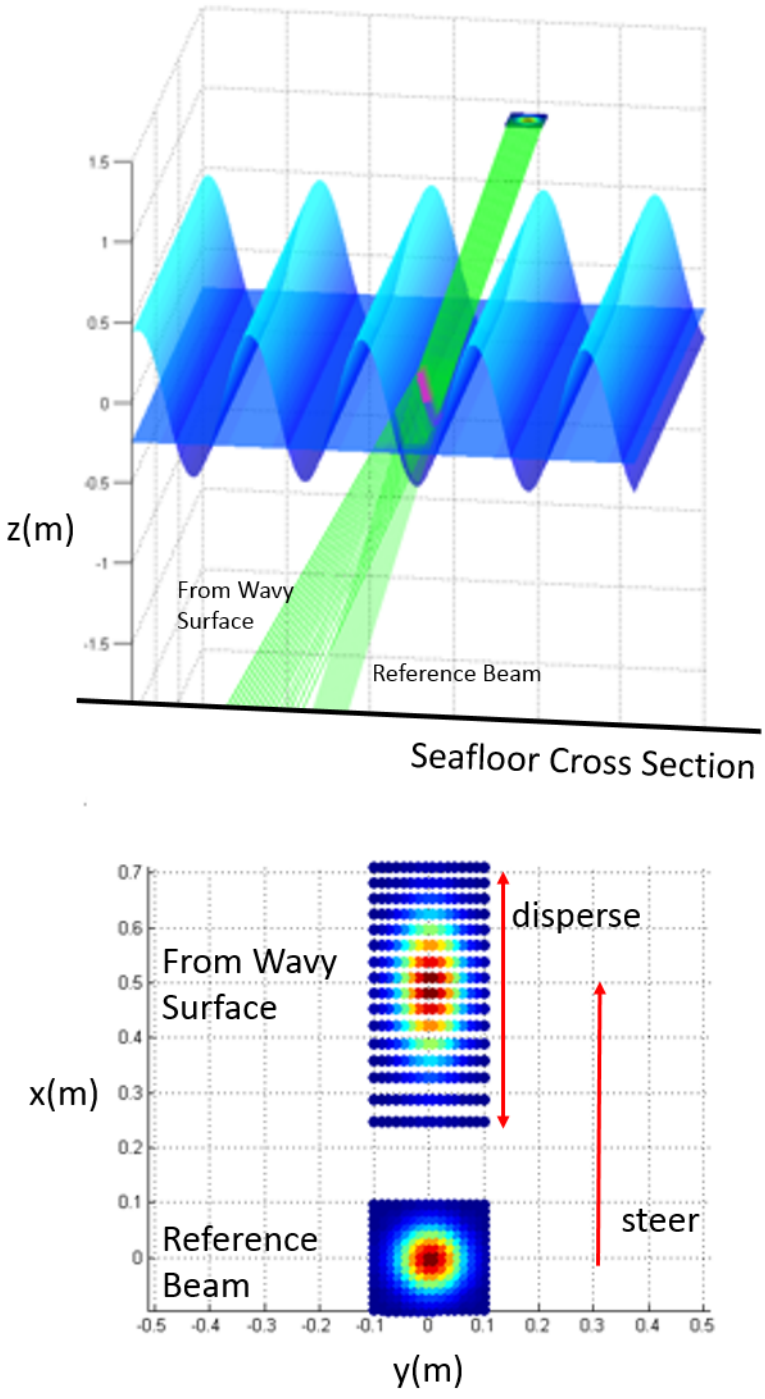

Figure 10: High-frequency SST steers and disperses incident laser beams.

When beams interact with these types of interfaces instead of flat interfaces, they are steered to different positions on the seafloor and dispersed into wider beams. Figure 10 contains a theoretical scenario illustrating these effects. Here, a laser beam divided into 256 rays interacts with a high-frequency sinusoidal surface with SST oriented parallel to the pointing vector. For comparison, an identical laser beam, called the reference beam, interacts with an assumed flat surface. In this example, the beam interacting with the high-frequency wavy surface is steered to a seafloor position centered 50 *cm* away from the reference beam and is also enlarged by 25 *cm*. Not accounting for these effects causes inaccurate seafloor-coordinate computation. As with low-frequency tilts, high-frequency structures at the interface can be oriented arbitrarily, producing a refracted beam whose direction can not be predicted by Equation 1. Clearly, the underlying flat-water assumption must be removed for systems to compute accurate seafloor coordinates.

To account for wavy surfaces properly, Equation 1 must be generalized to allow for arbitrary refracted trajectories into the water. One approach to achieving this is introducing a forward-starboard-down reference frame at the intersection of the reference ray and air-water interface, oriented with X-axis parallel to the pointing vector. Then, the transformation of coordinates model of Equation 1 can be extended to account for irregular interfaces by introducing an X-rotation through an angle about the pointing vector, which I define as ω_w, as shown in Equation 9.

$$\begin{bmatrix} N_P \\ E_P \\ D_P \end{bmatrix} = R_Z(\kappa)R_Y(\phi)R_X(\omega)\left(R_Z(\Delta\kappa)R_Y(\Delta\phi)R_X(\Delta\omega)R_Z(\theta)\left(R_Y(\phi_A)\begin{bmatrix} 0 \\ 0 \\ l_A \end{bmatrix} + R_Y(\phi_w)R_X(\omega_w)\begin{bmatrix} 0 \\ 0 \\ l_W \end{bmatrix}\right) + \begin{bmatrix} \Delta X \\ \Delta Y \\ \Delta Z \end{bmatrix}\right) + \begin{bmatrix} N_T \\ E_T \\ D_T \end{bmatrix}, \quad (9)$$

where:

ϕ_w : in-water steering angle parallel to the pointing vector
ω_w : in-water steering angle orthogonal to the pointing vector.

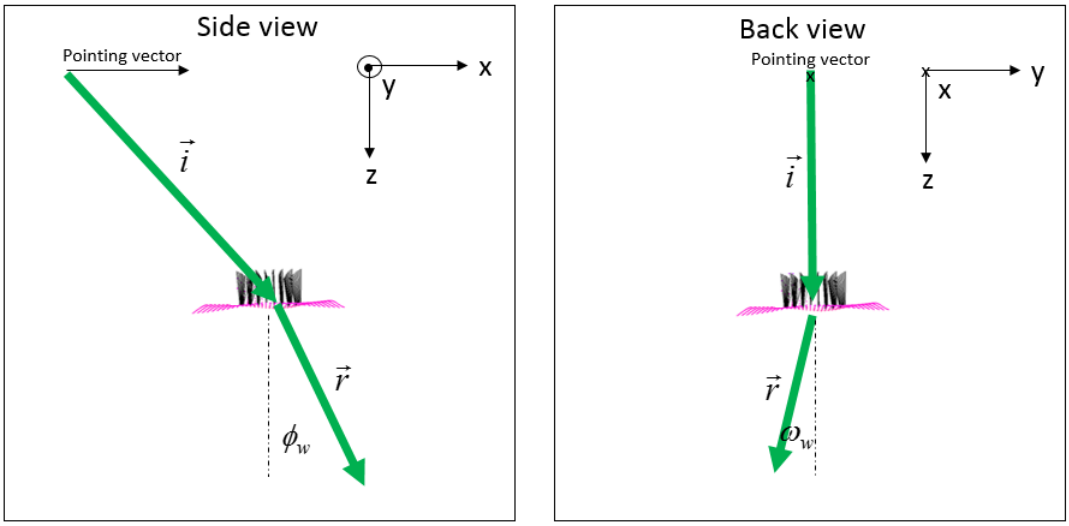

Figure 11: Arbitrary surface orientation produces a refracted beam with components parallel and perpendicular to the lidar's pointing vector.

The last two rotations in Equation 9 are shown about in-water steering angles that allow for an arbitrary refracted trajectory. For the simple case of a flat air-water interface, ω_w is 0, and ϕ_w can be computed using Snell's Law, which results in Equation 9 simplifying to Equation 1. For the case of a non-flat, air-water interface, these angles are not directly observable and ϕ_w can no longer be computed with Snell's Law. Instead, they must be expressed in terms of the known scanner angle and in-air, off-nadir angle pertinent to a particular lidar and the air-water interface's orientation. Figure 11 shows perspective views of the pointing vector, the incident vector, the refracted vector, ϕ_w, and ω_w in the presence of an arbitrarily tilted surface. Clearly, ϕ_w accounts for the refracted vector's component parallel to the pointing vector and ω_w accounts for the refracted vector's component perpendicular to the pointing vector.

The next section details an ALB system that measures SST co-temporally with sufficient resolution to improve its seafloor imaging capabilities. Specifically, co-temporal high-resolution interface measurements from an infrared, TOF, Geiger-mode

lidar are used with a green, linear-mode, waveform-resolved system. This novel, hybrid lidar can construct digital surface models (DSMs) from its interface measurements, ray trace through the DSMs, and estimate ϕ_w and ω_w. These angles may then be used in Equation 9 to compute accurate seafloor coordinates even in the presence of waves. This lidar also uses the DSMs to estimate interface-induced stretching for each pulse, a new advancement in the field of ALB, which may then be used to improve seafloor reflectance estimates.

3.1 A Novel, Hybrid lidar

Current ALB systems do not robustly account for sea surface effects when computing seafloor coordinates and estimating seafloor reflectance. The primary reason is because they lack high-resolution, co-temporal measurements of the air-water interface. Single-wavelength systems have no more than a few measurements with which to reconstruct the air-water interface *a posteriori* to improve the refracted beam's in-water trajectory; dual-wavelength systems add a few more measurements with their higher interface sampling rates using an IR laser, but the resolution is still poor. In either case, the amount of coordinate improvement by performing *a posteriori* correction is unknown. Furthermore, neither single- nor dual-wavelength systems have sufficient surface resolution to correct for interface-induced pulse stretching from irregular interfaces.

One way to increase a system's surface resolution is to use an IR, array-based, TOF lidar. Figure 12 depicts this scenario. Each pixel in the TOF array returns ranges within its unique FOV, creating many co-temporal measurements across a wide spatial extent. These measurements would originate from IR backscatter at or near the water surface because IR wavelengths have very high attenuation in water [61]. The resulting TOF values, then, describe each pixel's distance to the air-water interface and may be used to produce coordinates that lie on the water surface. Surface

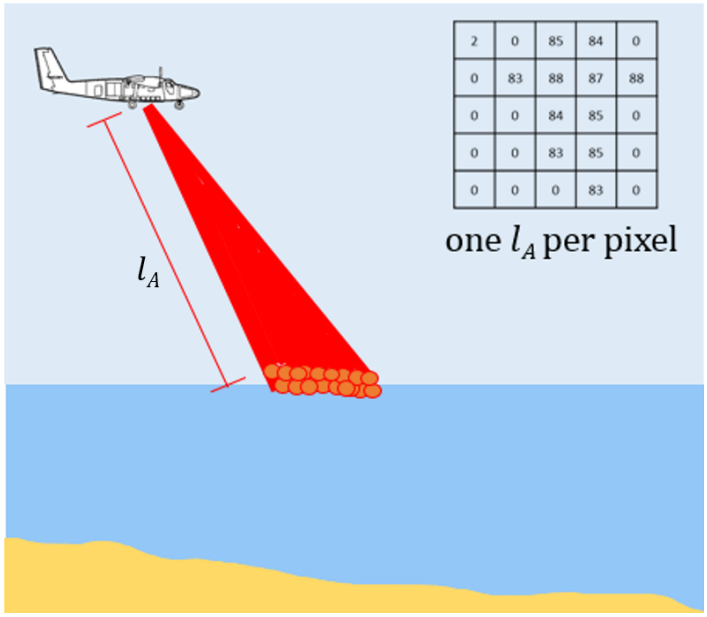

Figure 12: Array-based TOF lidars operating in the IR may be used to produce co-temporal surface measurements over a wide spatial extent.

coordinate resolution then becomes a design decision, depending on transmitted beam divergence, receiver FOV, and sensor resolution. While TOF lidar noise is normally a concern for volumetric scattering applications like ALB, the surface-concentrated infrared backscatter acts more like a "hard target" problem, to which TOF lidars are more suited.

Waveform-resolved ALB systems using the method just described could potentially improve their seafloor imaging capabilities. If densely spaced, the co-temporal surface coordinates may be used to reconstruct the air-water interface with high resolution for each pulse, allowing a system to compute the beam's refracted in-water trajectory more accurately and to estimate the seafloor's reflectance better. To this end, Georgia Tech Research Institute's (GTRI) Electro-Optical Systems Laboratory (EOSL) designed and built a novel lidar that augments a waveform-resolved, linear-mode system with a TOF, Geiger-mode lidar. This is believed to be the world's first hybrid lidar. This system, shown in Figure 13, is referred to as the Pathfinder lidar and was built fully with internal research and development funds. Its design and build

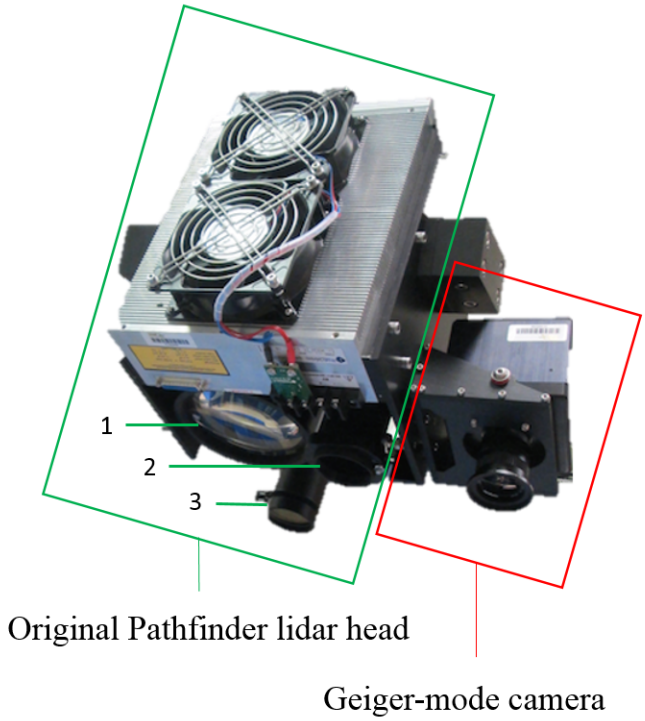

Figure 13: The Pathfinder lidar, augmented with a Geiger-mode lidar, uses high-resolution SST measurements to improve the accuracy of the seafloor coordinates it computes.

involved over 25 EOSL employees, requiring electrical, mechanical, optical, and computer engineering expertise. My contribution to Pathfinder was developing its unique, hybrid processing architecture, wherein novel algorithms operate on Geiger-mode and linear-mode data simultaneously.

Pathfinder combines a green, waveform-resolved, linear-mode lidar with a 32x32-element, IR, Geiger-Mode, Avalanche Photodiode (GmAPD) 3D camera. It uses a 2-kHz Nd:YAG laser that produces co-located beams of 1064-nm and 532-nm wavelength. The beams are purposefully separated by Pathfinder's transmitting optics so as to control each beam's divergence independently. In Figure 13, the green and IR transmitters are identified by labels "1" and "3", respectively. Pathfinder is a bi-axial system; the green receiver, identified by label "2", does not use the same optical path as the transmitter. Bi-axial configurations are uncommon in ALB because of alignment and calibration difficulties [66]. However, they are cheaper to implement than

co-axial configurations, the preferred method in ALB, which is why Pathfinder is bi-axial. The green receiver is non-segmented, focusing all of its captured photons onto a 532-nm-sensitive, Hamamatsu, R9880 PMT, whose current output is amplified by a DC-coupled, transimpedance amplifier (TIA). The amplifier's output voltage serves as the input to an Agilent M9703A digitizer, which is part of the "mixed-mode" computing architecture detailed in [46]. Pathfinder is also bi-axial in another sense, as the IR receiver, the GmAPD camera, is separated from the IR transmit path. Again, cost considerations drove this design. The GmAPD camera is an engineering-grade device manufactured by Princeton Lightwave [67]. It is a 1064-nm-sensitive, array-based, TOF imaging system. The camera's internal circuitry detects single-photon events with 250-*ps* timing resolution across its FPA, producing TOF values that are read directly into Pathfinder's computing architecture via camera link.

When synchronized with a laser, GmAPD cameras produce an array of TOF measurements within their field-of-view for each transmitted pulse [25]. By co-locating the green and IR beams on the water surface and by setting the IR receiver's FOV appropriately, GmAPD cameras may perform thousands of air-water interface measurements in the green beam's vicinity. The maximum number depends on the camera's resolution, which is 32x32 for Pathfinder's GmAPD camera. Importantly, each camera pixel reports only one TOF value, corresponding to the time it detects its first photon. Pixels cannot record another photon event until the camera is reset and armed for the next transmitted pulse. Because IR backscatter is concentrated at or near the air-water-interface, most TOF values reported by the GmAPD correspond to detected photons originating from there. Figure 14 depicts a scenario in which an IR, GmAPD camera operates concurrently with a green, waveform-resolved lidar. Both systems are synchronized with an Nd:YAG laser, whose IR beam is diverged larger than the green's. Here, the Geiger-mode lidar's goal is to compute surface coordinates from the TOF values its camera reports. Because the IR beam is larger than

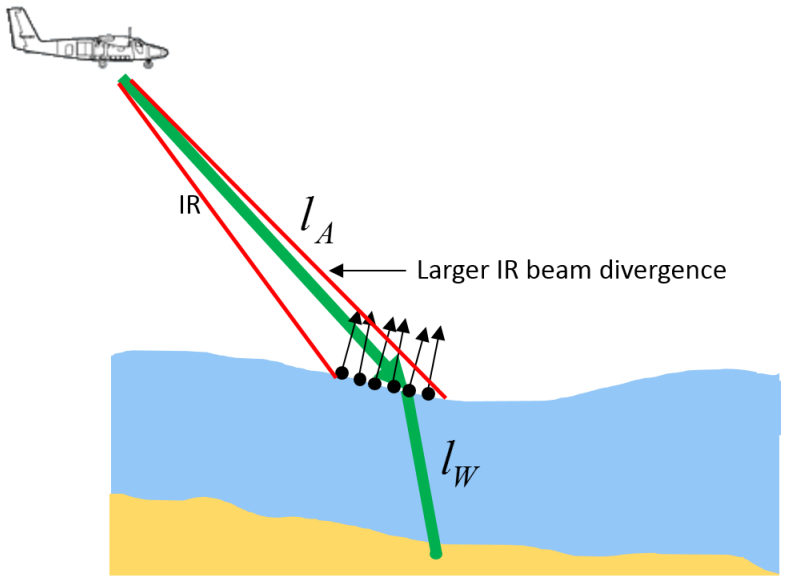

Figure 14: A hybrid system's IR channel may be used to measure low- and high-frequency SST in the green beam's vicinity.

the green beam, the camera can detect both low- and high-frequency SST. The water surface and its orientation may then be reconstructed and used in the waveform-resolved-lidar's processing algorithms to compute accurate seafloor coordinates even in the presence of waves. Figure 15 graphically explains this procedure. Pathfinder is designed to operate like this.

An important design decision for a hybrid system using the procedure outlined in Figure 15 is the spatial resolution of surface coordinates. Pathfinder's GmAPD camera resolution is fixed at 32x32 elements, so the two remaining system parameters that affect the surface resolution are the transmitted beam's divergence and the GmAPD camera's FOV. For a typical deployment scenario, the green beam is approximately 3-meters in diameter at the water surface. This means that the IR beam and the camera FOV should be larger than 3 meters at the water surface to enable detection of both low- and high-frequency SST. Figure 16 shows one possible configuration of the camera FOV and the green and IR beams on the water surface. Here, the camera's FOV on the surface is a square with 4-meter sides. Its area encompasses the green beam, sampling both inside and outside the green footprint. Importantly, it is

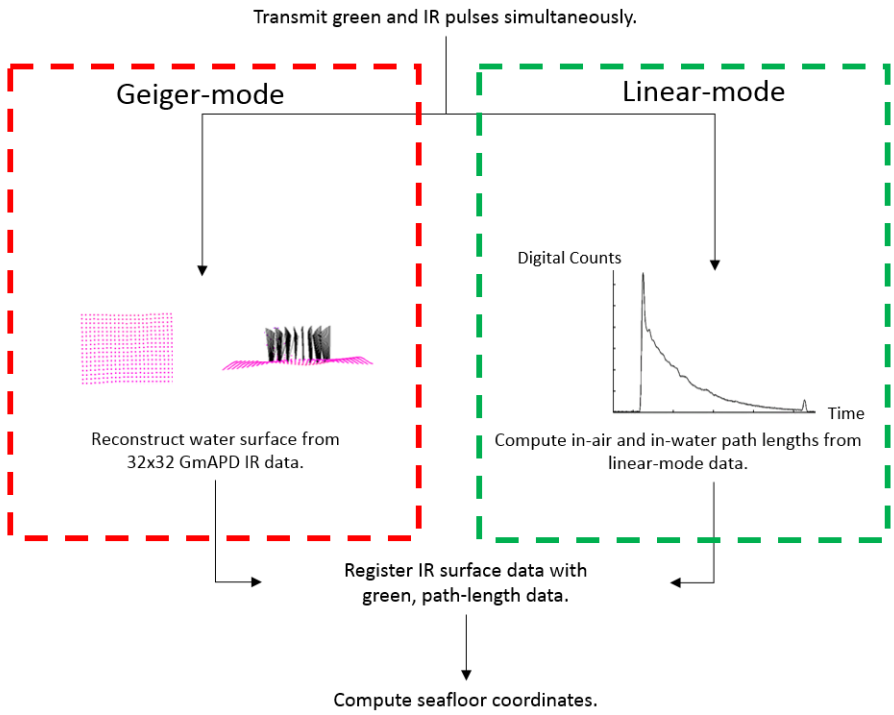

Figure 15: A hybrid lidar system may register high-resolution SST measurements with green path-length measurements to compute accurate seafloor coordinates.

also smaller than the IR beam's footprint, sampling only within the IR-illuminated area. Since there are 1024 pixels in the TOF array, the resulting surface resolution is 64 points-per-meter-squared. Given that a green footprint with 3-meter diameter has an area of approximately 7 meters-squared, this configuration can produce up to 448 sub-footprint SST measurements from a single transmitted pulse! This degree of surface resolution is a marked improvement from the one, or handful, of sub-footprint SST measurements conventional waveform-resolved systems can produce. The next section discusses how these measurements may be leveraged to model the air-water interface.

3.2 Air-water interface modeling

SST measurements produced by hybrid systems are critical to computing a green pulse's refracted trajectory into water. SST coordinates and normal vectors computed from them may be used to construct DSMs of the air-water interface. Interface

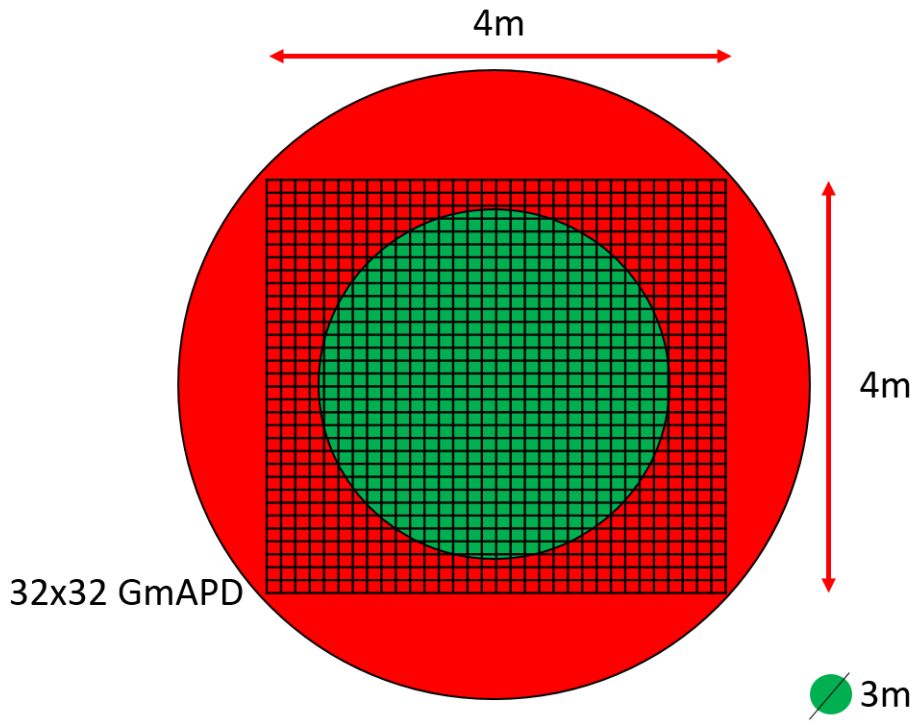

Figure 16: A hybrid lidar system may register high-resolution SST measurements with green path-length measurements to compute accurate seafloor coordinates.

coordinates may be computed using photogrammetric principles to project GmAPD focal-plane coordinates in the image space to SBF coordinates in the object space. This may be done by using Equation 10,

$$\begin{bmatrix} X \\ Y \\ Z \end{bmatrix}_{SBF} = R_Z(\theta)R_Y(\phi_A)\vec{p}_{i,j}l_{A_{i,j}}, \tag{10}$$

where subscripts i and j designate a pixel's row and column in the FPA; $\vec{p}_{i,j}$ is a unit vector describing the $<i,j>$-th pixel's "positive" projection from the image space to the object space; and, $l_{A_{i,j}}$ is the $<i,j>$-th pixel's detected TOF value converted to in-air path length. $\vec{p}_{i,j}$ may be computed using

$$\vec{p}_{i,j} = \begin{bmatrix} x \\ y \\ f \end{bmatrix} / \left\| \begin{bmatrix} x \\ y \\ f \end{bmatrix} \right\|, \tag{11}$$

where

x : $<i,j>$-th pixel's vertical offset from FPA's principal point,
y : $<i,j>$-th pixel's horizontal offset from FPA's principal point, and
f : GmAPD camera's focal length.

Here, image space offsets, x and y, are positive upward and rightward, respectively, from the principal point of the array. Since f is positive in Equation 11, the algebraic signs of image-space and object-space coordinates are the same. Thus, each pixel of the array has a $\vec{p}_{i,j}$ that projects it to object space coordinates in the same relative quadrant. For example, pixel <1,1>, the upper left pixel of the array, projects up and to the left of $[0,0,1]^T$. This convention applies to cameras whose circuitry outputs non-inverted, non-reversed digital images. Coordinates computed using this method lie in the same coordinate space as the green, waveform-resolved coordinates. [1] Hence, DSMs constructed from them may be used when modeling the green beam's refraction at the air-water interface.

In [66], Guida shows that the air-water interface may be reconstructed as a DSM using GmAPD coordinates. In that work, multiple pulses of the laser were used to generate the SST, containing surface location and orientation for each pixel in the GmAPD array, and the lidar was stationary, which is not true for ALB applications. This thesis presents an alternative method to generate DSMs of the air-water-interface with a hybrid lidar that removes the stationary assumption. To accomplish this, several aspects of the method described in [66] were removed: (1) TOF averaging when

[1] This is true for co-axial ALB systems. For bi-axial arrangements, GmAPD coordinates, as well as green coordinates, should be transformed to geodetic ones using Equation 24 to lie in the same coordinate space.

computing surface coordinates; (2) TOF filtering; and, (3) the convolution-based surface-normal computation. These methods reduce the noise inherent to Geiger-mode data but are inapplicable to mobile systems because they rely on the GmAPD camera imaging the same scene for every pulse. For mobile systems, the location of the GmAPD-imaged scene changes every pulse, necessitating pulse-specific, coordinate-computation and noise-reduction techniques. Coordinates computed from individual TOF values though have much higher noise than coordinates computed from averaged TOF values. Consequently, reducing noise and constructing accurate DSMs is even more challenging in this scenario. Recognizing the need for a noise reduction strategy and for handling 3D spatial displacement of the lidar between pulses, I developed the following DSM-construction method: (1) use coincidence processing to reduce TOF noise; (2) compute surface coordinates for each pulse and aggregate them into an accumulator array; and, (3) compute surface normal vector from the accumulator array coordinates.

The first step in my method is to use co-incidence processing to reduce TOF noise. Coincidence-processing techniques are a suite of algorithms specific to Geiger-mode systems that reduce their measurement noise [68, 69]. One effective technique is called histogram trimming, wherein only time bin values falling within a specified range gate are accepted. The upper and lower bounds of the range gate can be set *a priori*, when information about the scene is known, and can be actively updated as pointing and navigation parameters change. The width of this range gate directly affects the noise of the computed in-air ranges. For Pathfinder, the average standard deviation (i.e. noise) of a pixel's computed TOF is 1.43 ns when imaging the water surface. This statistic was determined from 20,000 flat-surface measurements using a range gate of 70 time bins equally spaced by 250 ps (this range gate was chosen *a posteriori* by viewing the actual histogram data and accepting all of the time bin values associated with the normal distribution about the water surface). Assuming the center of the

range gate was situated at the water surface, 70 time bins corresponds to a spatial range-gate width of 2.3 m (1.31 m above the surface and 0.99 m beneath the surface). This large width contributes to the very noisy nature of the GmAPD measurements. Ideally, range gates should be decreased to very small regions, on the order of a few centimeters, above and below the water surface to decrease Geiger-mode noise.

Since Pathfinder's green and IR channels are synchronized, it is possible to reduce GmAPD TOF noise by using green channel measurements as a heuristic in accomplishing the histogram trimming. Specifically, the green measurements recorded simultaneously with the IR data may be used to set the appropriate range gate when histogram-trimming the Geiger-mode data. Since Pathfinder's green surface measurement has a standard deviation of 220 ps, choosing Geiger-mode data within a range gate of +/- 2*220 ps about the green water surface measurement would result in accepting only photons directly arising from the water surface. This 880-ps gate width, representing a 2σ confidence interval about the green channel's surface measurement, corresponds to a gate width of 3.52 time bins (recall that the GmAPD has 250-ps time-bin resolution). Since the GmAPD only reports time bin values as integers, a range gate width of 4 time bins is used to accept all appropriate time bin measurements. Using this hybrid, histogram-trimming technique, the average standard deviation of a pixel's TOF value decreased to 280 ps. This measurement uncertainty is now on the same order as the linear-mode system, and shows the considerable benefits of using this novel, hybrid technique. It is important to note, however, that this method cannot be performed *en masse* for all pixels due to focal-plane-dependent differences in the traveled distance of photons. Instead, it must be performed on a per-pixel basis, as explained next.

Consider a typical airborne deployment scenario with the following specifications: altitude = 400 m; IR receiver FOV = 40 $mrad$; and, system off-nadir angle = 20 degrees. Furthermore, assume the transmitted beam is co-aligned with the center

of the IR and green receiver FOVs. If the water surface is perfectly flat, the green surface measurement, centered in the IR FOV, would report, on average, an l_A value of 425.67 m. Say, for this example, this distance is calibrated to correspond to a Geiger-mode time bin value of 2000 time bins. If this green measurement were used to gate a GmAPD frame *en masse* using the discussed hybrid approach, then only time bins from 1998-2002 would be accepted (corresponding to l_A values of 425.595 m - 425.745 m). While this range gate would work in the center of the array, it would not work toward the edges of the Geiger-mode array because photons striking these pixels travel different distances. Specifically, photons striking pixels closer to nadir will travel shorter distances and photons striking pixels farther from nadir will travel longer distances. In this example, the closest pixel toward nadir in line with the center of the array would report, on average, an l_A value of 422.67 m; the furthest pixel away from nadir in line with the center of the array would report, on average, an l_A value of 428.88 m. It is immediately evident that photons arising from the water surface that strike these pixels will not be accepted by the established range gate since they are outside the range of 425.595 m - 425.745 m. Therefore, each pixel must have its own unique range gate to accept the appropriate photons.

When the imaged scene is fixed, pixel-dependent range gates may be established *a priori* based on geometry. For example, in the case of a flat water surface and a stationary lidar, the distance from each pixel to the water surface is known, allowing appropriate range gates to be set for each pixel. However, when the imaged scene is changing, the lidar's location is changing, or if both are changing, the range gates must be updated appropriately to accept the correct photons arising from the water surface. One way to do this is to estimate the low frequency content of the water surface from a series of green surface measurements. For example, a planar surface normal may be estimated from 3 or more non-linear surface measurements. Using this information in tandem with the lidar's pointing and navigation parameters, distances

to the water surface across the FPA may be estimated and range gates may be set appropriately. In this way, appropriate low frequency content may be parsed out of the noisy Geiger-mode data. Importantly, because the range gate accepts photons in the vicinity of the low-frequency content, the high-frequency content superimposed on the low frequency content is also accepted. Thus, this technique significantly reduces the noise of Pathfinder's IR channel by restricting the range gate width on a per-pixel basis.

After reducing TOF noise, the next step in constructing interface DSMs is to compute coordinates using Equation 10 for every pulse. The resulting coordinates may then be aggregated into an accumulator array. Accumulator arrays are rasterized coordinate arrays that leverage spatial averaging to reduce noise. Their resolution is user-definable, but is typically smaller than the camera's FPA resolution. Using an accumulator array is advantageous because it allows coordinates computed from multiple, adjacent pulses to reduce system noise further. Accumulator array values are computed by averaging coordinates that fall within accumulator-array pixel boundaries. Figure 17 illustrates this process for a 2x2 accumulator array. Here, a collection of SBF coordinates have been computed using Equation 10. An accumulator array is established by setting a 2x2 grid in the SBF, designating the boundaries of each accumulator array pixel. Each pixel's value may then be computed by averaging the coordinates that fall within its boundaries. In this example, pixel-$[1, 1]$ is the average of 6 coordinates; pixel-$[1, 2]$ is the average of 3 coordinates; pixel-$[2, 1]$ is the average of 3 coordinates; and, pixel-$[2, 2]$ is the average of 5 coordinates. The accumulator-array pixel values are SBF coordinates that are less noisy than those computed using Equation 10, but they come at the expense of reduced surface resolution. Clearly, there is a trade space between accumulator array resolution and noise. This is evaluated in Chapter 4 when analyzing the accuracy of seafloor coordinates ray traced through the DSMs.

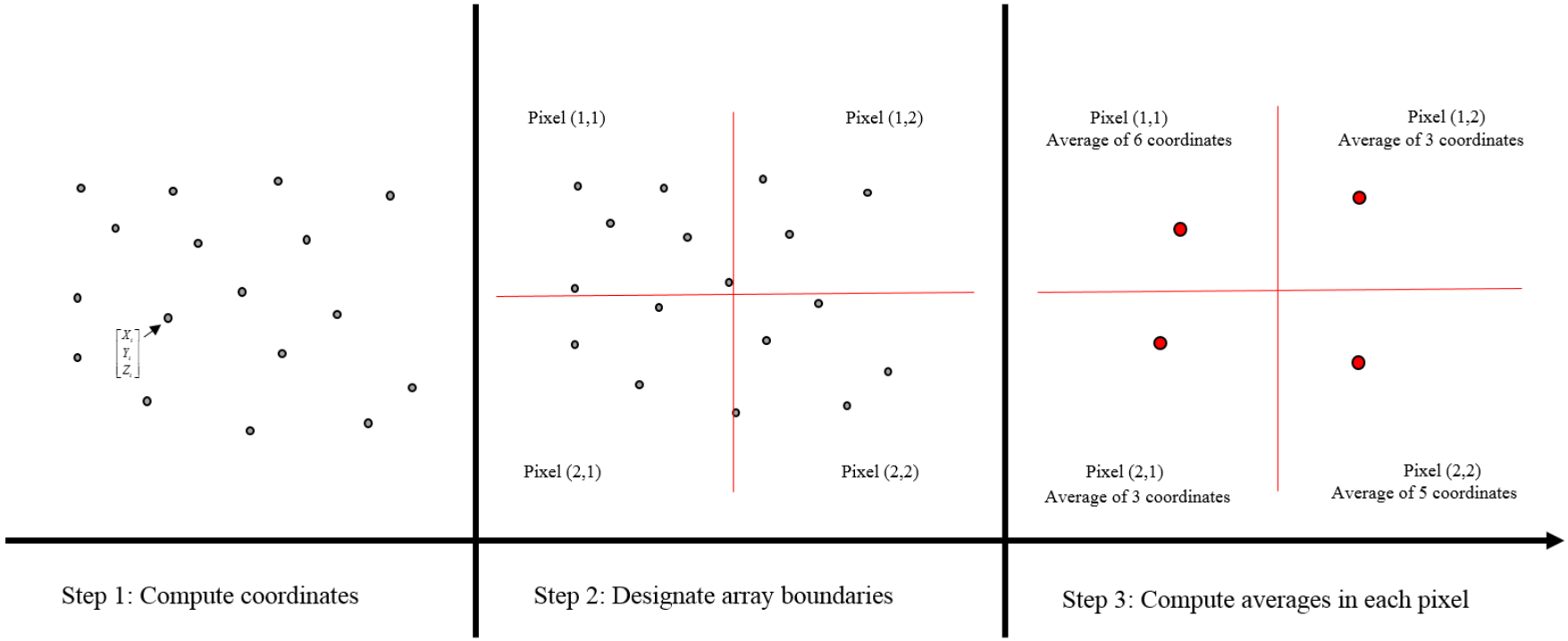

Figure 17: An accumulator array leverages spatial averaging of coordinates to reduce Geiger-mode measurement noise.

Once the accumulator array coordinates are produced, the final step in creating interface DSMs is to compute surface normal vectors from the coordinates. Two common approaches are Ordinary Least Squares (OLS) [70] and Principal Component Analysis (PCA) [71]. Both methods support computing one or multiple surface normals from the interface coordinates. OLS methods operate by minimizing the sum of squared residuals between computed coordinates and an assumed surface. PCA methods operate by performing an eigenvector analysis on the coordinates. In three-space, the eigenvector corresponding to the minimum eigenvalue is the vector normal to the coordinates. The results of using OLS and PCA to compute surface normals for DSMs are analyzed in Chapter 4. For completeness, however, I show how OLS may be used to compute a planar surface normal below.

First, assume accumulator-array SBF coordinates (x,y,z) can be expressed by the plane equation

$$z = Ax + By + C \tag{12}$$

where, A, B, and C are the x-, y-, and z-components of the vector normal to the plane. Since Equation 12 is a scaled form of the traditional plane equation, assume C has been scaled to take a value of -1 (negative to account for z positive in downward direction). Next, subtract the mean coordinate $(\bar{x}, \bar{y}, \bar{z})$ from each accumulator array coordinate to eliminate C, and establish a linear system of equations, shown in Equation 13 as

$$\begin{bmatrix} x_1 - \bar{x} & y_1 - \bar{y} \\ x_2 - \bar{x} & y_2 - \bar{y} \\ . & . \\ . & . \\ x_n - \bar{x} & y_n - \bar{y} \end{bmatrix} \begin{bmatrix} A \\ B \end{bmatrix} = \begin{bmatrix} z_1 - \bar{z} \\ z_2 - \bar{z} \\ . \\ . \\ z_n - \bar{z} \end{bmatrix} \tag{13}$$

where, n is the number of accumulator array coordinates. For the 2x2 example shown in Figure 17, n is 4. The unique, OLS solution to this problem may then be computed as

$$\begin{bmatrix} A \\ B \end{bmatrix} = (A_{sys}^T A_{sys})^{-1} A_{sys}^T b \tag{14}$$

where

$$A_{sys} = \begin{bmatrix} x_1 - \bar{x} & y_1 - \bar{y} \\ x_2 - \bar{x} & y_2 - \bar{y} \\ . & . \\ . & . \\ x_n - \bar{x} & y_n - \bar{y} \end{bmatrix} \tag{15}$$

and

$$b = \begin{bmatrix} z_1 - \bar{z} \\ z_2 - \bar{z} \\ . \\ . \\ z_n - \bar{z} \end{bmatrix}. \tag{16}$$

The OLS solution coefficients A and B may be used together with C to form the best-fit-plane's normal vector as

$$\vec{v} = \begin{bmatrix} A \\ B \\ -1 \end{bmatrix}. \tag{17}$$

This normal vector represents the best planar model of the accumulator array coordinates in a least-squares sense. If a unit surface-normal vector is desired, $\vec{v}$ may be divided by its norm to arrive at

$$\vec{n_s} = \begin{bmatrix} A \\ B \\ -1 \end{bmatrix} \Big/ \left\| \begin{bmatrix} A \\ B \\ -1 \end{bmatrix} \right\|. \tag{18}$$

The next two sections discuss applications of Pathfinder's air-water-interface modeling capability: (1) geometric reconstruction of seafloor coordinates, and (2) radiometric restoration of seafloor reflectance estimates.

3.3 Geometric Reconstruction

When the air-water interface is flat, seafloor coordinates computed by ALB systems contain no interface-induced steering errors. That is, when the air-water interface is known to be flat, Equation 1 can be used to compute seafloor coordinates with no error arising from the air-water interface. However, the air-water interface is rarely flat, as gravity and capillary waves create low- and high-frequency structures on the interface. These irregular air-water interfaces refract a system's laser pulse differently than flat interfaces, causing seafloor-coordinate computation error if Equation 1 is used instead of Equation 9. However, Equation 9 requires knowing ϕ_w and ω_w, which are not directly observable for the case of non-flat, air-water interfaces. As a result, these angles must be expressed in terms of the known scanner angle and in-air, off-nadir angle pertinent to a particular lidar and the air-water interface's orientation.

To derive expressions for these angles, start with Equation 9 and extract the SBF coordinate equation as shown.

$$\begin{bmatrix} X \\ Y \\ Z \end{bmatrix}_{SBF} = R_Z(\theta) \left(R_Y(\phi_A) \begin{bmatrix} 0 \\ 0 \\ l_A \end{bmatrix} + R_Y(\phi_w) R_X(\omega_w) \begin{bmatrix} 0 \\ 0 \\ l_W \end{bmatrix} \right) \tag{19}$$

Next, convert the SBF coordinate equation into vector notation by factoring out l_A and l_W from their respective terms and labeling the matrix-vector products as $\vec{i}$ and $\vec{r}$, respectively. This is shown in Equation 20 as

$$\begin{bmatrix} X \\ Y \\ Z \end{bmatrix}_{SBF} = l_A \vec{i} + l_W \vec{r} \tag{20}$$

where,

$$\vec{i} = R_Z(\theta) R_Y(\phi_A) \begin{bmatrix} 0 \\ 0 \\ 1 \end{bmatrix} \tag{21}$$

and

$$\vec{r} = R_Z(\theta) R_Y(\phi_w) R_X(\omega_w) \begin{bmatrix} 0 \\ 0 \\ 1 \end{bmatrix}. \tag{22}$$

Here, $\vec{i}$ may be interpreted as the incident unit vector on the water surface, and $\vec{r}$ may be interpreted as the in-water, refracted unit vector. In the SBF, computing $\vec{i}$ relies only on knowing systems' scanner and off-nadir angles. ALB systems may therefore determine it for every laser pulse. On the other hand, computing $\vec{r}$ relies on knowing systems' scanner angle and the in-water angles ϕ_w and ω_w. As previously mentioned, these angles are not directly observable, meaning systems may not determine $\vec{r}$ using

Equation 22 directly. Instead, systems may use Snell's law, extended to three dimensions. In [72], Glassner shows that the refracted vector lies in the plane whose normal is the cross-product of the incident and surface-normal vectors, and can be expressed as

$$\vec{r} = \eta\vec{i} + \left(\eta k - \sqrt{1 + \eta^2\left(k^2 - 1\right)}\right)\vec{n_s} \tag{23}$$

where:

$k =$ $-\vec{n_s} \cdot \vec{i}$
$\eta =$ n_{air}/n_{water}
$\vec{i}$: incident unit vector
$\vec{n_s}$: surface-normal unit vector, and
$\vec{r}$: refracted unit vector.

Equation 23 shows that the refracted unit vector depends on the incident unit vector and the surface-normal unit vector. Thus, computing $\vec{r}$ relies on knowing system parameters as well as the air-water-interface's 3D orientation. Systems that produce co-temporal, high-resolution SST measurements may estimate $\vec{n_s}$ and use Equation 23 to compute $\vec{r}$. Once $\vec{r}$ is known, Equation 20 may be used to compute SBF seafloor coordinates, which can then be substituted into Equation 9 to produce geodetic, seafloor coordinates as

$$\begin{bmatrix} N_P \\ E_P \\ D_P \end{bmatrix} = R_Z(\kappa)R_Y(\phi)R_X(\omega)\left(R_Z(\Delta\kappa)R_Y(\Delta\phi)R_X(\Delta\omega)\begin{bmatrix} X \\ Y \\ Z \end{bmatrix}_{SBF} + \begin{bmatrix} \Delta X \\ \Delta Y \\ \Delta Z \end{bmatrix}\right) + \begin{bmatrix} N_T \\ E_T \\ D_T \end{bmatrix}. \tag{24}$$

Using this method, ϕ_w and ω_w are implicitly computed when evaluating Equation 23. If explicit values are desired, they may be obtained by

$$\phi_w = \arcsin\left(\frac{r_x}{\sqrt{r_x^2 + r_z^2}}\right) \tag{25}$$

and

$$\omega_w = -\arcsin\left(\frac{r_y}{\sqrt{r_x^2 + r_y^2 + r_z^2}}\right) \tag{26}$$

where, $\vec{r} = [r_x, r_y, r_z]^T$.

A hybrid lidar system, like Pathfinder, is well suited to use this coordinate computation approach. Unlike current ALB systems that may only assume refracted trajectories based on incident vectors, Pathfinder may use its IR, Geiger-mode measurements to compute high-resolution DSMs of the water surface using the method outlined in Section 3.2. The DSM coordinates and the normal vectors computed from them enables Pathfinder to measure $\vec{i}$ and $\vec{n_s}$ simultaneously, allowing for computation of the refracted unit vector using Equation 23. Pathfinder's processing architecture was developed to accomplish this, as shown in Figure 18. In this hybrid processing architecture, the green, linear-mode, waveform-resolved channel operates in parallel with the IR, Geiger-mode channel. The green channel operates as it would conventionally: green backscattered photons are detected, amplified, and digitized before being sent to the CPU. The IR channel, which I designed to supplement the existing green channel, is responsible for collecting interface measurements and computing interface DSMs. The GmAPD camera collects IR backscattered photons and determines TOF measurements for each pixel in its focal plane array. Interface DSM coordinates and normals are then computed and registered with co-temporal green channel data. Finally, the registered green and IR data is passed to the GPU, where seafloor coordinates are rapidly computed in parallel using Equation 24.

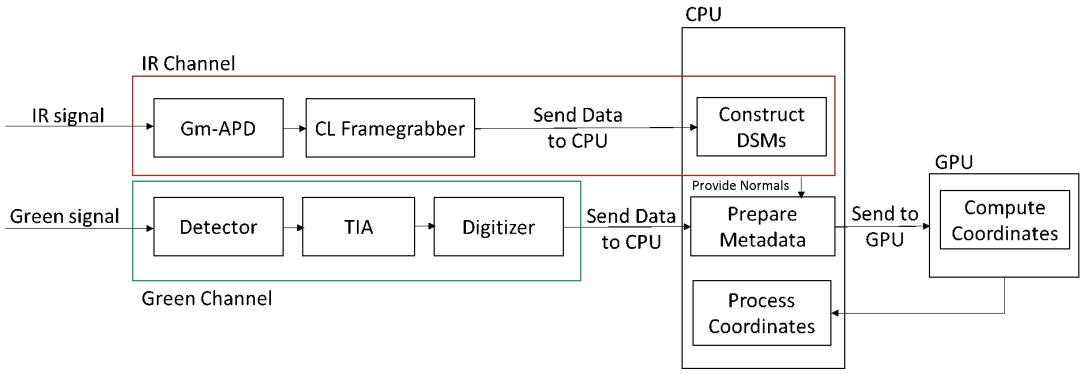

Figure 18: Combining a linear-mode system with a Geiger-mode system allows for computing seafloor coordinates that account for air-water interface orientation.

3.4 Radiometric Restoration

Waveform-resolved ALB systems can estimate seafloor reflectance at the laser's wavelength by inverting the radiative transfer equation and solving for ρ (Equation 2). As discussed in Section 2.3, this inversion involves radiometrically calibrating the system and constraining the inversion with assumptions and estimates of various parameters. Importantly, the detected backscatter from a transmitted pulse may be viewed as the output of a linear, shift-variant system. The transmitted pulse, itself a convolution of a unit impulse with the laser's pulse shape, is convolved with the lidar's impulse response function and the shift-variant BLTF (Figure 8) to produce the observed signal. A mathematical model describing this relationship is shown in Equation 27 as

$$g = f * h_{BLTF} = (\delta * h_{irf} * h_{laser}) * h_{BLTF} \tag{27}$$

where f is the unit-impulse convolved with the lidar's impulse response function (h_{irf}) and laser pulse shape (h_{laser}), h_{BLTF} is the BLTF, and g is the observed signal. The lidar's impulse response function accounts for all radiometric losses the transmitted pulse undergoes during its roundtrip path to the seafloor. The BLTF describes the cascades of transfer functions, in the optical and electrical domains, that affect the

observed signal's shape. It is shift-variant because, among other things, the air-water interface changes for each pulse. Equation 28 expresses it as a convolution of its two components, the environmental transfer function and the system transfer function:

$$h_{BLTF} = h_{env} * h_{sys} \tag{28}$$

where, h_{env} is the environmental transfer function and h_{sys} is the ALB-system transfer function.

The BLTF's individual transfer functions affect ALB system performance by introducing distortion and noise to the observed signal. System-component transfer functions are often well known and can be modeled to simulate their effect on detected signals [57]; however, environmental transfer functions are not as well understood. These transfer functions have noise components and signal-stretching components [37]. While noise profiles arising from solar background, glinting off the water surface, and upwelling radiance from the water column are modeled well [44], stretching effects from the air-water interface and water-column scattering are not. Some work has been published regarding water-column stretching [73, 37], but very little has been published about stretching induced by the interface.

Stretching from the air-water-interface transfer function arises from temporal interaction with the interface that is longer than the pulse's temporal extent. In other words, for a pulse with 2-ns temporal extent, air-water-interface stretching occurs when interface interaction is longer than 2 ns. This is almost always true, meaning nearly all ALB signals contain some interface-induced stretching. The lone exception is when the interface is oriented perfectly normal to the transmitted pulse. In this case, the air-water-interface transfer function is an impulse, which introduces no stretching when convolved with an input. In all other cases, the air-water-interface transfer function is a function with some other shape, causing a broadening of the detected signal's temporal extent.

The main cause of interface-induced broadening is geometric stretching. Because systems employ off-nadir pointing angles, inclined incidence stretches the pulse consistent with the geometry. Here, the time required for the pulse to pass through the interface is directly related to its angle of incidence relative to the interface. For a tilted interface oriented along the pointing vector and containing no high-frequency content, the interaction time may be expressed as

$$t_{interaction} = t_{pulse} + \frac{w_{beam}}{c} \tan\theta \tag{29}$$

where:

t_{pulse} : temporal extent of pulse,
w_{beam} : spatial extent of pulse at interface,
c : speed of light in air, and
θ_{inc} : angle of incidence relative to interface's normal vector.

Equation 29 shows that when pulses are normally incident to the interface ($\theta_{inc} = 0$), their interaction time is equal to their temporal extent. However, when pulses are inclined relative to the interface ($\theta_{inc} \neq 0$), their interaction time is greater than their temporal extent by an amount equal to $\frac{w_{beam}}{c} \tan\theta_{inc}$. This value represents the stretching introduced by the interface, and is shown in Equation 30 as

$$t_{stretch} = \frac{w_{beam}}{c} \tan\theta_{inc}. \tag{30}$$

Using the fact that the pulse's wavefront bends across the interface to maintain continuity, the interface's stretching function may be modeled as a triangle function [50], whose temporal width is equal to $t_{stretch}$. When θ_{inc} is 0, $t_{stretch}$ is 0, effectively making the triangle an impulse. When θ_{inc} is nonzero, $t_{stretch}$ depends on the beam's spatial footprint and its angle of incidence.

A system's beam divergence, flying height, and off-nadir angle together with the ALB-community's flat-water assumption establish the triangle function modeling the

air-water-interface. For a system flying at 400 m and using a 20-degree off-nadir angle with 7-mrad beam divergence, Equation 30 may be evaluated as

$$t_{stretch} = \frac{(400m)(0.007)/_{cos(20^\circ)}}{0.3m/ns} \tan 20^\circ = 3.6ns, \tag{31}$$

where the beam's spatial extent, w_{beam}, is computed as the major axis of an ellipse oriented parallel to the pointing vector. This stretch value may then be used as the triangle function's width, and the resulting triangle function models the air-water-interface transfer function for this ALB system. As discussed in Section 2.3, uncompensated stretching degrades seafloor reflectance estimates. Therefore, the stretching introduced by this transfer function may be removed by deconvolving it from the observed signal. However, this deconvolution kernel is only valid when the interface is flat because Equation 30 only allows $t_{stretch}$ to vary as a function of system parameters. This limitation does not accommodate a scenario in which the interface incidence angle and the system's off-nadir angle are different, occurring when the interface is tilted. This limitation also does not accommodate a scenario in which high-frequency SST structures exist on the interface. Therefore, a new formulation is needed that compensates for the air-water interface. Hybrid systems, like Pathfinder, that construct high-resolution DSMs of the air-water-interface while detecting waveform-resolved signals offer a path to accomplishing this.

To derive a new formulation using cotemporally-constructed DSMs, first start by expanding the BLTF's environmental component in Equation 28 into its constituent transfer functions, shown in Equation 32 as

$$h_{BLTF} = (h_{atm} * h_{int} * h_{wc} * h_{sf}) * h_{sys} \tag{32}$$

where:

h_{atm} : atmospheric transfer function

h_{int} : air-water-interface transfer function,
h_{wc} : water-column transfer function, and
h_{sf} : seafloor transfer function.

Next, rearrange and group the right-hand-side of Equation 31 as

$$h_{BLTF} = h_{int} * h_{rest} \tag{33}$$

where $h_{rest} = h_{atm} * h_{wc} * h_{sf} * h_{sys}$. Equation 33 purposefully separates the air-water-interface transfer function from the rest of the individual transfer functions, which are then grouped into h_{rest}. Next, Equation 33 may be substituted into Equation 27, resulting in

$$g = f * (h_{int} * h_{rest}). \tag{34}$$

For flat air-water interfaces, h_{int} is known. It is a triangle function with temporal width computed by Equation 30. Therefore, the only unknown term in Equation 34 is h_{rest}; it may be estimated using a system identification approach. The Fourier transform of Equation 34 to transform to the frequency domain, as shown in 35,

$$G_{flat} = F H_{int_{flat}} H_{rest} \tag{35}$$

may be rearranged to estimate H_{rest}, shown in Equation 36 as

$$\hat{H}_{rest} = \frac{G_{flat}}{F H_{int_{flat}}} \tag{36}$$

where:

F is the Fourier transform of the transmitted pulse,

G_{flat} is the Fourier transform of an observed waveform, g_{flat}, arising from flat air-water interfaces, and

$H_{int_{flat}}$ is the Fourier transform of a flat, air-water-interface transfer function.

Since $h_{int_{flat}}$ is a triangle in the time domain, $H_{int_{flat}}$ is a sinc^2 in the frequency domain. The inverse Fourier transform may then be applied to Equation 36, estimating h_{rest}, shown in Equation 37 as

$$\hat{h}_{rest} = \mathcal{F}^{-1}\left(\frac{G_{flat}}{FH_{int_{flat}}}\right). \tag{37}$$

Equation 37 may be evaluated during flat interface conditions to estimate h_{rest}. Determining flat interface conditions may be accomplished by using co-temporal SST measurements. DSMs constructed from these measurements contain surface normal vectors describing the interface's orientation. Since a hybrid system like Pathfinder registers DSM data with each transmitted pulse, observed waveforms whose registered DSM data satisfies a "flatness" threshold may be treated as g_{flat} waveforms. Taking the Fourier transform of g_{flat} enables evaluation of Equation 37.

Next, assume the air-water interface is wavy. This changes the Fourier transform of Equation 34. The new result may be written as

$$G_{wavy} = FH_{int_{wavy}}H_{rest} \tag{38}$$

where

$H_{int_{wavy}}$ is the Fourier transform of the wavy, air-water-interface transfer function, and

G_{wavy} is the Fourier transform of an observed waveform, g_{wavy}, arising from the wavy air-water interface.

Since $\hat{H}_{rest}$ from the flat interface analysis estimates H_{rest}, Equation 36 may be substituted into Equation 38, resulting in

$$G_{wavy} = FH_{int_{wavy}} \frac{G_{flat}}{FH_{int_{flat}}}. \tag{39}$$

This expression may then be simplified and rearranged to estimate $H_{int_{wavy}}$, shown in Equation 40 as

$$\hat{H}_{int_{wavy}} = \frac{G_{wavy} H_{int_{flat}}}{G_{flat}}. \tag{40}$$

The final step is to take the inverse Fourier transform of Equation 40, resulting in the estimate for the wavy, air-water-interface transfer function, shown in Equation 41 as

$$\hat{h}_{int_{wavy}} = \mathcal{F}^{-1} \left(\frac{G_{wavy} H_{int_{flat}}}{G_{flat}} \right). \tag{41}$$

This equation may then be used to estimate the air-water-interface transfer function during non-flat conditions. However, the analysis used to reach this result assumes h_{rest} is constant across pulses. This is obviously not true because the water-column and seafloor transfer functions are shift-variant. However, this assumption may be removed by restricting g_{wavy} and g_{flat} to their respective interface return signals. Doing this removes the contributions of the shift-variant transfer functions, h_{wc} and h_{sf}, to h_{rest}. Now, the only transfer functions contributing to h_{rest} are the atmospheric transfer function (h_{atm}) and the system transfer function (h_{sys}). As a simplifying assumption, these transfer functions are treated as constant, and Equation 41 may be used to estimate wavy, air-water-interface transfer functions. In turn, these estimates of interface transfer functions can be used to improve seafloor reflectance estimates either by deconvolving them from the full, waveform-resolved signal or by using their temporal extent to improve STF estimates used in Equation 3. Chapter 4 contains results evaluating this method.

The new formulation for determining air-water-interface transfer functions outlined in this Section only uses the high-resolution, co-temporal SST measurements to

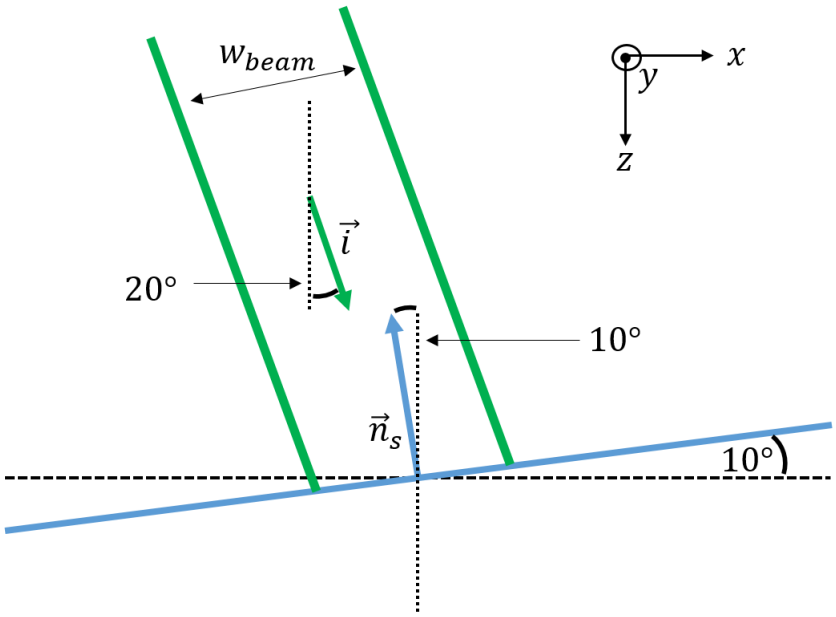

Figure 19: The angle between the incident vector and the interface's normal vector determines the amount of stretching incident beams experience when interacting with low-frequency tilted interfaces.

determine flat interface conditions. Then, evaluating many equations ensues to produce the transfer function estimate. A far superior method in terms of computational complexity, and possibly accuracy, would be to estimate the stretch function directly from the spatial-domain DSM construction. To the best of my knowledge, this has not been done. In this work, I discuss the simplest case of low-frequency tilts.

Consider the case shown in Figure 19.Here, a low-frequency tilted interface is oriented along the pointing vector (i.e. in the XZ-plane). This interface is tilted toward the system at a 10-degree angle. Further, assume the same system parameters used for Equation 31 (i.e. altitude = 400 m, off-nadir angle = 20°, and beam divergence = 7 mrad). If this system uses high-resolution SST measurements to construct accurate DSMs, the DSM produced for this case should be very close to a planar surface whose normal vector is tilted toward the system at a 10-degree angle. Upon recognizing this planar surface, a system could evaluate Equation 30 with θ_{inc} computed as

$$\theta_{inc} = \arccos(\vec{i} \cdot \vec{n_s}) \tag{42}$$

where $\vec{i}$ is the incident unit vector and $\vec{n_s}$ is the surface-normal unit vector produced by the the DSM construction technique. For this simple example, perfect interface reconstruction would produce $theta_{inc} = 10°$, resulting in a computed stretch value of $1.75ns$. This value is equal to the true stretch value. Then when estimating ρ, it may either be used to estimate STF in Equation 3 or used as the triangle function's temporal width and deconvolved from the observed signal. For comparison, had a flat interface been assumed, the stretch value would have been $3.62ns$, producing inaccurate estimates of STF and the triangle function, both of which would cause inaccurate estimates of ρ. Chapter 4 also contains results using this method.

This section and the previous one have shown how a hybrid system may use DSMs of the air-water-interface to improve the accuracy of seafloor coordinate and reflectance estimates. The next, and final, section of this Chapter details how to characterize and assess the accuracy of such a system.

3.5 Determining System Accuracy

Deriving Equation 9 now makes it possible to characterize interface-induced error that propagates to seafloor coordinates. Since irregular air-water interfaces steer laser pulses to a position on the seafloor according to Equation 9, one way to quantify interface-induced error is to compare the coordinates computed by Equation 9 and Equation 1 in the presence of waves. For simplicity, consider the case of a low-frequency wave with structure only oriented along the pointing vector. Figure 20 shows the effect of varying the wave's slope on the difference in coordinates computed by the two equations for a flat seafloor. When failing to account for wavy interfaces, Equation 1 results in coordinate error that linearly increases as depth increases. Furthermore, as the wave's slope increases, the rate of change in seafloor

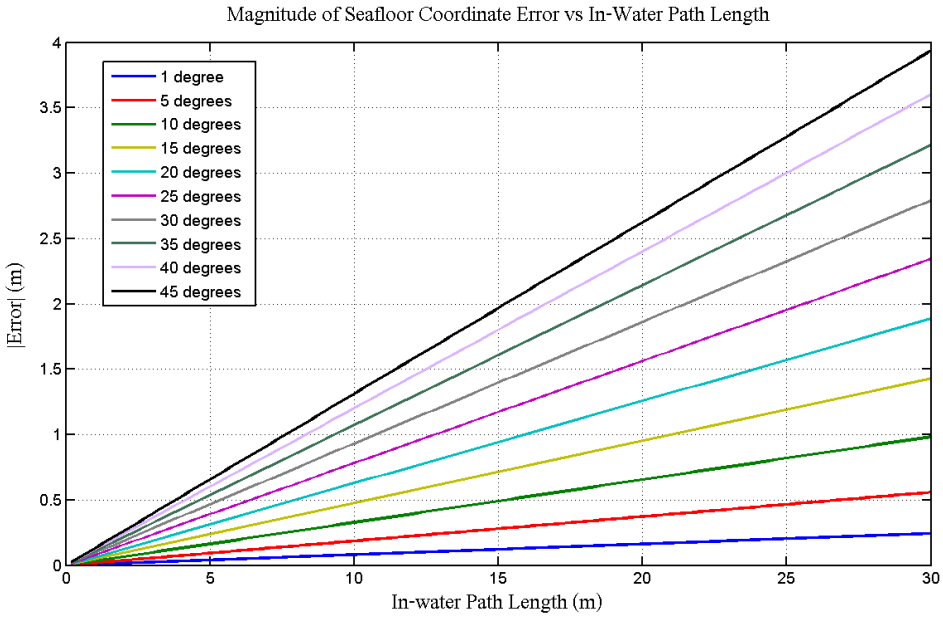

Figure 20: The magnitude of seafloor coordinate error resulting from a tilted surface increases linearly as a function of in-water path length, with slope related to the magnitude of the wave's tilt.

coordinate error also increases. At a shallow depth of 10 meters, an uncompensated wave slope of 30 degrees causes a seafloor coordinate error of roughly 1 meter. This error magnitude would not meet IHO standards.

The errors computed in Figure 20 are only a function of air-water interface tilt. Errors in lidar pointing and ranging, and in navigation, convolve with errors arising from air-water interface effects to degrade the overall accuracy of seafloor coordinates. Recognizing this, it is important to compensate for all errors as best possible, and to quantify the total uncertainty (or accuracy) of an ALB system through propagation of variances from all measurements onto the point coordinates. One way to do this is to derive a new TPU model, based on Tuell's model [59], to account for the air-water interface . This can be done by starting with Equation 9 and deriving all of its partial derivatives with respect to each variable. Then, all of the measurement variances and covariances can be used to fill the measurement cofactor matrix. The result of this process is similar to Equation 4, and is shown in Equation 43 as

$$\widetilde{\Sigma_P} = \tilde{J}\widetilde{\Sigma_M}\tilde{J}^T \tag{43}$$

where:

$\widetilde{\Sigma_P}$: TPU matrix (3x3) filled with positional variances and covariances,
$\tilde{J}$: Jacobian matrix (3x18) formed with partial derivatives, and
$\widetilde{\Sigma_M}$: Cofactor matrix (18x18) formed with measurement variances and co-variances.

In this new formulation, the Jacobian and cofactor matrices, $\tilde{J}$ and $\widetilde{\Sigma_M}$, may be constructed as

$$\tilde{J} = \begin{bmatrix} \frac{\partial N}{\partial \kappa} & \frac{\partial N}{\partial \phi} & \dots & \dots & \frac{\partial N}{\partial \phi_w} & \frac{\partial N}{\partial \omega_w} \\ \frac{\partial E}{\partial \kappa} & \frac{\partial E}{\partial \phi} & \dots & \dots & \frac{\partial E}{\partial \phi_w} & \frac{\partial E}{\partial \omega_w} \\ \frac{\partial D}{\partial \kappa} & \frac{\partial D}{\partial \phi} & \dots & \dots & \frac{\partial D}{\partial \phi_w} & \frac{\partial D}{\partial \omega_w} \end{bmatrix} \tag{44}$$

and

$$\widetilde{\Sigma_M} = \begin{bmatrix} \sigma_\kappa^2 & \sigma_\kappa\sigma_\phi & \dots & \dots & \dots & \sigma_\kappa\sigma_{\phi_w} & \sigma_\kappa\sigma_{\omega_w} \\ \sigma_\phi\sigma_\kappa & \sigma_\phi^2 & \dots & \dots & \dots & \sigma_\phi\sigma_{\phi_w} & \sigma_\phi\sigma_{\omega_w} \\ . & & . & & & & . \\ . & & & . & & & . \\ . & & & & . & & . \\ \sigma_{\phi_w}\sigma_\kappa & \sigma_{\phi_w}\sigma_\phi & \dots & \dots & \dots & \sigma_{\phi_w}^2 & \sigma_{\phi_w}\sigma_{\omega_w} \\ \sigma_{\omega_w}\sigma_\kappa & \sigma_{\omega_w}\sigma_\phi & \dots & \dots & \dots & \sigma_{\omega_w}\sigma_{\phi_w} & \sigma_{\omega_w}^2 \end{bmatrix}, \tag{45}$$

resulting in a new TPU matrix containing the variances and covariances of a point's northing, easting, and down coordinates, shown in Equation 46 as

$$\widetilde{\Sigma_P} = \begin{bmatrix} \sigma_N^2 & \sigma_N\sigma_E & \sigma_N\sigma_D \\ . & \sigma_E^2 & \sigma_E\sigma_D \\ (sym) & . & \sigma_D^2 \end{bmatrix}. \tag{46}$$

In this formulation, the tildes over each matrix signify their change from Equation 4. Specifically, the cofactor measurement matrix is now an 18x18-element matrix and the Jacobian is a 3x18-element matrix after including the new variable ω_w. These changes produce different variance and covariance entries in $\widetilde{\Sigma_P}$ compared to Σ_P. Additionally, though the navigation, pointing, and boresight-alignment measurement variances and covariances do not change, the measurement variances and covariances associated with ϕ_w do change in this model since ϕ_w is actually measured now, as opposed to being computed directly from ϕ_A in Tuell's method [59]. By arranging the variables in the same order as the previous formulation and simply adding ω_w to the end, the upper 16x16 elements in this formulation are equivalent to the upper 16x16 elements in Equation 6. This may be expressed in block matrix form as,

$$\widetilde{\Sigma_P} = \begin{bmatrix} \Sigma_{sys} & . \\ . & \Sigma_{interface} \end{bmatrix}. \tag{47}$$

where,

$$\Sigma_{sys} = \Sigma_{P_{(1:16,1:16)}} = \widetilde{\Sigma_P}_{(1:16,1:16)} \tag{48}$$

and

$$\Sigma_{interface} = \begin{bmatrix} \sigma^2_{\phi_w} & \sigma_{\phi_w}\sigma_{\omega_w} \\ \sigma_{\omega_w}\sigma_{\phi_w} & \sigma^2_{\omega_w} \end{bmatrix}. \tag{49}$$

Here, Σ_{sys} may be interpreted as the variances and covariances arising from measurements of the "system", such as navigation, pointing, and ranging measurements. On the other hand, $\Sigma_{interface}$ may be interpreted as the variances and covariances arising from air-water-interface measurements. Therefore, Equation 43 may be used to identify and quantify how any measurement error, including air-water-interface

measurement error, affects seafloor coordinate error. To do this, however, techniques for computing the variances and covariances of ϕ_w and ω_w must be developed to fill their measurement cofactor-matrix entries appropriately.

Computing the measurement variances and covariances of ϕ_w and ω_w requires developing explicit formulations for ϕ_w and ω_w. For the OLS-based, DSM-construction technique presented in Section 3.2, this may be done by first substituting $\vec{n_s}$, Equation 18, and $\vec{i}$, Equation 21, into Equation 23 to solve for $\vec{r}$. Then, the x-, y-, and z-components of $\vec{r}$ may be used in Equation 25 and Equation 26, resulting in explicit expressions for ϕ_w and ω_w, shown as

$$\phi_w = \arcsin\left(\frac{\eta\sin(\theta)\sin(\phi_A) + \chi A}{\sqrt{(\eta\sin(\theta)\sin(\phi_A) + \chi A)^2 + (\eta\cos(\phi_A) - \chi)^2}}\right) \tag{50}$$

and

$$\omega_w = -\arcsin\left(\frac{\eta\sin(\theta)\sin(\phi_A)+\chi B}{\sqrt{(\eta\sin(\theta)\sin(\phi_A)+\chi A)^2+(\eta\sin(\theta)\sin(\phi_A)+\chi B)^2+(\eta\cos(\phi_A)-\chi)^2}}\right), \tag{51}$$

where:

χ : function of A, B, ϕ_A, and θ that can be found in Appendix A.

By using the law of variance propagation for both ϕ_w and ω_w, estimates of $\sigma^2_{\phi_w}$, and $\sigma^2_{\omega_w}$ may then be determined as

$$\hat{\sigma}^2_{\phi_w} = \begin{bmatrix} \frac{\partial\phi_w}{\partial\theta} & \frac{\partial\phi_w}{\partial\phi_A} & \frac{\partial\phi_w}{\partial A} & \frac{\partial\phi_w}{\partial B} \end{bmatrix} \begin{bmatrix} \sigma^2_\theta & \sigma_\theta\sigma_{\phi_A} & \sigma_\theta\sigma_A & \sigma_\theta\sigma_B \\ . & \sigma^2_{\phi_A} & \sigma_{\phi_A}\sigma_A & \sigma_{\phi_A}\sigma_B \\ . & . & \sigma^2_A & \sigma_A\sigma_B \\ (sym) & . & . & \sigma^2_B \end{bmatrix} \begin{bmatrix} \frac{\partial\phi_w}{\partial\theta} \\ \frac{\partial\phi_w}{\partial\phi_A} \\ \frac{\partial\phi_w}{\partial A} \\ \frac{\partial\phi_w}{\partial B} \end{bmatrix} \tag{52}$$

and

$$\hat{\sigma}^2_{\omega_w} = \begin{bmatrix} \frac{\partial \omega_w}{\partial \theta} & \frac{\partial \omega_w}{\partial \phi_A} & \frac{\partial \omega_w}{\partial A} & \frac{\partial \omega_w}{\partial B} \end{bmatrix} \begin{bmatrix} \sigma^2_\theta & \sigma_\theta \sigma_{\phi_A} & \sigma_\theta \sigma_A & \sigma_\theta \sigma_B \\ . & \sigma^2_{\phi_A} & \sigma_{\phi_A} \sigma_A & \sigma_{\phi_A} \sigma_B \\ . & . & \sigma^2_A & \sigma_A \sigma_B \\ (sym) & . & . & \sigma^2_B \end{bmatrix} \begin{bmatrix} \frac{\partial \omega_w}{\partial \theta} \\ \frac{\partial \omega_w}{\partial \phi_A} \\ \frac{\partial \omega_w}{\partial A} \\ \frac{\partial \omega_w}{\partial B} \end{bmatrix}. \quad (53)$$

These equations are formulated similarly to the TPU model presented previously in this section. The partial derivatives of Equations 50 and 51 with respect to θ, ϕ_A, A, and B fill the Jacobian matrix entries. Then, the measurement variances and covariances of these variables are used to fill the measurement cofactor matrix, which is identical for each equation. Combining these equations into one system produces a 2x2 matrix that estimates $\Sigma_{interface}$, shown in Equation 54 as

$$\hat{\Sigma}_{interface} = \begin{bmatrix} \frac{\partial \phi_w}{\partial \theta} & \frac{\partial \phi_w}{\partial \phi_A} & \frac{\partial \phi_w}{\partial A} & \frac{\partial \phi_w}{\partial B} \\ \frac{\partial \omega_w}{\partial \theta} & \frac{\partial \omega_w}{\partial \phi_A} & \frac{\partial \omega_w}{\partial A} & \frac{\partial \omega_w}{\partial B} \end{bmatrix} \begin{bmatrix} \sigma^2_\theta & \sigma_\theta \sigma_{\phi_A} & \sigma_\theta \sigma_A & \sigma_\theta \sigma_B \\ . & \sigma^2_{\phi_A} & \sigma_{\phi_A} \sigma_A & \sigma_{\phi_A} \sigma_B \\ . & . & \sigma^2_A & \sigma_A \sigma_B \\ (sym) & . & . & \sigma^2_B \end{bmatrix} \begin{bmatrix} \frac{\partial \phi_w}{\partial \theta} & \frac{\partial \omega_w}{\partial \theta} \\ \frac{\partial \phi_w}{\partial \phi_A} & \frac{\partial \omega_w}{\partial \phi_A} \\ \frac{\partial \phi_w}{\partial A} & \frac{\partial \omega_w}{\partial A} \\ \frac{\partial \phi_w}{\partial B} & \frac{\partial \omega_w}{\partial B} \end{bmatrix}. \quad (54)$$

The diagonal entries of $\hat{\Sigma}_{interface}$ are variance estimates of ϕ_w and ω_w; the symmetric, off-diagonal entry is their covariance estimate. The cofactor matrix entries associated with θ and ϕ_A come from lidar pointing data, while entries associated with A and B come from the DSM construction procedure. The latter reveals exactly what one would expect: the accuracy of ϕ_w and ω_w depends on the accuracy of the computed normal vector, and by extension, the DSM interface measurements.

The variances and covariance of A and B must be computed to use Equation 54. For a hybrid lidar system, they depend on GmAPD interface measurements and

the propagation of interface measurement variances through OLS. To compute them, first recognize the OLS regression in Equation 13 is implicitly of the form $f(\vec{v}, \vec{x}) = 0$, where $\vec{v}$ is a vector of inputs and $\vec{x}$ is a vector of outputs. In this formulation, the input vector, $\vec{v}$, contains the coordinates used in the OLS regression; and, the output vector, $\vec{x}$, contains the normal vector coefficients, A and B. As shown in [74, 75], the law of propagation of variance for this class of problems may then be expressed as

$$J_o \Sigma_o J_o^T = J_I \Sigma_I J_I^T \tag{55}$$

where:

Σ_o : output covariance matrix,
J_o : partial of f with respect to the outputs,
Σ_I : input covariance matrix, and
J_I : partial of f with respect to the inputs.

Here, the input covariance matrix, Σ_I, contains the variances and covariances of the coordinates used in the OLS regression. The output covariance matrix, Σ_o, contains the variances and covariances of A and B. In other words, Σ_o is the desired matrix. Equation 55 may then be rearranged, solving for Σ_o as

$$\Sigma_o = \left(J_o^T J_o\right)^{-1} J_o^T J_I \Sigma_I J_I^T J_o \left(J_o^T J_o\right)^{-1}. \tag{56}$$

For an OLS regression of n coordinates, $\vec{v}$ contains 3n entries. When $\vec{v}$ is arranged such that, $\vec{v} = [x_1, y_1, z_1, x_2, y_2, z_2, ..., x_n, y_n, z_n]^T$, J_I, J_o, and Σ_I may be constructed as

$$J_I = \begin{bmatrix} A & B & -1 & 0 & ... & & ... & & ... & & 0 \\ 0 & ... & 0 & A & B & -1 & 0 & ... & & ... & 0 \\ . & & & & & & & & & & 0 \\ 0 & ... & & ... & & ... & & 0 & A & B & -1 \end{bmatrix} \tag{57}$$

$$J_o = A_{sys} = \begin{bmatrix} x_1 - \bar{x} & y_1 - \bar{y} \\ x_2 - \bar{x} & y_2 - \bar{y} \\ . & . \\ . & . \\ x_n - \bar{x} & y_n - \bar{y} \end{bmatrix}, \tag{58}$$

and

$$\Sigma_I = \begin{bmatrix} \Sigma_1 & ... & 0 \\ . & \Sigma_2 & . \\ . & . & . \\ 0 & ... & \Sigma_n \end{bmatrix}, \tag{59}$$

where, Σ_i is the 3x3 TPU matrix of the ith surface coordinate in the OLS regression. Assuming independent coordinates, Σ_I is a block diagonal matrix. Appendix B contains these derivations. Using these results, evaluating Equation 56 estimates the variances and covariance of A and B, which may be used to estimate air-water-interface uncertainty, $\Sigma_{interface}$. The estimate of $\Sigma_{interface}$ may then be used in the new, 18x18 TPU formulation to compute seafloor coordinate uncertainty, $\widetilde{\Sigma_P}$, in the presence of waves.

Although the listed equations in this process are specific to my DSM construction technique, the process may be generalized to any ALB system estimating SST to perform air-water-interface refraction. This generalized process is summarized as follows:

(1) Determine the lidar's in-air ranging variance to the air-water interface.

(2) Compute TPU matrix for each SST coordinate using upper 15x15 system in Equation 4 or 43.

(3) Propagate coordinate uncertainties through surface-normal computation procedure to variances and covariances of surface normal components.

(4) Propagate surface normal uncertainty to air-water-interface uncertainty (i.e. compute $\Sigma_{interface}$).

(5) Propagate air-water-interface uncertainty to seafloor coordinate uncertainty using full, 18x18 system in Equation 43.

Equation numbers are not included for steps 3 and 4 because they are specific to a system's DSM construction technique. For the OLS-based method presented in this thesis, step (3) corresponds to Equation 56 and step (4) corresponds to Equation 54. Nonetheless, this process represents the first time in the field of ALB that systems' surface-measurement uncertainty may be propagated to seafloor coordinates. Thus, for the first time, the effects of irregular air-water interfaces on ALB seafloor-coordinate accuracy may be characterized and computed. Figure 21 illustrates this process.

To facilitate comparing different DSM construction techniques, it is convenient to reduce $\widetilde{\Sigma_P}$ to a single parameter. As presented in Section 2.4, one common choice for this parameter is SAS_{gg} (Equation 8). For a given system, better DSM construction techniques will produce smaller SAS_{gg} values. This is because higher-accuracy DSMs improve the estimates of ϕ_w and ω_w, resulting in smaller entries of $\Sigma_{interface}$. In turn, because the elements in Σ_{sys} are fixed for a given system, a decrease in the values of $\Sigma_{interface}$ produces smaller values on the main diagonal of $\widetilde{\Sigma_P}$. Thus, SAS_{gg} will be smaller. Figure 22 graphically illustrates the benefit of accurately constructing DSMs, computing ϕ_w and ω_w, and estimating $\sigma^2_{\phi_w}$ and $\sigma^2_{\omega_w}$. Here, the red vectors represent the magnitude of the error vector and the red circles represent the magnitude of SAS_{gg}. The left side of Figure 22 depicts the case where the air-water interface is not measured (i.e. when using Equation 1). The dashed vector represents the computed

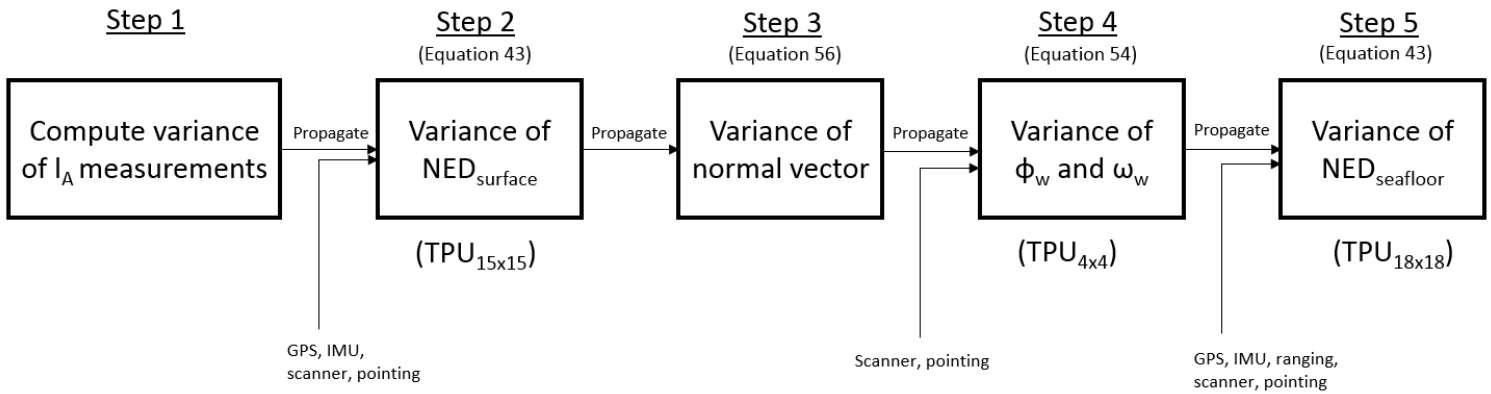

Figure 21: A lidar's surface measurement uncertainty may be propagated to seafloor coordinate uncertainty for the first time using new TPU framework. Note: Equation numbers provided for Steps 3 and 4 are specific to the OLS-based DSM-construction technique presented in Section 3.2.

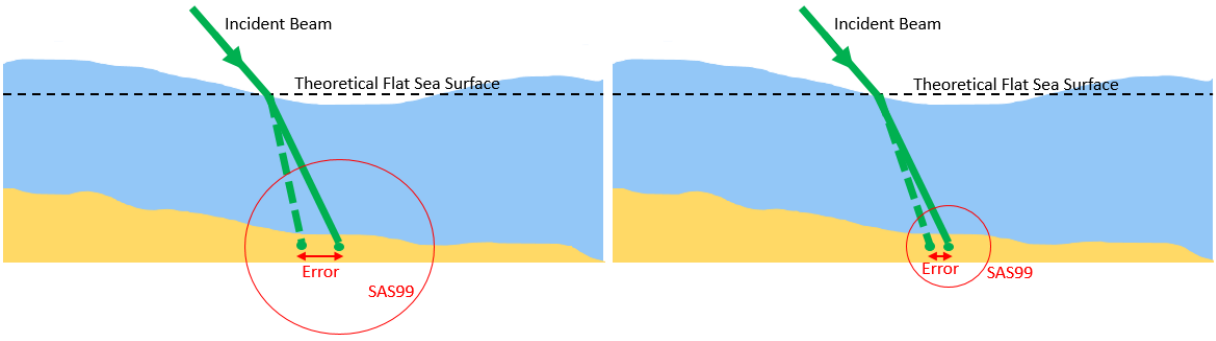

Figure 22: The magnitude of seafloor-coordinate error and uncertainty decrease as in-water steering-angle measurement accuracy increases and variance decreases.

point when assuming a flat air-water interface. The solid green vectors show the true location of the point – if ϕ_w and ω_w are perfectly known. The right side of Figure 22 shows the case wherein a DSM is constructed and ϕ_w and ω_w are measured with known variance $\sigma^2_{\phi_w}$ and $\sigma^2_{\omega_w}$. This illustration shows that for a given lidar and for a particular air-water-interface measurement technique, seafloor coordinate error and uncertainty are minimized when ϕ_w and ω_w are measured as accurately as possible.

Finally, since ALB-system, seafloor-image quality depends on the accuracy of computed seafloor points, this TPU framework allows for relating DSM quality to seafloor image quality. Images produced from coordinates with higher accuracy will have smaller SAS_{99}, on average, than images produced from coordinates with less accuracy. Thus, the average SAS_{99} value of seafloor coordinates used in an image may serve as an image-quality metric. Moreover, as just shown, DSM accuracy is directly related to SAS_{99}. Better construction techniques yield smaller SAS_{99} values, while worse techniques yield larger SAS_{99} values. Therefore, computing SAS_{99} from the TPU matrices enables relating changes in DSM construction techniques to changes in seafloor image quality. Chapter 4 contains results relating DSM and image quality via SAS_{99}.

CHAPTER IV

EXPERIMENT AND RESULTS

This chapter presents the experiments and simulations performed to assess Pathfinder's capabilities during wavy water conditions. These experiments and simulations evaluate the new math models presented in Chapter 3. The chapter begins by detailing the experiments designed to evaluate the coordinate-computation and accuracy-assessment techniques. Results of these experiments are then presented and discussed. The chapter then details the simulations designed to evaluate the reflectance estimation technique. Results of these simulations are then presented and discussed. After validating the new math models, the seafloor coordinate-computation and reflectance-estimation techniques are unified into one restoration procedure for seafloor imaging. The chapter concludes by detailing the simulations performed to evaluate the restoration procedure and presents the corresponding results.

4.1 Data Collection Campaign

With the assistance of several EOSL colleagues, I performed experiments with Pathfinder at the water tank facility in Georgia Tech's Love Manufacturing Building. This facility has a large fresh-water tank (25' x 40' x 25') and serves as a testing environment for water-related research activities. The goal of the experiments was to characterize the accuracy of a hybrid lidar's computed coordinates and to identify possible strategies for mitigating sea surface effects.[1] Using the new processing architecture described in Chapter 3, Pathfinder modeled the air-water-interface during calm and wavy conditions using its GmAPD measurements and registered the resulting DSMs with its co-temporal, waveform-resolved data. Then, Pathfinder used algorithms based on

the novel methods described in Chapter 3 to compute tank floor coordinates (hereafter called "floor coordinates"). Results were compared to truth data recorded by a witness camera. To the best of my knowledge, these experiments are the first demonstrating the use of high-resolution GmAPD measurements to reconstruct the air-water interface, to correct the green lidar's computed seafloor coordinate, and to identify interface-induced pulse stretching in green, waveform-resolved signals. Seafloor reflectance estimation and imaging were not part of the experiments.

Figure 23 shows Pathfinder at the water tank facility. Pathfinder, installed on scaffolding above the tank, was stationary and had no scanning capabilities. It was 3 meters above the water's surface and was oriented 20-degrees off-nadir. This configuration ensured that Pathfinder's green and IR beams were co-located on the water surface and within their respective receiver's FOV. Figure 24 shows spot diagrams of the green and IR beams relative to the GmAPD camera's FOV at 3.19 m, the configured imaging distance to the water surface. At this distance, the green beam, represented by the blue circle, was 12 cm wide; and, the IR beam, represented by the green circle, was 38 cm wide. The camera's FOV, represented by the black square in both diagrams, was 23 cm wide, which was larger than the green beam, but smaller than the IR beam. Since the camera's image resolution was 32x32, each pixel was spaced by 0.72 cm. This spacing resulted in the green beam's diameter comprising roughly 16.5 camera pixels. The green receiver's FOV, not shown in these spot diagrams, matched the green beam's diameter.

Based on prior experience at the facility, we placed a black tarp on the tank's highly reflective floor. The tarp's purpose was to reduce the dynamic range of returned powers and to enhance the green beam's visual contrast from its surroundings. Then, a rectangular frame of known size and orientation and with known distance demarcations was placed on the tarp. The frame's purpose was to provide a reference

[1]NOAA/Dewberry provided $100k to fund part of this work.

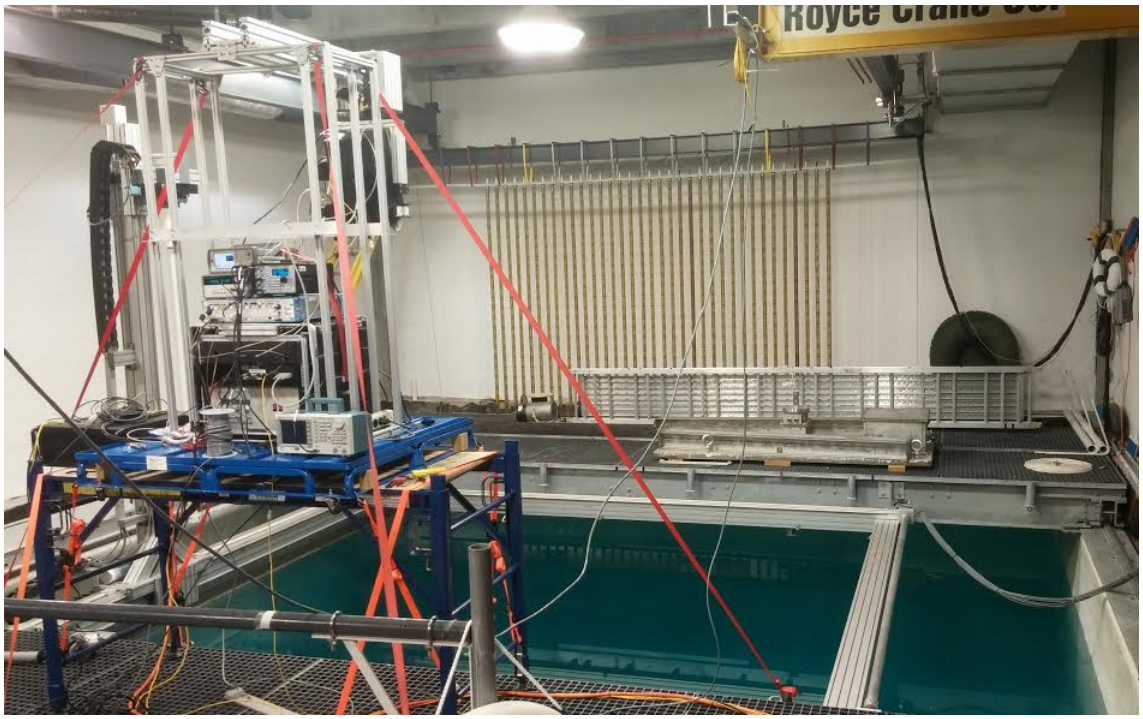

Figure 23: Pathfinder, the world's first hybrid lidar, deployed at the Love Manufacturing Building's water tank facility in March 2015.

for the green beam's movement on the floor. A witness camera, installed underwater with known position, was aligned to view the framed area such that the frame's bottom edge was parallel to the image's bottom edge. Figure 25 shows an image captured by the witness camera. In this 1280x1024 grayscale image, the green beam is the bright, white spot centered on the tarp. During wavy conditions, the green beam's position changed but always stayed within the frame's borders. Images like these were used to determine the green beam's truth coordinates on the tank floor.

After the positions of Pathfinder, the witness camera, and the frame were chosen, a global coordinate system using forward-starboard-down positive axes was established. The coordinate system's origin was arbitrarily chosen as a point on an I-beam above the water surface. Measurements from this position to the Pathfinder lidar, to the witness camera, and to the frame's front left corner determined each object's Northing, Easting, and Down (NED) offset. Importantly, these NED offsets served as coordinates in a common LGF coordinate system. Therefore, NED coordinates

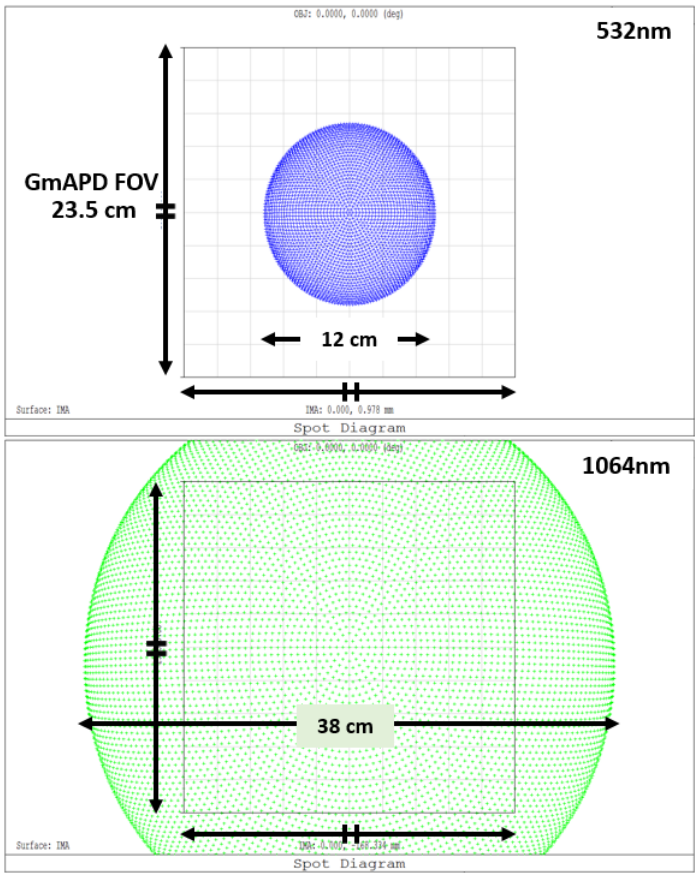

Figure 24: Pathfinder's green and IR beams co-located at its configured imaging distance. The green beam, shown as the blue circle, is smaller than the GmAPD's FOV (the square); the IR beam, shown as the green circle, is larger than the GmAPD's FOV.

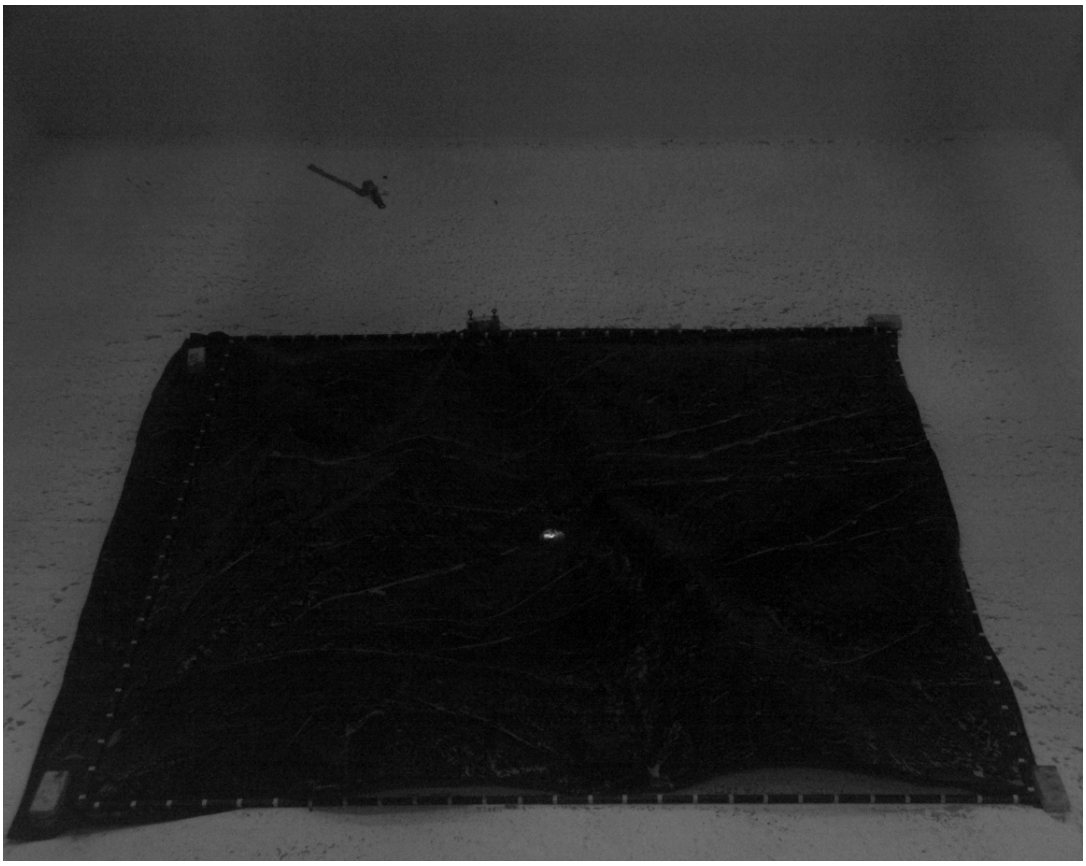

Figure 25: A witness camera installed underwater viewed the green beam's movement within a frame of known size on the tank floor.

computed by Pathfinder using Equation 9 could be compared to the beam's truth coordinates determined from witness camera images. Truth coordinates were determined by converting the beam's pixel location in witness camera images to NED coordinates via perspective transformation, shown in Equation 60 as

$$\begin{bmatrix} N_P \\ E_P \\ D_P \end{bmatrix} = \begin{bmatrix} v_0 + v_1(row) \\ h_0 + h_1(col) \\ D_{frame} \end{bmatrix}, \tag{60}$$

where:

v_0 and v_1 are vertical interpolation parameters,
h_0 and h_1 are horizontal interpolation parameters, and
D_{grid} is the measured Down offset to the frame's front-left corner.

Equation 60 describes the transformation of pixel coordinate [row,column] to NED coordinate [N,E,D].[2] This transformation may only be applied to image pixels within the frame and relies on the following conditions:

(1) the frame's bottom edge is parallel to the image's bottom edge;

(2) the camera's NED position is known;

(3) the spacing between the frame's demarcations is known; and,

(4) the NED coordinates of the frame's four corners and their corresponding positions in the image are known.

The first condition was satisfied when aligning the camera. The second condition was satisfied when measuring the camera's NED offset from the LGF-coordinate system's origin. The third condition was satisfied when designing and building the frame. The

[2]Although the expressions for N_P and E_P are expressed as linear functions of *row* and *column*, this is only for brevity. Their full analytic expressions are much more complex and Appendix C contains details of their derivations.

fourth condition was satisfied after measuring the front-left-corner's NED offset from the origin and imaging the scene. Since the frame's size and orientation were known and since the tank floor was flat, coordinates corresponding to the other three corners could be determined relative to the front-left-corner. Image pixels corresponding to the frame's corners were determined manually in Matlab using Figure 25.

Waves were created using the apparatus shown in Figure 26. Known as the "wave generator", this steel container was partially filled with water and suspended from an overhead gantry using a pulley system. It weighed nearly 800 pounds and required one or two individuals to operate. By pulling a rope attached to the pulley, individuals could disturb the water by plunging the wave generator into and out of the water. After multiple plunges, long-wavelength waves affecting the entire tank were created. These waves had peak-to-trough amplitudes ranging from 10-20 cm. Sometimes, wave interference introduced high frequency structures on the surface, but most wave content was low frequency (relative to the pulse's footprint). Wave creation was unsystematic; it depended on the individuals' effort and strength and the frequency of plunging, neither of which were reproducible. Nonetheless, this method was adequate in creating waves that altered the green beam's refracted trajectory, producing discernible position changes on the tank floor.

Performing experiments and collecting data involved operating custom software (hereafter called "Bathy-m") written to control Pathfinder and the witness camera. Bathy-m handled timing synchronization between Pathfinder's linear-mode and Geiger-mode lidars and between Pathfinder and the witness camera. This synchronization was achieved by controlling a function generator that sent trigger signals to each device referenced to a common high-frequency clock. Bathy-m also managed acquiring, processing, and writing data during the experiments. Raw binary-data files and Hierarchical Data Format (HDF) files were written to the hard drive, containing all relevant data from the experiment. Once waves were created and started steering

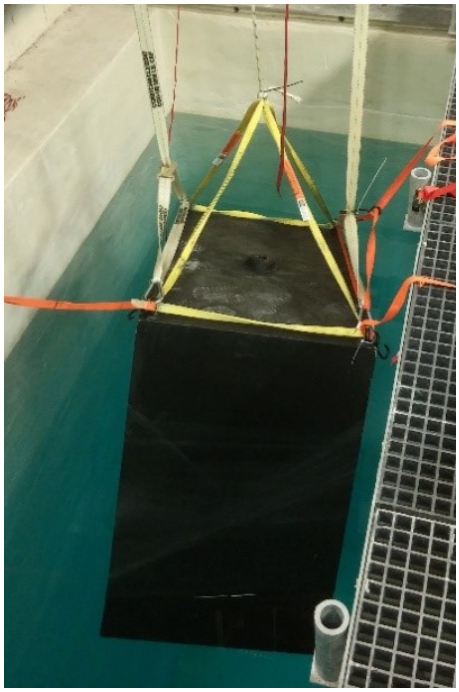

Figure 26: This 800-pound container served as the wave generator. When repeatedly plunged into and out of the water, it created waves that altered the green beam's refracted trajectory and position on the tank floor.

the beam, the software's operator began data acquisition. Experiments were designed to last 10 seconds. After 10 seconds, data collection ceased, and all data acquired during that interval was written to output files. Each experiment had a unique, HDF output file, containing all GmAPD data, waveform-resolved data, and witness-camera data. Raw data, consisting of diagnostic information from the waveform-resolved system's digitizer, was not written to a unique file for each experiment. Instead, raw data was appended to one file containing binary diagnostic data from all previous experiments. Table 1 shows each device's data collection rate, its fundamental data output, and the amount of data written for one experiment. 134 experiments recording these outputs were performed during flat and wavy conditions. All other data, including floor coordinates and interface DSMs, were derived from this fundamental data.

Unfortunately, after performing many of the experiments, most were found to be

Table 1: Each device's data collection frequency, fundamental output, and the amount of output written for one 10-second experiment.

Device	**Data Rate**	**Output(s)**	**Number Written**
Linear-mode lidar	2 kHz	1024-sample waveform	20000
Geiger-mode lidar	2 kHz	32-x-32 TOF values	20000
Witness Camera	30 Hz	1280-x-1024 image	300

unusable. The first 100 were corrupted by a wave measurement structure of buoys placed near the green footprint on the water surface. This square structure was over 30-cm wide, larger than both the green footprint and the GmAPD camera's FOV. Its intended purpose was to provide truth data for the surface's low-frequency orientation. However, because the structure was within the IR-illuminated area of the water surface, photons reflecting off the structure at oblique angles were detected by the GmAPD camera even though it was not within the camera's FOV. Consequently, GmAPD measurements could not reconstruct the water surface because the majority of detected photons originated from the structure. The final 34 experiments occurred after removing the wave measurement structure. For these experiments, the GmAPD data was deemed acceptable. Pathfinder was subsequently disassembled, packed up, and returned to EOSL. However, upon return, it was discovered that the digitizer's diagnostic information did not record properly for all 34 experiments. This problem was not noticed during the data collection experiments because it had never occurred at any point during the previous two years of operating the digitizer. Thus, validating the digitizer's raw data during experimentation only entailed checking that the proper number of bytes were written. Even though the number of bytes written to the ever-growing binary file was reviewed, the data was never cross-validated with the HDF data while the equipment was installed at the water tank. While two of the digitizer's diagnostic entries (l_A and l_W) were recorded for coordinate computation purposes in the HDF files, data critical to timing synchronization was not. This

problem affected 30 of the remaining 34 experiments. For these experiments, sub-ns synchronization of the Geiger-mode and linear-mode was subsequently unachievable when post-processing the data, prohibiting accurate surface reconstruction. Therefore, these files were also deemed unusable, leaving only four viable data files for use in this thesis.

Despite having only four of the original 134 experiments available to analyze, the data associated with these four files is completely representative of the conditions created at the water tank. One file was recorded during flat water conditions and the other three were recorded during wavy water conditions. Therefore, I believe the results presented in this chapter are a fair representation of the results the other experiments would have produced had their output files not been corrupted. The next section provides background of the evaluation framework created to process the data contained within these four files. The three following sections provide the corresponding results as they pertain to geometric reconstruction of seafloor coordinates (Section 4.3), radiometric restoration of seafloor reflectance (Section 4.4), and unified reconstruction and restoration of seafloor images (Section 4.5).

4.2 Data Evaluation Framework

A suite of Matlab functions and scripts were written to process Pathfinder's collected data. The purpose of these tools was to parse the experiments' fundamental outputs (Table 1) and to group them into subsets. Each subset is called an acquisition and may be viewed as the evaluation unit in this framework. Each acquisition has synchronized waveform, GmAPD, and witness-camera data that serve as its inputs. An acquisition's outputs are predicted floor coordinates (modeling different scenarios) and a truth coordinate. Figure 27 shows an experiment divided into N fixed-size acquisitions.

Each acquisition's size was set as 100 ms of continuous data, establishing 100

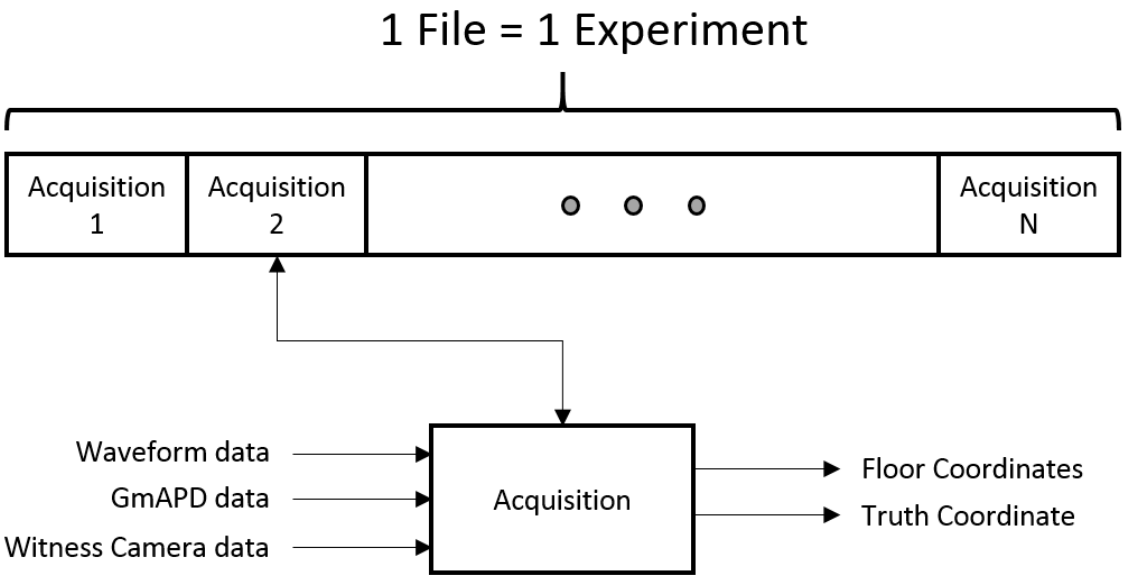

Figure 27: Each 10-second experiment is separated into 100-ms subsets called acquisitions. Acquisitions serve as the fundamental unit of comparison in the data evaluation framework.

acquisitions per file. This value of time was selected to equal a wave's "epoch". A wave epoch is used as a simplifying assumption to establish how long the GmAPD camera can treat measurements from the scene as originating from the same low-frequency wave. An epoch spanning multiple laser pulses is necessary to reduce Geiger-mode noise. As mentioned in Section 3.2, Geiger-mode ranging variance to the water surface was large. To reduce this variance, interface modeling techniques used histogram-trimming and an accumulator array. The wave epoch directly affects the number of measurements allowed in the accumulator array. Based on witness camera imagery captured during wavy conditions, the epoch was chosen as 100 ms, because over this period, the beam maintained its floor position well. Consequently, a maximum of 100 ms of GmAPD data may be aggregated into the accumulator array when creating one DSM.

Establishing 100-ms acquisitions determines the number of waveforms, GmAPD camera images, and witness camera images used as acquisition inputs. Based on the measurement rates in Table 1, these values were 200 waveforms, 200 GmAPD

images, and 3 witness camera images, respectively. Since each acquisition produces only one truth coordinate and one floor coordinate per algorithm, the following procedure was implemented to map these inputs to one set of values usable in coordinate computation:

(1) Compute one l_A and l_W value per waveform. Then, average the 200 l_A values and average the 200 l_W values to produce $\overline{l_A}$ and $\overline{l_W}$. These averaged values may serve as floor-coordinate computation inputs.

(2) Compute coordinates for each 32x32 GmAPD image and aggregate into accumulator array. Compute one DSM from the accumulator array coordinates. This DSM may be used for SST-compensated, coordinate-computation algorithms.

(3) Compute truth coordinates ($[N_{truth}, E_{truth}, D_{truth}]^T$) for each witness camera image. Average the resulting coordinates to produce the truth floor coordinate.

Figure 28 graphically depicts the procedure, showing how acquisition inputs may be mapped to outputs. This schematic shows Equation 1 and Equation 9 producing naïve coordinates and algorithm coordinates, respectively. These names are meant to describe the scenarios each equation models. Equation 1 models the naïve scenario wherein SST is ignored: only Pathfinder's waveform-resolved data is used to produce floor coordinates, which contain interface-induced errors. Equation 9 models the scenario wherein SST is measured and the angles ϕ_w and ω_w are estimated. Here, Pathfinder's waveform-resolved data is combined with its Geiger-mode data using the algorithms described in Chapter 3 to robustly account for the irregular water surface when computing the coordinates. By comparing naïve and algorithm coordinates to the truth coordinate, differences in measurement error between the two modeled scenarios may be analyzed.

Several other aspects of Figure 28 merit explanation. "Constant inputs", pointing to Equation 1 and to Equation 9, are all the parameters necessary to compute floor

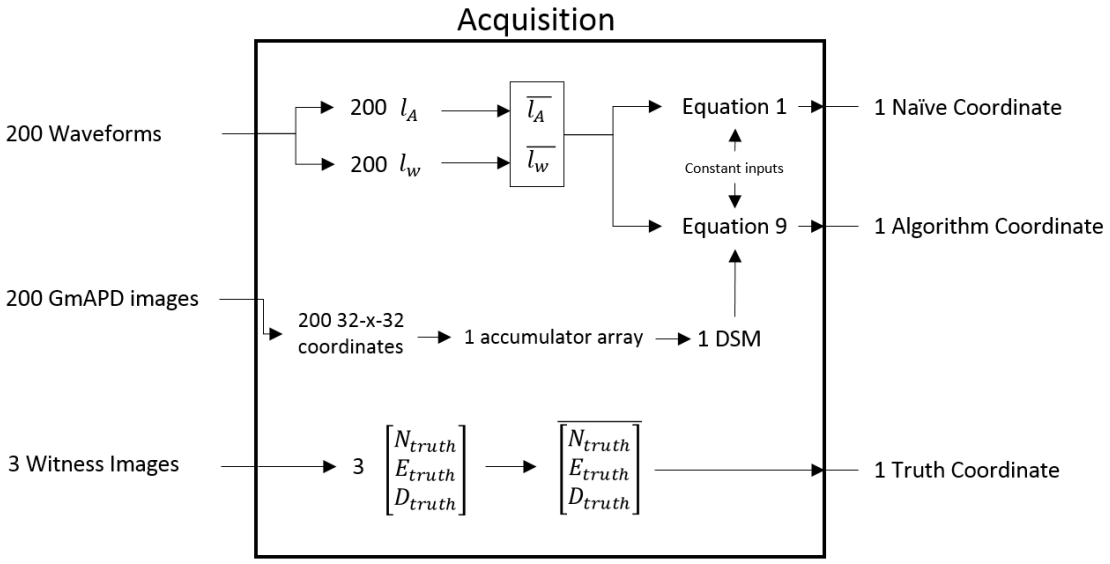

Figure 28: Acquisition inputs are mapped to its outputs.

coordinates that remain constant across all experiments and the acquisitions within them. These parameters are also common to both equations. Constant parameters that were non-zero are listed in Table 2.

Table 2: Constant, non-zero parameter values for all experiments.

Parameter	**Value**
N_T	-4.019 m
E_T	-0.0983 m
D_T	-2.309 m
ϕ_A	20°

Figure 28 also shows that the 200 32x32 GmAPD coordinates are mapped into an accumulator array. Section 3.2 contains the details of how an accumulator array works. Here, I use that process with array resolutions of 2x2, 3x3, 4x4, 5x5 and 6x6. Each of these resolutions produces a unique DSM that may be used when computing floor coordinates. Results for each of these resolutions is presented in the next section. An array dimension of 6x6 is the maximum considered resolution because for a deployed system employing circular scanning, surface point analysis revealed

that resolutions higher than 6x6 do not result in multiple GmAPD measurements falling within each accumulator-array-pixel's boundaries. Appendix D shows a table of expected GmAPD measurements falling within pixel boundaries for each of these resolutions in an airborne deployed scenario.

The final aspect of Figure 28 warranting explanation is how the DSM may be used to estimate ϕ_w and ω_w when using Equation 9. For a given accumulator array resolution, a fixed number of spatially averaged coordinates will be produced (i.e. 4, 9, 16, 25, or 36). From these coordinates, normal vectors may be computed to estimate SST. The original goal was to compute many surface normal vectors for a DSM and to ray trace through the DSM when determining the refracted beam's trajectory. However, the noise of GmAPD measurements ($\approx$ 4 cm) together with the small green footprint ($\approx$ 12 cm) caused sub-footprint normal vectors to be highly sensitive to ranging errors. In turn, this caused ray tracing through a DSM with sub-footprint normal vectors to be unreliable. Recognizing this, a simplifying restraint was introduced such that a plane-of-best-fit was regressed through all accumulator array coordinates. This reduced the normal vector's sensitivity to ranging errors, resulting in more reliable ray tracing through the DSM. Therefore, only one surface normal, corresponding to the plane-of-best-fit, is produced per DSM. This surface normal may then be used in Equation 23 to compute $\vec{r}$, from which ϕ_w and ω_w may be determined using Equation 50 and Equation 51.

Each file contains 100 unique sets of data using this evaluation framework. Each one of these sets corresponds to an acquisition within the file. Acquisition outputs are the three sets of coordinates: naïve, algorithm, and truth; which may be compared and analyzed. The next section presents results analyzed by acquisition for each of the four files. For convenience, all subsequent analysis refers to the one file recorded during flat water conditions as "flat conditions" and to the three files recorded during wavy water conditions as File 1, File 2, and File 3.

4.3 Geometric Results

During flat conditions, the water surface was a flat, planar surface with Down coordinate of 0.819 m. Figure 29 shows Pathfinder's reconstruction of the surface over time. The two plots in Figure 29 correspond to data independently acquired with Pathfinder's two lidars. The waveform-resolved-system's data is shown in blue, and the Geiger-mode-system's data is shown in red. These plots were generated with no sharing of data across systems (i.e. no hybrid algorithms were employed). For the waveform-resolved system, the water surface level was determined for a given acquisition by using its surface coordinate's Down value. For the Geiger-mode system, the water surface level was determined for a given acquisition by computing the average Down value of coordinates used to construct its DSM. These two procedures may then be performed for each acquisition. Since acquisitions occur sequentially in time, the effect of sequentially plotting each acquisition's water surface level produces the plots shown. Both systems observe the water surface as constant, with minor deviations caused by in-air ranging variance. Both systems also exhibit a 2-cm bias, most likely caused by incorrectly measuring Pathfinder's NED offset from the global origin.

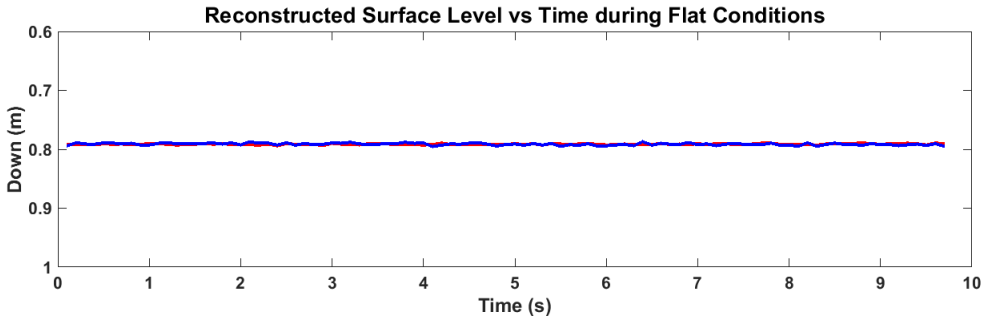

Figure 29: Pathfinder's two lidars reconstruct the water surface level versus time during flat conditions. Waveform-resolved data is the blue plot; Geiger-mode data is the red plot.

The green beam's footprint was stationary on the floor during flat conditions (see Figure 25). The NED truth coordinate, computed by applying Equation 60 to the beam's pixel position in the witness image, was $(-1.1687m, -0.0510m, 7.052m)$.

Table 3 contains aggregated results of using various methods to compute floor coordinates during these conditions. The table's first column indicates the method used. Naïve refers to coordinate computation using Equation 1; "i-x-i DSM, OLS" refers to coordinate computation using Equation 9 with OLS surface-normal estimation from an i-x-i-resolution DSM; and, "i-x-i DSM, PCA" refers to coordinate computation using Equation 9 with PCA surface-normal estimation from an i-x-i-resolution DSM. The second column contains each method's average geometric error, computed by first determining the magnitude of difference between the predicted coordinate and the truth coordinate for each acquisition and then averaging across all acquisitions. Methods are sorted by this column in ascending order. The third column contains each method's average SAS_{99}, computed using the method depicted in Figure 21 for each acquisition and then averaging across all acquisitions. I have found no examples in the literature describing an analytical solution for propagation of accumulator array measurement errors in the PCA-approach for estimation of surface normals. Therefore, estimation of variances on these parameters remains a subject for future work, and these table entries have been left blank.

As expected, the naïve method performs best during flat conditions. It has the smallest average error and uncertainty (SAS_{99}) of all methods because it perfectly reconstructs the surface for each acquisition. This result is a direct consequence of its flat-water assumption. During flat conditions, $\sigma^2_{\phi_w}$ and $\sigma^2_{\omega_w}$ are 0 for the naïve method, meaning its floor coordinates have no error or uncertainty arising from surface measurements. Therefore, in-air and in-water ranging variances are the only causes of floor coordinate error. On the other hand, hybrid methods have non-zero $\sigma^2_{\phi_w}$ and $\sigma^2_{\omega_w}$, meaning that their errors and uncertainties should be larger than the naïve case because ranging performance is constant across all methods. This is exactly what is observed. However, hybrid performance is still good, as typical errors are approximately 3 cm. In these cases, the errors and uncertainties exceeding naïve

Table 3: Coordinate computation errors and uncertainty during flat conditions.

Method	$\overline{\lvert Error \rvert}$ **(m)**	$\overline{SAS_{99}}$ **(m)**
Naïve	0.010	0.3848
3x3 DSM, PCA	0.0246	–
3x3 DSM, OLS	0.0262	0.4581
4x4 DSM, PCA	0.0278	–
6x6 DSM, PCA	0.0282	–
2x2 DSM, OLS	0.0285	0.4682
5x5 DSM, PCA	0.0303	–
4x4 DSM, OLS	0.0311	0.4718
2x2 DSM, PCA	0.0359	–
5x5 DSM, OLS	0.0493	0.4849
6x6 DSM, OLS	0.0743	0.4795

values may be viewed as those introduced by using a hybrid lidar approach instead of assuming a flat surface when the water was, indeed, perfectly flat. It is only in this rare scenario that the measurement variances and result of the error propagation degrade the accuracy of coordinates as compared to the naïve case. In general, PCA-based methods and 3x3 DSM resolutions introduce smaller errors than OLS-based methods and other resolutions. A likely explanation for these trends is that their normal vector estimates are less sensitive to measurement errors. For PCA, less sensitive normals can be explained by rejecting coordinate outliers better than OLS. For 3x3 DSM resolution, less sensitive normals can be explained by this resolution being an optimal combination of coordinate noise and redundancy when estimating the normal. Uncertainty generally increases as error increases. The trend is monotonic except for the "6x6 DSM, OLS" case. Appendix E contains figures showing example DSMs constructed during flat conditions.

During wavy conditions, low-frequency waves with peak-to-trough amplitudes of 10-20 cm caused the water level to rise and fall. Figure 30, Figure 31, and Figure 32 show Pathfinder's ability to reconstruct the surface's changing water level versus time for File 1, File 2, and File 3, respectively. These plots were generated using the same method that produced Figure 29. Once again, the blue curves correspond to waveform-resolved data and the red curves correspond to Geiger-mode data. As seen in all three figures, both lidars are synchronized in time and detect the same changes in water level. In general, the Geiger-mode lidar is noisier, exaggerating the change in some waves' water level. The maximum overshoot is approximately 5 cm. No truth data exists for the water-surface level because the wave measurement structure was removed before performing these experiments. However, as discussed at the end of this section, analyzing Pathfinder's floor-coordinate measurement errors when compensating for SST indicates the reconstructed surface level was very good.

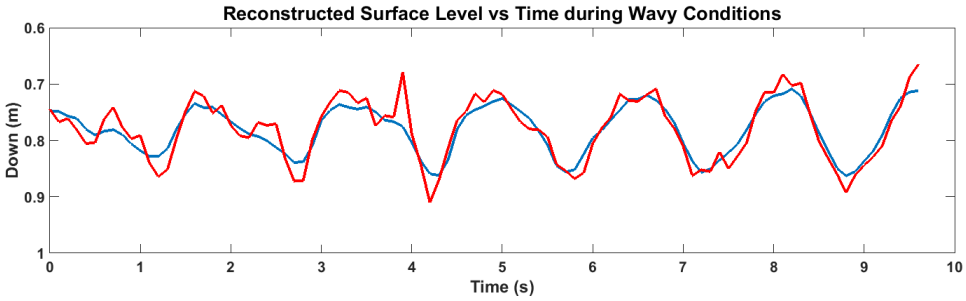

Figure 30: Pathfinder's two lidars reconstruct the changing water surface level versus time for File 1 waves. Waveform-resolved data is the blue plot; Geiger-mode data is the red plot.

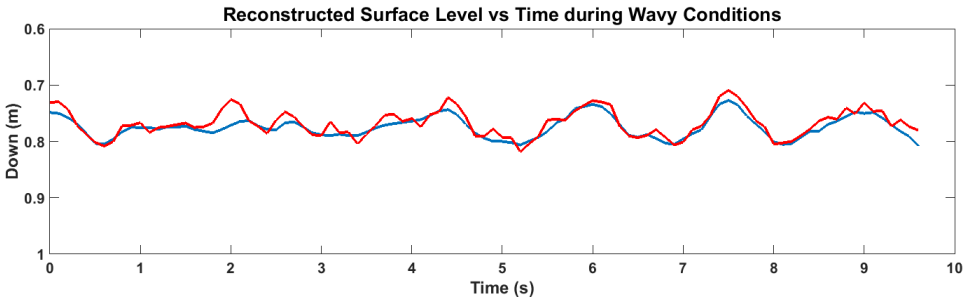

Figure 31: Pathfinder's two lidars reconstruct the changing water surface level versus time for File 2 waves. Waveform-resolved data is the blue plot; Geiger-mode data is the red plot.

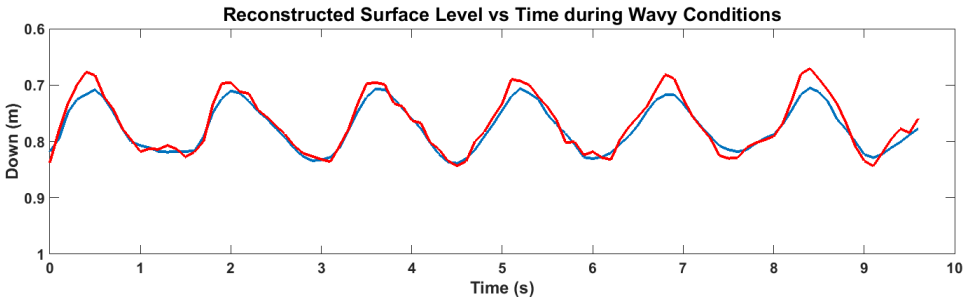

Figure 32: Pathfinder's two lidars reconstruct the changing water surface level versus time for File 3 waves. Waveform-resolved data is the blue plot; Geiger-mode data is the red plot.

As discussed in Chapter 3, a novel, coincidence processing technique was employed to reduce Geiger-mode lidar noise. This involved histogram trimming of GmAPD TOF data on a per-pixel basis by using the waveform resolved system's in-air ranging measurements (see Section 3.2). Figure 33, Figure 34, and Figure 35 show Pathfinder's ability to reconstruct the surface's changing water level versus time when employing hybrid processing algorithms for File 1, File 2, and File 3, respectively. Here, the blue curves are the same as they are in Figures 30, 31, and 32, but the red curves are different. While the red curves are computed the same way, each acquisition's DSM-coordinate noise has been significantly reduced from histogram-trimming. Coordinates comprising the DSMs are less noisy here than before because the Geiger-mode-lidar's TOF variance is smaller (Chapter 3 contains the before- and after-histogram-trimming TOF variance values). Appendix F contains figures showing example DSMs constructed from hybrid processing techniques during these wavy conditions. These are the DSMs from which surface normals are estimated in subsequent analyses.

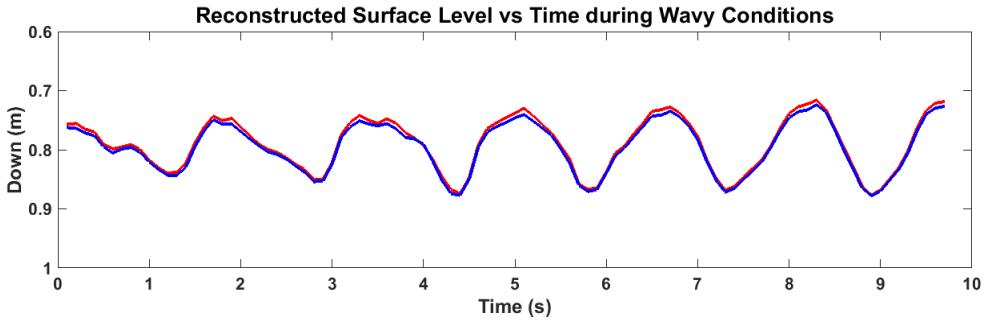

Figure 33: Pathfinder's two lidars reconstruct the changing water surface level versus time for File 1 waves. Waveform-resolved data is the blue plot; Geiger-mode data is the red plot.

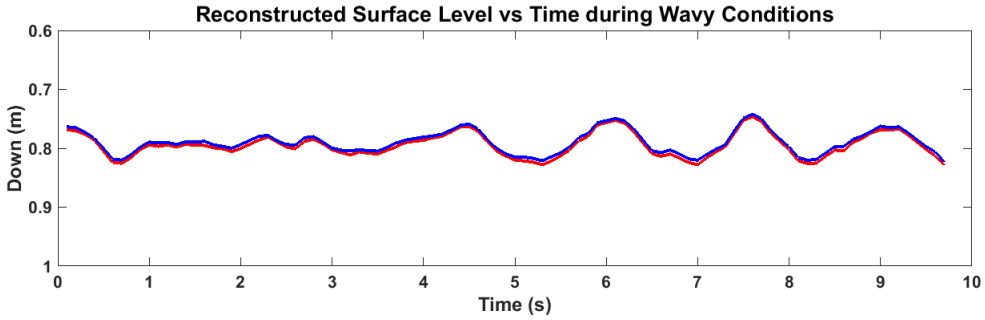

Figure 34: Pathfinder's two lidars reconstruct the changing water surface level versus time for File 2 waves. Waveform-resolved data is the blue plot; Geiger-mode data is the red plot.

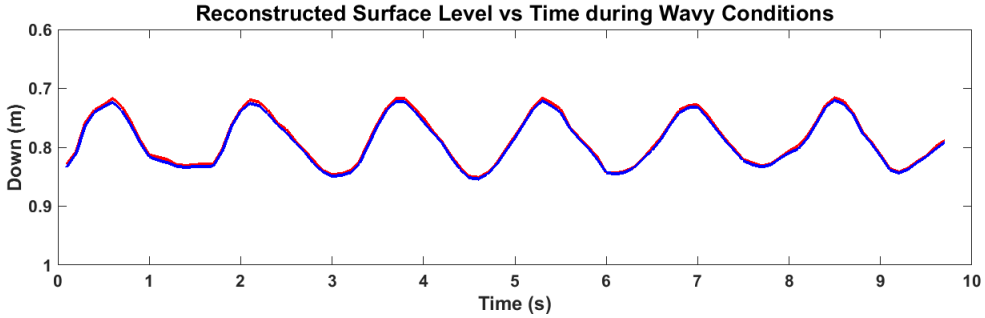

Figure 35: Pathfinder's two lidars reconstruct the changing water surface level versus time for File 3 waves. Waveform-resolved data is the blue plot; Geiger-mode data is the red plot.

The green beam's footprint wandered within the frame on the tank floor during these conditions. Figure 36 shows a time lapse of witness camera images recorded in File 1. Here, the beam's shape remains fairly constant, but its position changes. This is indicative of low-frequency tilts steering the beam, as discussed in Chapter 3. Importantly, the position changes in all directions, instead of along the pointing

vector (up and down in these images – i.e. the red, dotted line). This corroborates the need for SST-compensation algorithms that accommodate arbitrary beam steering. For these conditions, naïve coordinates computed by Equation 1 will have interface-induced error arising from uncompensated SST. Because the refracted beam's computed trajectory is always the same when using Equation 1, waves causing beam steering will produce l_W values that project the floor coordinate deeper or shallower than the true tank floor. The resulting errors should be larger than those when compensating for SST and computing floor coordinates with Equation 9. Figure 37 illustrates this point by plotting one acquisition's predicted and true floor coordinates in Matlab. The coordinates here are shown from a top-down view of the tank floor. The black circle is the naïve coordinate; the blue circle is an SST-compensation-algorithm coordinate; and, the green circle is the true floor coordinate. The red "X" is the hypothetical position of the beam during flat conditions. Clearly, the SST-compensation algorithm significantly reduces the error because the naïve coordinate cannot predict floor coordinates anywhere else but above and below the red "X". It is important to note, however, that error is three dimensional, as opposed to the two dimensions shown here. This figure is simply meant to show that SST-compensation algorithms reduce floor error by improving the refracted beam's trajectory.

Table 4, Table 5, and Table 6 contain aggregated results of applying the same methods used in Table 3 to wavy conditions. These tables correspond to waves recorded during File 1, File 2, and File 3, respectively, and were produced using the same method that produced Table 3, with one subtle exception. While the $\overline{|Error|}$ column is still computed the same way, it is important to note that the truth coordinate now changes for every acquisition, instead of being constant like it is in flat conditions. Tables are once again sorted by ascending order of entries in column 2. For all three files, using SST-compensation algorithms reduces the magnitude of coordinate error. Usually, error reduction is around 40%. Moreover, $\overline{SAS_{99}}$ is smaller for

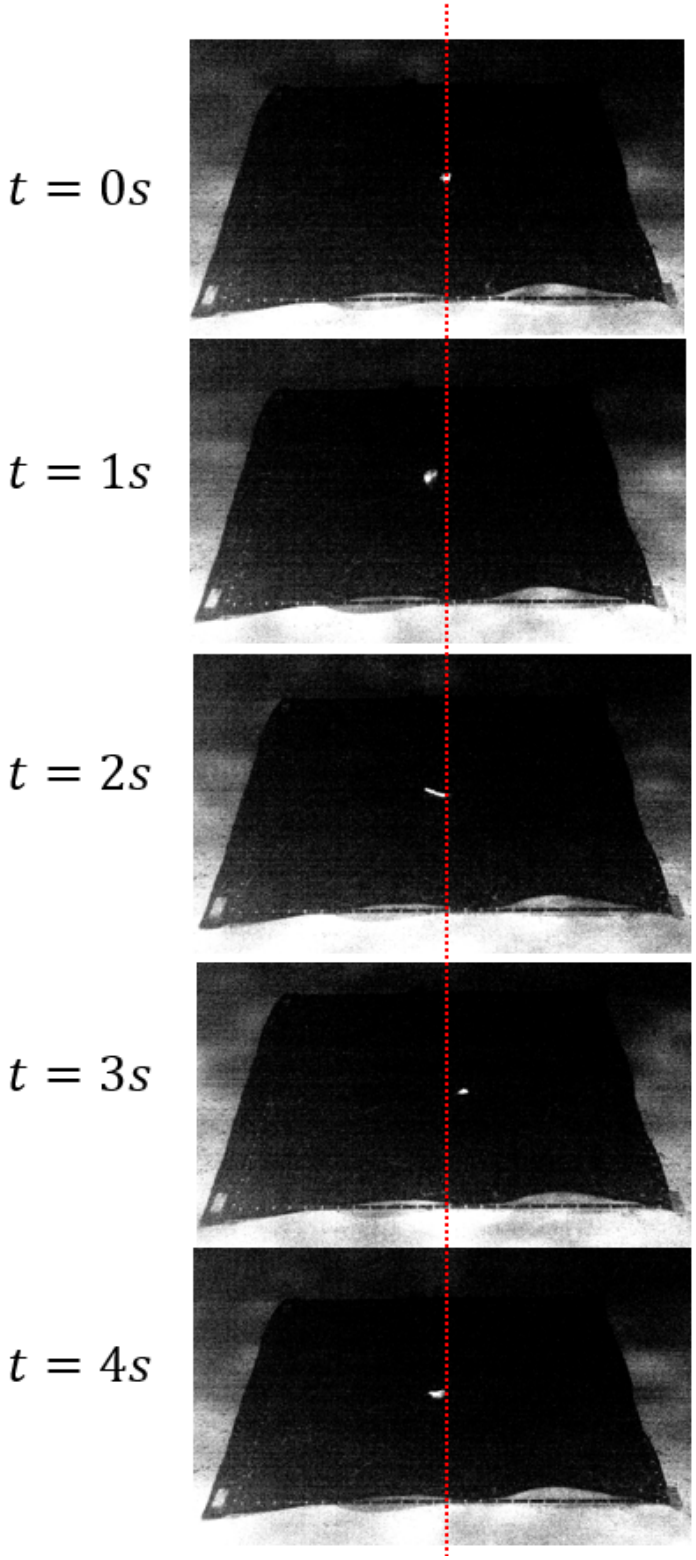

Figure 36: A time-lapse showing the effects of beam steering from waves on the water surface.

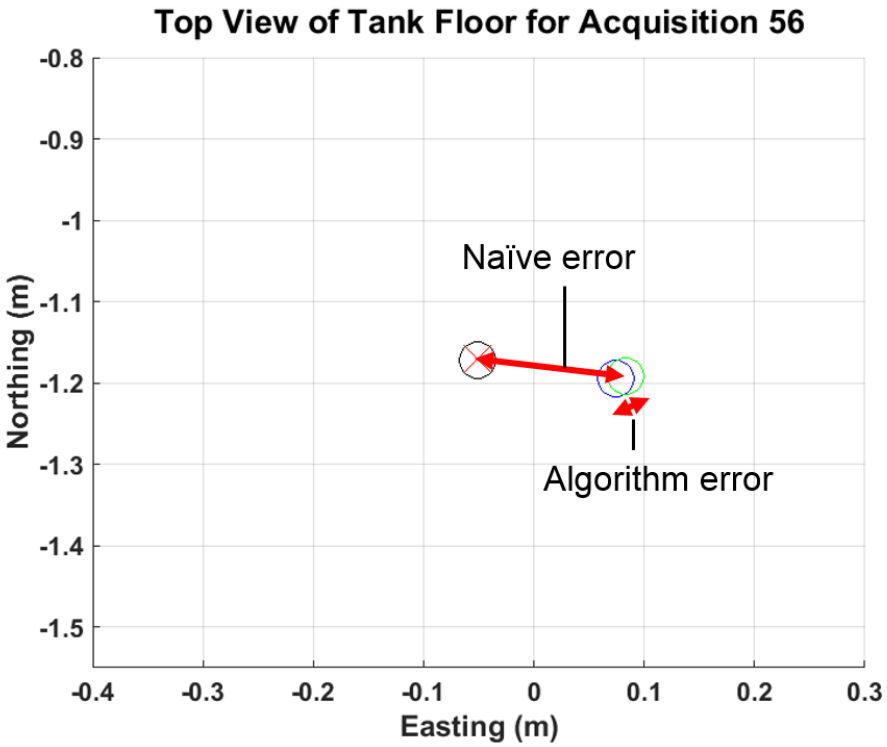

Figure 37: Coordinate computed by SST-compensation algorithm reduces floor coordinate error.

these algorithms when compared to the naïve cases, indicating less uncertainty of the floor measurement. This is because $\sigma^2_{\phi_w}$ and $\sigma^2_{\omega_w}$ are no longer 0 for the naïve case. Instead, they are equal to the *a posteriori* variance of ϕ_w and ω_w during each file's wavy conditions. Because these variances are now larger than SST-compensation algorithm variances, naïve coordinate uncertainty is larger than algorithms' coordinate uncertainty. The combination of these two results, smaller coordinate error and smaller coordinate uncertainty, is what was predicted in Chapter 3 (see Figure 21). Regarding surface normal estimation and DSM resolution, PCA-based methods and smaller resolutions generally outperform OLS-based methods and larger resolutions. The same explanation provided for flat conditions applies here. Because PCA generally outperforms OLS, $\overline{SAS_{99}}$ values for OLS-based methods are probably reasonable upper-bound estimates for PCA-based methods' $\overline{SAS_{99}}$ values.

Table 4: Coordinate computation errors and uncertainty for waves recorded during File 1.

Method	$\overline{\lvert Error \rvert}$ **(cm)**	$\overline{SAS_{99}}$ **(cm)**
Naïve	12.9	52.61
2x2 DSM, OLS	6.91	46.73
3x3 DSM, PCA	6.92	–
4x4 DSM, PCA	6.95	–
6x6 DSM, PCA	6.97	–
5x5 DSM, PCA	7.04	–
2x2 DSM, PCA	7.10	–
3x3 DSM, OLS	7.40	43.63
4x4 DSM, OLS	7.41	43.58
5x5 DSM, OLS	8.15	44.29
6x6 DSM, OLS	9.49	44.34

Table 5: Coordinate computation errors and uncertainty for waves recorded during File 2.

Method	$\overline{\lvert Error \rvert}$ **(cm)**	$\overline{SAS_{99}}$ **(cm)**
Naïve	8.74	46.79
3x3 DSM, PCA	4.45	–
4x4 DSM, PCA	4.63	–
6x6 DSM, PCA	4.70	–
5x5 DSM, PCA	4.73	–
2x2 DSM, OLS	4.97	46.72
2x2 DSM, PCA	5.02	–
3x3 DSM, OLS	5.15	43.58
4x4 DSM, OLS	5.38	43.89
5x5 DSM, OLS	6.92	44.45
6x6 DSM, OLS	7.55	44.43

Table 6: Coordinate computation errors and uncertainty for waves recorded during File 3.

Method	$\overline{\lvert Error \rvert}$ **(cm)**	$\overline{SAS_{99}}$ **(cm)**
Naïve	9.52	48.45
2x2 DSM, OLS	5.11	46.89
2x2 DSM, PCA	5.21	–
4x4 DSM, PCA	5.38	–
3x3 DSM, PCA	5.45	–
5x5 DSM, PCA	5.58	–
6x6 DSM, PCA	5.64	–
4x4 DSM, OLS	5.80	45.03
3x3 DSM, OLS	5.88	44.19
5x5 DSM, OLS	7.07	46.04
6x6 DSM, OLS	7.73	45.98

To help visualize the reduction in coordinate error when using SST-compensation algorithms, Figure 38, Figure 39, and Figure 40 show histograms of the floor coordinate error for File 1, File 2, and File 3, respectively. The SST-compensation method used to produce the algorithm histograms was "6x6 DSM, PCA." Naïve-coordinate error histograms are also shown for comparison in each case. As seen in

these figures, the SST-compensation algorithm reduces the magnitude of floor coordinate error, indicated by histograms shifting to the left relative to the naïve error histograms. Moreover, the shape of the histograms changes as well. Compensation-algorithm error histograms are strongly skewed to the left, indicating active and very good compensation of surface waves most of the time. On the other hand, naïve error histograms tend to be flat and distributed almost uniformly across all error values. This is because they are completely influenced by the waves, whose orientation was completely random.

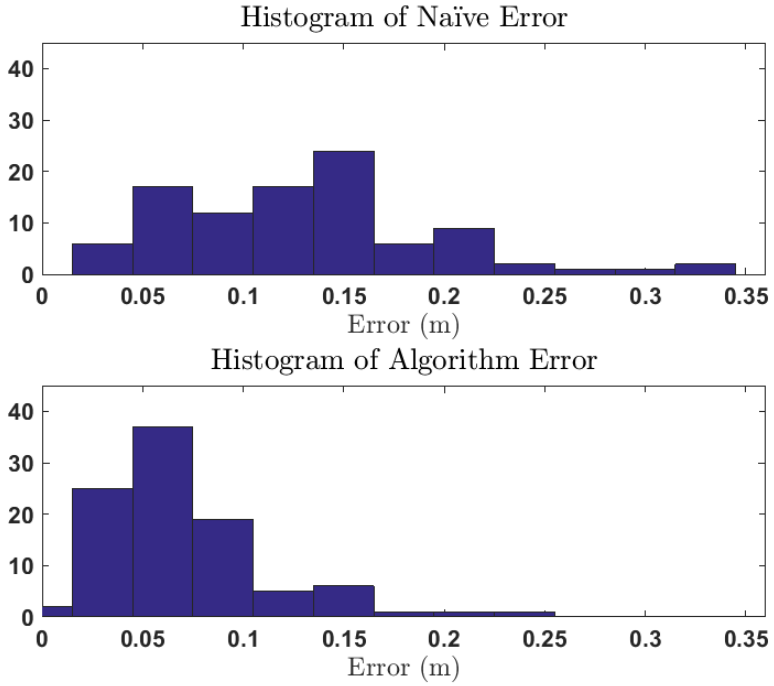

Figure 38: Comparing floor coordinate errors in File 1 for 2 cases: (1) when ignoring SST (naïve); and (2) when using hybrid SST-compensation algorithm (6x6-DSM PCA).

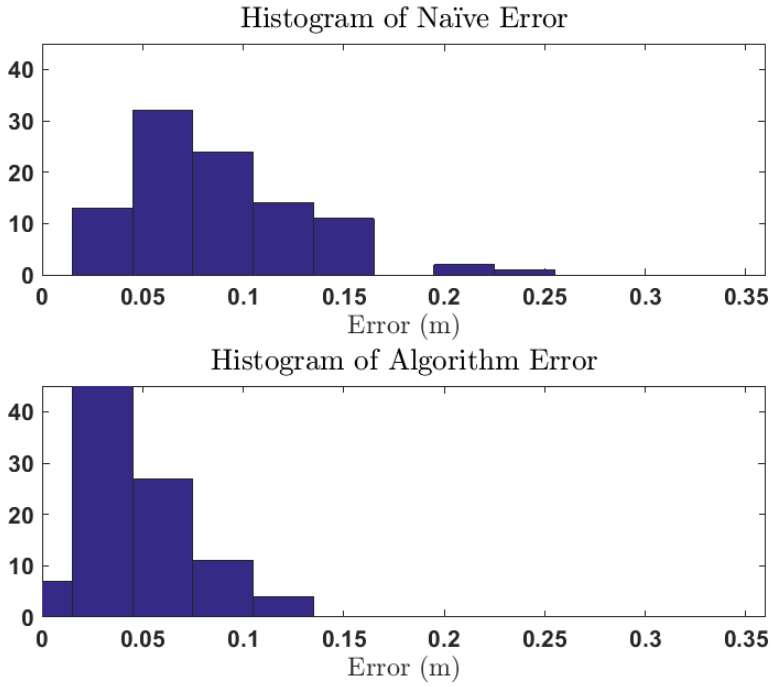

Figure 39: Comparing floor coordinate errors in File 2 for 2 cases: (1) when ignoring SST (naïve); and (2) when using hybrid SST-compensation algorithm (6x6-DSM PCA).

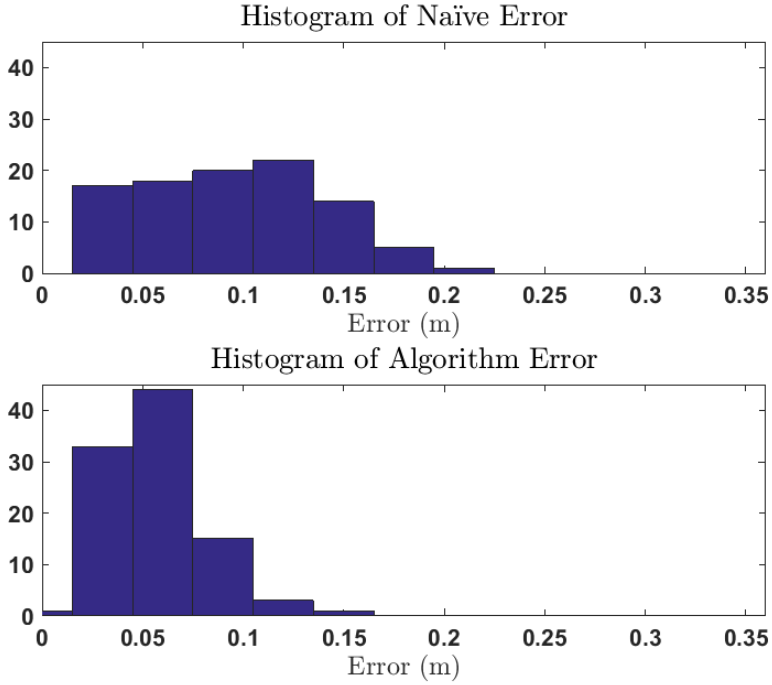

Figure 40: Comparing floor coordinate errors in File 3 for 2 cases: (1) when ignoring SST (naïve); and (2) when using hybrid SST-compensation algorithm (6x6-DSM PCA).

The results presented in this section indicate that a hybrid-lidar approach, wherein a Geiger-mode, IR lidar and a green, linear-mode, waveform-resolved lidar operate co-temporally, is effective in reducing interface-induced coordinate errors. Reductions in floor coordinate errors were a direct result of using SST measurements from Pathfinder's Geiger-mode lidar to estimate the green beam's trajectory when computing waveform-resolved floor coordinates. It is important to note that these results were obtained with 200 lidar pulses during the 0.1-second wave epoch. For currently deployed airborne systems, 200 lidar measurements will not be available for SST compensation. Recognizing this, Figure 41 shows the magnitude of floor coordinate error versus number of pulses used when constructing the DSM. These results apply to waves recorded during File 1. The blue plot represents floor coordinate error using the "6x6 DSM, PCA" method and the red plot is naïve floor-coordinate error. Here, the blue plot decreases with added TOF images because accumulator-array coordinate noise decreases as more GmAPD measurements are averaged, enabling more accurate computation of the surface's normal vector; the red plot remains constant because naïve floor coordinates are independent of GmAPD data. The intersection of these two curves represents the location where neither technique outperforms the other. In these conditions, if system developers design for more than 5-6 overlapping IR measurements of the green surface footprint, then the SST-compensation algorithm will outperform the naïve algorithm. This type of analysis may be used as a heuristic for effective SST compensation in system design. Finally, these results also depend on the low-frequency interface used to histogram-trim the GmAPD measurements. Since Pathfinder had no scanning capabilities, 3 or more non-linear surface measurements from the green system did not exist. To overcome this limitation, surface normals computed from the witness camera were used in histogram trimming. While this introduces a weak connection between truth data and algorithm performance, it is a necessary step for effectively reducing GmAPD noise as described in Section 3.2.

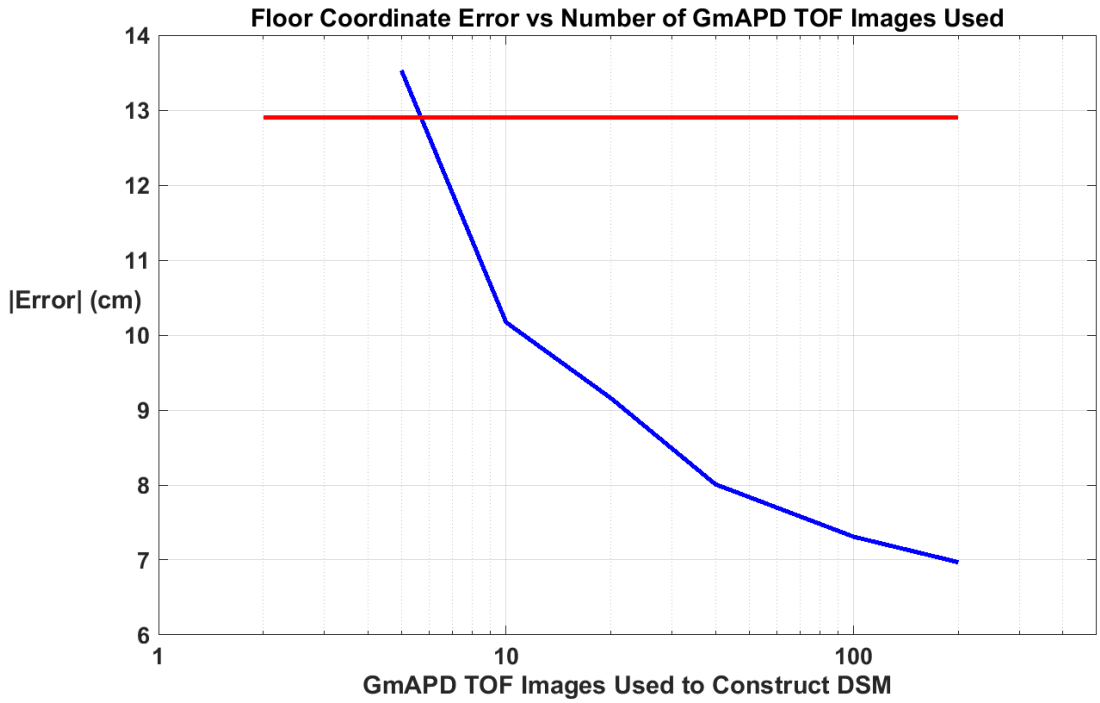

Figure 41: The magnitude of coordinate error decreases as more GmAPD TOF images are used when constructing the DSM. Beyond 5-6 measurements, this SST-compensation algorithm (blue plot) outperforms the naïve algorithm (red plot).

4.4 Radiometric Results

As stated in Section 4.1, reflectance estimation and imaging were not part of the experiments at the water tank facility. Nonetheless, it is still possible to use waveforms collected by Pathfinder during those experiments to identify pulse stretching from non-flat interfaces. Subsequently, simulations can be used to show expected improvements in reflectance estimates based on removing the identified stretching effects.

Identifying interface-induced pulse stretching from Pathfinder's waveforms may be accomplished using the following procedure:

(1) Isolate and analyze the surface return signal of each waveform.

(2) Compute the FWHM of the waveform's surface return signal OR use Equation 41 to estimate the interface's transfer function and compute its temporal extent.

(3) Plot the result of (2) versus the angular difference between the incident vector and the surface normal vector for that waveform (i.e. use Equation 42).

(4) Repeat (2)-(3) for many angular differences.

Step 1 removes contributions from water-column and floor transfer functions, consistent with the theory presented in Section 3.4. Repeating Steps 2 and 3 and plotting their results produces a scatter plot relating the pulse's air-water-interface interaction time to different incidence angles. The scatter of points should show how $t_{interaction}$ (Equation 29) changes as a function of θ (Equation 42). The slope of this change should be the derivative of Equation 29 with respect to θ, shown in Equation 61 as

$$\frac{\partial t_{interaction}}{\partial \theta} = \frac{w_{beam}}{c} \sec^2(\theta). \tag{61}$$

Evaluating Equation 61 with experimental parameters, $w_{beam} = 12$ cm and $\theta = 20°$, produces a value of 7.9 ps/deg. Thus, experimental data should show a 7.9-ps change in surface-return FWHM per 1-degree change in incidence angle. Figure 42, Figure 43, and Figure 44 show the result of performing the procedure above with FWHM used for Step 2.

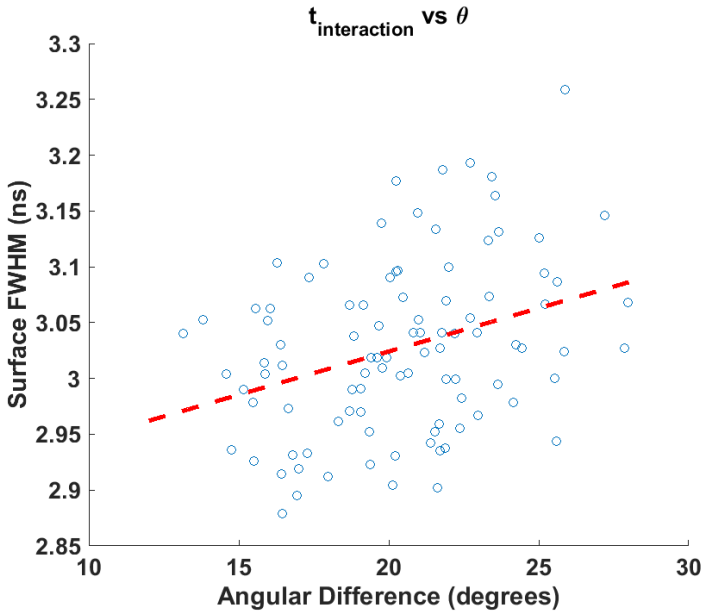

Figure 42: FWHM of surface interaction time versus angular difference for File 1 waves.

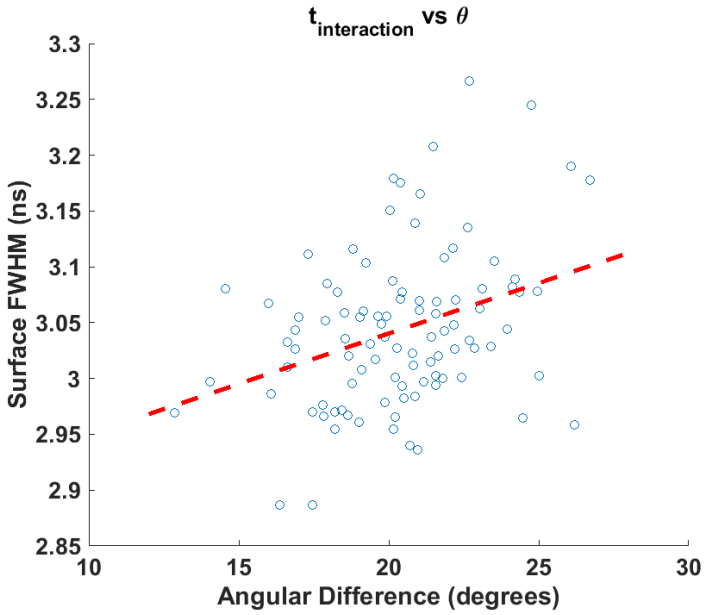

Figure 43: FWHM of surface interaction time versus angular difference for File 2 waves.

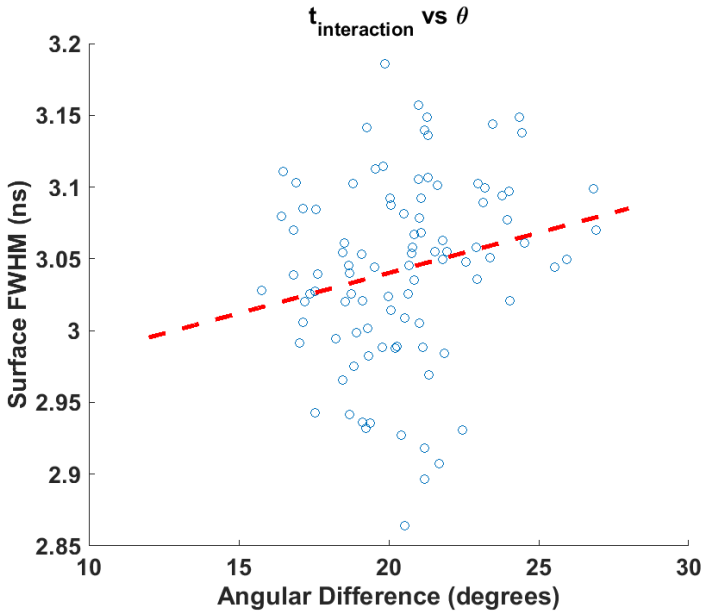

Figure 44: FWHM of surface interaction time versus angular difference for File 3 waves.

Each circle in these plots represents the ($t_{interaction}$,θ)-pair for an acquisition, where: $t_{interaction}$ is the average FWHM of the surface return for the 200 waveforms in an acquisition; and, θ is the angular difference computed by using Equation 42 with the surface normal, n_s, estimated from Pathfinder's constructed DSM for that acquisition. The red, dashed-lines indicate lines-of-best-fit computed with OLS regression. In all figures, $t_{interaction}$ increases as θ increases. The slope of the best-fit lines are 7.8 ps/deg, 9.0 ps/deg, and 5.6 ps/deg for File 1, File 2, and File 3, respectively, all of which agree well with the theorized slope of 7.9 ps/deg.

Because there is significant scatter about the lines-of-best-fit, another characteristic of surface stretching that may be used to identify it is a strong anti-correlation with reflection from the surface. In other words, surface stretching values should decrease as surface reflection increases and they should increase as surface reflection decreases. Here, surface stretching is defined as the FWHM of the surface return signal; and, reflection is defined as a waveform's ratio of peak surface signal received to its peak "t0" signal value. (Recall that the "t0" signal is a lidar's detection of

its transmitted pulse). Figure 45, Figure 46, and Figure 47 show surface reflection and surface stretching vs time for File 1, File 2, and File 3, respectively. In these plots, reflection and stretching have both been normalized to a 0-1 scale for visualization purposes, with 0 corresponding to their minimum values and 1 corresponding to their maximum values. The blue curves are normalized reflection and the red curves are normalized stretching. In all figures, very strong anti-correlated behavior is observed between surface reflection and surface stretching. Therefore, agreement between theorized and observed slopes (Figures 42, 43, and 44) together with strong anti-correlated behavior with surface reflection (Figures 45, 46, and 47) indicate that interface-induced stretching has been identified.

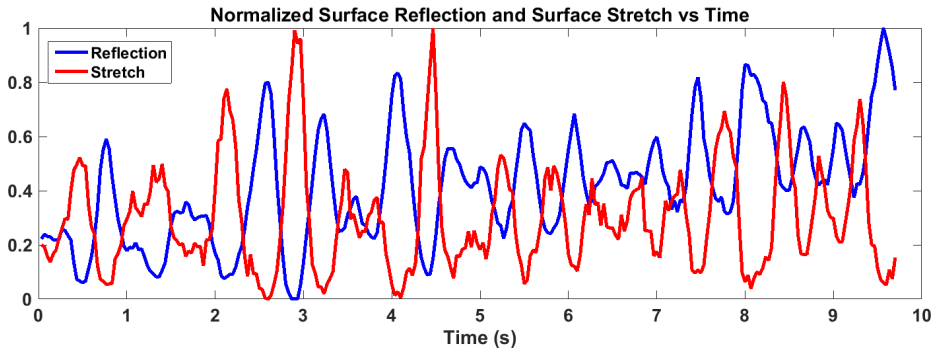

Figure 45: Normalized surface reflection and surface stretch versus time for File 1 waves.

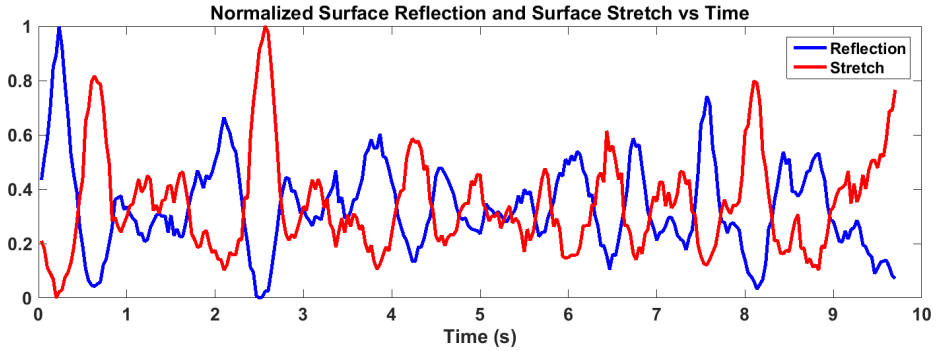

Figure 46: Normalized surface reflection and surface stretch versus time for File 2 waves.

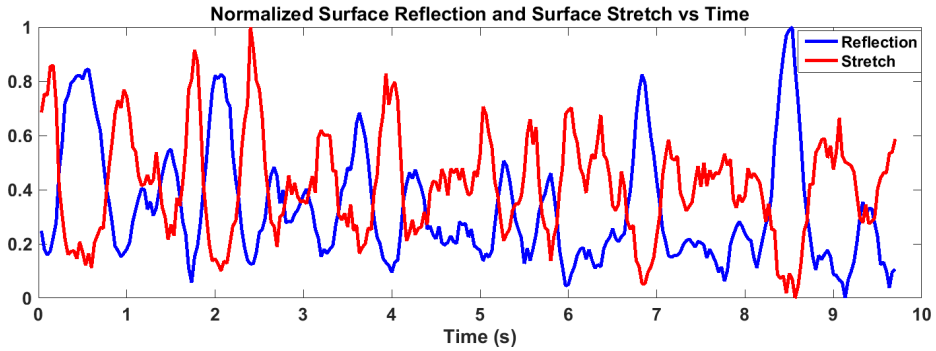

Figure 47: Normalized surface reflection and surface stretch versus time for File 3 waves.

Once surface stretching has been positively identified, the next step is to perform a system identification of the transfer function responsible for introducing this stretch. This identification may be performed by using Equation 41. Figure 48 depicts this process graphically. The first step, labeled as "1" in the figure, involves convolving the wavy-interface return waveform with the flat-interface transfer function. The result of this convolution is the third plot. Next, deconvolve a flat-interface return waveform from the previous result. This step is labeled as "2" in the figure. For this example, deconvolution was performed using a Wiener filter. The result of the deconvolution is the green, dashed waveform in the bottom plot. The blue waveform in that plot is the flat-interface transfer function displayed as a reference. The deconvolved interface transfer function is shifted slightly to the left in time, indicating the water surface was located closer to Pathfinder than when the water surface was flat. Moreover, it has a slightly different shape and magnitude than the flat-interface transfer function, indicating some irregular surface features. However, an important observation of the deconvolved signal's general shape is that it is still very similar to a triangle, indicating that the interface was a low-frequency tilt. By recognizing this earlier in processing (i.e. when constructing the DSM), the entire deconvolution procedure used to identify the transfer function may be avoided and replaced by directly creating a triangle function with width computed by using Equation 30. This second process will hereafter be called "SST-direct". Identified interface transfer functions – whether

by using Equation 41 or "SST-direct" – may then be used to improve estimates of ρ.

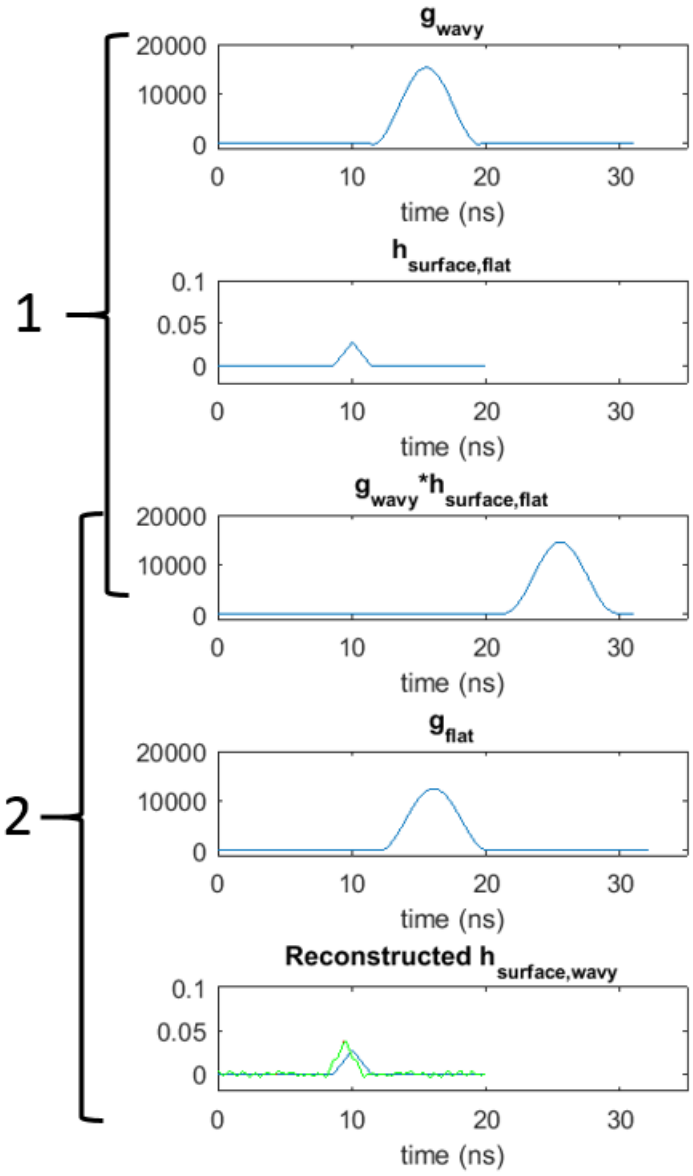

Figure 48: Performing a system identification of the interface transfer function during wavy conditions. The green waveform is the identified transfer function.

As discussed in Chapter 3, interface-transfer-function estimates may be used to improve seafloor reflectance estimates either by deconvolving them from full, waveform-resolved signals or by using their temporal extent to improve *STF* estimates used in Equation 3. Because reflectance estimation was not a part of the experiments, I have used simulated waveforms to study the possibility of improving estimated reflectance

with the proposed restoration procedure. Waveforms were produced with EOSL's radiometric simulator, which I developed during my Master's Thesis [50]. For these simulations, one theoretical scenario was examined: a low-frequency tilt of 10 degrees (see Figure 19). Seafloor reflectance, ρ, was then estimated from ALB signals generated from water depths of 1 m to 20 m in increments of 1m. The following three methods were used to estimate ρ:

(1) Use Equation 41 to identify the interface transfer function. Compute its FWHM. Add this value to other stretch functions' FWHM to compute STF. (Other stretch functions are laser pulse shape and seafloor stretching). Choose the peak value of the observed seafloor signal as the power received from the seafloor. Use Equation 3 to estimate ρ.

(2) Use Equation 41 to identify the interface transfer function. Deconvolve this function (and the laser pulse-shape function) from the waveform-resolved signal. Choose the peak value of the "sharpened" seafloor signal as the power received from the seafloor. Use Equation 3 with STF as 1 to estimate ρ.

(3) Use "SST-direct" to identify the interface transfer function. Deconvolve this function (and the laser pulse-shape function) from the waveform-resolved signal. Choose the peak value of the "sharpened" seafloor signal as the power received from the seafloor. Use Equation 3 with STF as 1 to estimate ρ.

All simulations used the settings listed in Table 7.

Table 7: Simulation settings for ALB-waveform reflectance estimation.

Parameter	**Value**
Altitude	400 m
ϕ_A	20°
Beam Divergence	7 mrad
K_D	0.04 m^{-1}
ρ	0.2
Optical Efficiency	0.35
P_T	1 MW
Pulse FWHM	1.3 ns
Receiver Aperture	6”

The surface stretching function was a triangle function with temporal width 1.75 ns (computed in Section 3.4). The seafloor was assumed to be flat. To account for inclined incidence on the seafloor, a Gaussian seafloor stretching function with FWHM equal to 0.99 ns was assumed. This value was computed by using Equation 30 with $\theta = 7.5°$ (the in-water refraction angle corresponding to in-air incidence of 10°) and with c divided by 1.33. Stretching from the water column and FOV loss were ignored. The system was assumed to be radiometrically calibrated with known counts-to-Watts mapping-function χ. System noise, modeled from Pathfinder system measurements, was the dominant noise source. A representative electrical domain waveform produced by the simulator is shown in Figure 49.

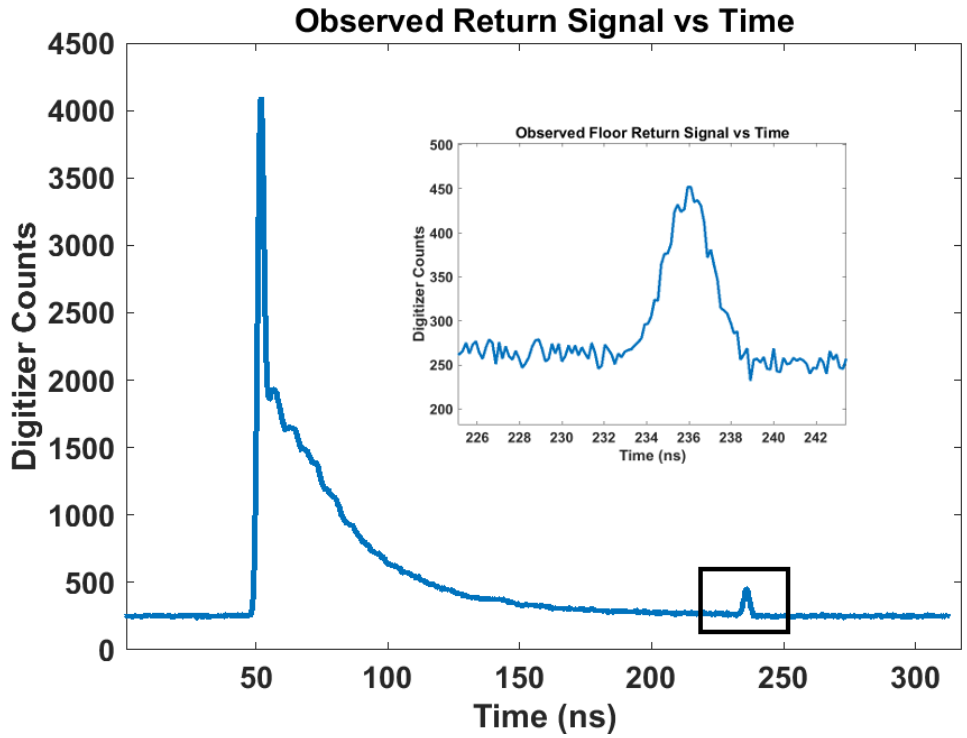

Figure 49: An electrical domain waveform characteristic of waveforms produced with EOSL's radiometric simulator.

Figure 49 shows an entire waveform-resolved signal measured in digital counts versus time. Digital counts are the output of an ALB system's digitizer; Pathfinder's provides 16-bit values. The boxed portion of the signal, corresponding to the seafloor signal, has been magnified for visualization purposes. Here, the seafloor signal is roughly 200 counts above the noise floor of the system. The peak value of this signal is directly related to ρ via Equation 3 after mapping the electrical signal to the optical domain using χ. However, because the seafloor signal has been stretched by the laser's pulse shape, the interface transfer function, and the floor transfer function, using the mapped Watts value as the seafloor power received will produce an underestimate of ρ. To illustrate why this is true, consider the signals shown in Figure 50. Here, the blue curve corresponds to the system's impulse response function. This represents the true signal that a system would detect in the absence of stretching. The next three curves from left to right show the effects of sequentially convolving the impulse

response function with the laser pulse shape, then the interface transfer function, and then the seafloor transfer function. The result of these sequential convolutions are the orange, yellow, and purple curves, respectively. Thus, the purple curve is the signal incident on the receiver that produced the electrical domain waveform shown in Figure 49. Since the peak of the purple curve is smaller than the peak of the blue curve, ρ will be underestimated when the purple curve alone is used to determine power received from the seafloor. Thus, the goal of signal processing is to account for this discrepancy in peak heights by estimating the STF parameter in Equation 3 or by deconvolving the transfer functions that introduce stretching so that seafloor received power may be estimated from a curve that resembles the blue curve as closely as possible.

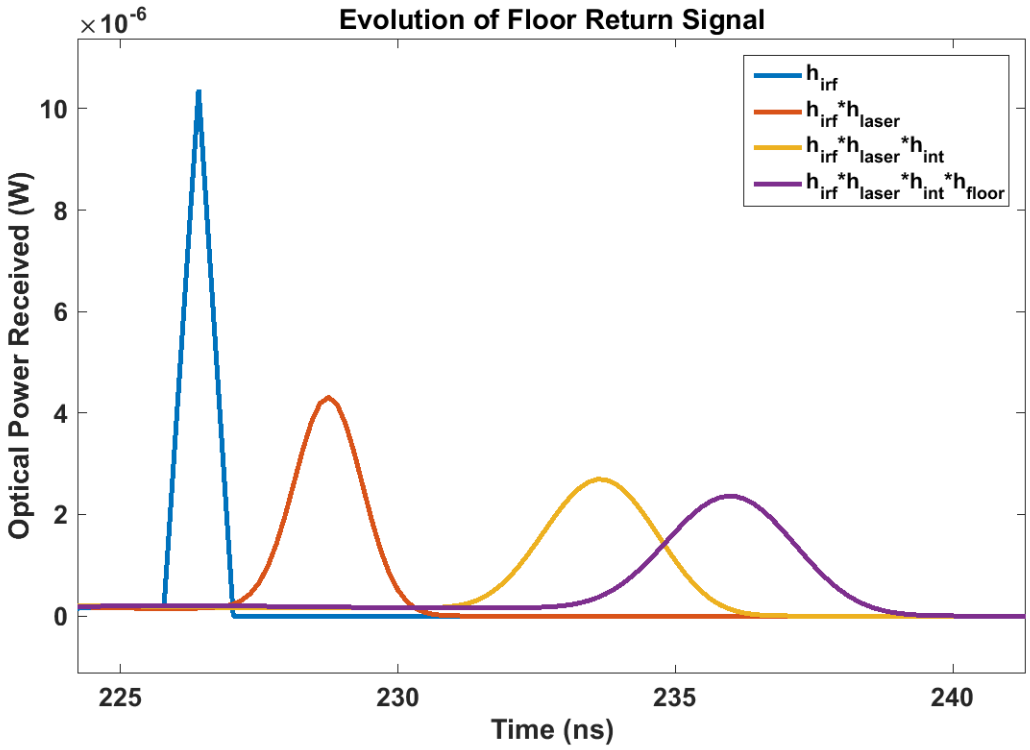

Figure 50: Evolution of the seafloor return signal from the impulse response function to the observed power incident on the ALB receiver.

The motivation behind the low-frequency tilted scenario presented here is that

systems assuming a flat air-water interface will use an incorrect stretching function at the interface. Consequently, estimates of ρ will be inaccurate, whether by incorrectly estimating STF or by deconvolving incorrect transfer functions from the observed seafloor signal. On the other hand, hybrid lidars constructing surface DSMs have the ability to identify the appropriate interface transfer function using the method outlined previously in this section. This more accurate transfer function may then be used together with other known transfer functions to estimate ρ more accurately. To this end, the simulations were performed and ρ was estimated using each of the three methods listed above. Figure 51 shows the results of using Method (1) to estimate ρ and Figure 52 shows the results of using Method (2) and Method (3) to estimate ρ.

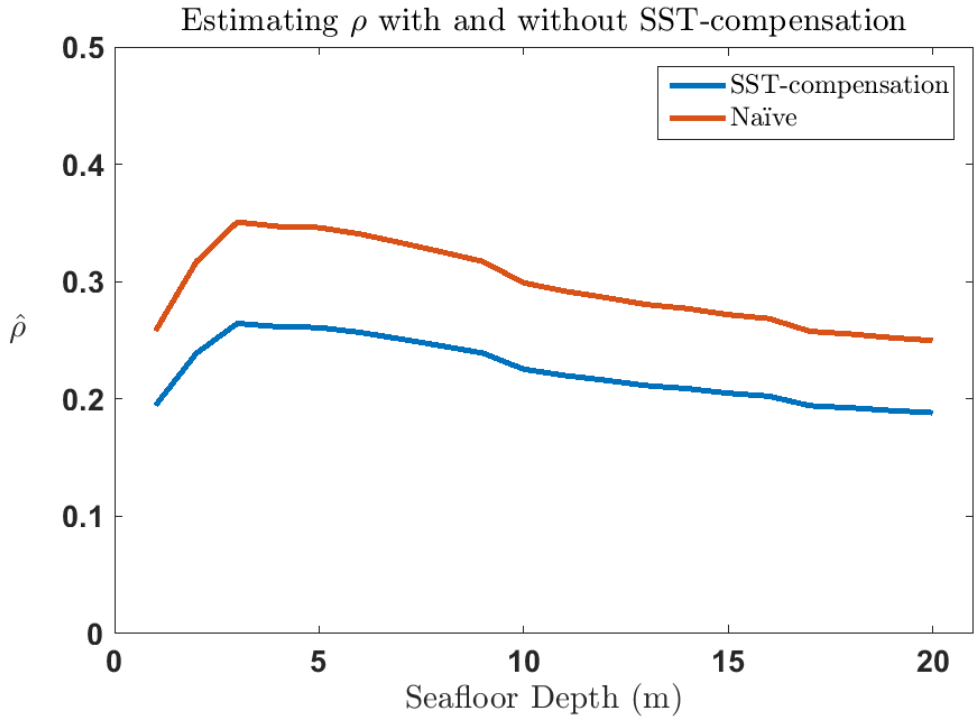

Figure 51: Estimating ρ at various seafloor depths with and without SST compensation informing the STF value in Equation 3. True value of ρ is 0.2.

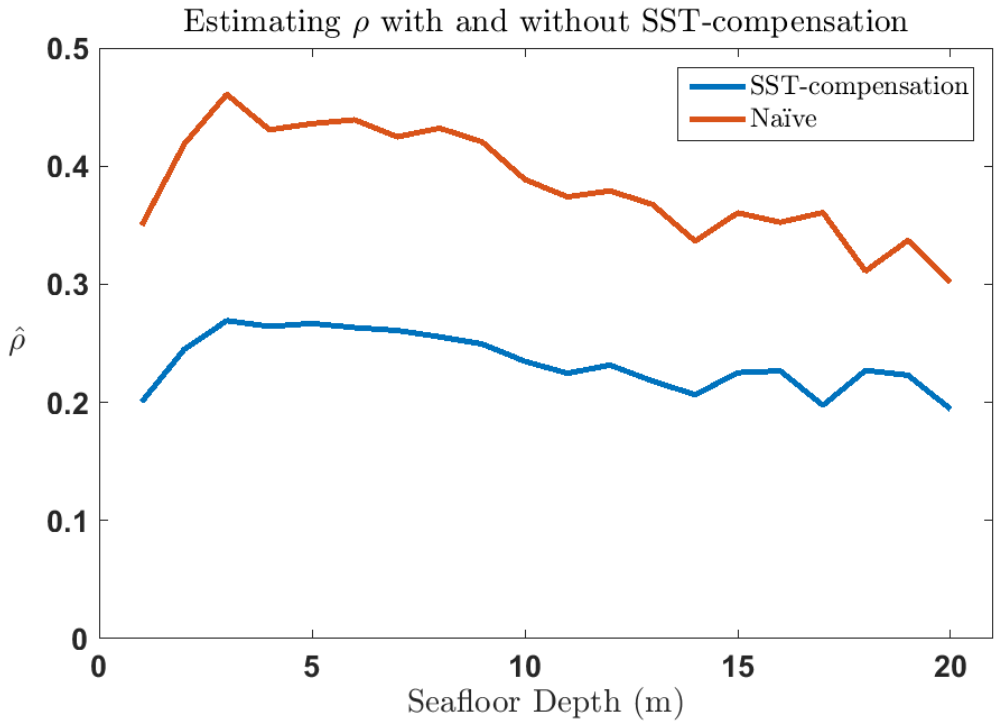

Figure 52: Estimating ρ at various seafloor depths with and without SST compensation informing interface transfer-function identification. True value of ρ is 0.2.

In both of these plots, estimation methods that compensate for SST are the blue curves; those that ignore SST are the orange curves. All methods use equivalent interest-point detection results (i.e. $\widehat{l_A}$, $\widehat{l_W}$, $\widehat{K_D}$, etc. are the same for blue and orange curves). SST-compensation methods assume perfect interface reconstruction. Therefore, these plots may be interpreted as best-case improvements from using system-identification of the interface-transfer function for this scenario. The true value of ρ is 0.2. Figure 51 shows that using SST-compensation when estimating STF for use in Equation 3 reduces error across all depths. On average, error reduction is 75%, arising from the constant 22% decrease in ρ estimates across all depths (i.e. both curves have the same shape). This can be explained as follows. The SST-compensation method always computes the interface contribution to STF as ${}^{1.75ns}/_{2}$ (the 10-degree triangle function's FWHM). Similarly, the naïve method always computes the interface contribution to STF as ${}^{3.62ns}/_{2}$ (the 20-degree triangle function's FWHM). Therefore, since

both methods assume a 1.3-ns laser-shape stretching function and a 0.99-ns seafloor stretching function, the ratio of their two computed STF values is 0.774. Here, this ratio represents the only difference between the two estimation methods. Because STF appears in the numerator of Equation 3, the SST-compensation method produces a 22% smaller estimate of ρ, which is always significantly closer to the true value of 0.2.

Figure 52 also shows that SST-compensation improves estimation of ρ. This figure has only two curves because Method (2) and Method (3) produce the same result, so they are both represented by the blue curve. For this example, Richardson-Lucy deconvolution with 25 iterations was used for naïve and SST-informed approaches. This algorithm was chosen because of its success in other lidar applications [76, 77]; and, 25 iterations were used because, when applied to a noiseless observed signal, iterations beyond 25 produced no further changes from the 25-iteration deconvolved signal. This figure shows that deconvolving an SST-informed pulse-stretching function before estimating the seafloor power received for use in Equation 3 reduces error across all depths. On average, error reduction is 82%. This improvement may be explained by the curves shown in Figure 53, which correspond to signals from the 20-meter-depth simulation. Here, the purple curve is the result of mapping the observed electrical signal (in digital counts) to its calibrated optical signal (in Watts) using the mapping function χ. Then, the naïve and SST-informed stretching functions are deconvolved from the calibrated, observed signal to produce the orange and yellow curves, respectively. The peak value of each signal is used as the seafloor power received when estimating ρ. Because the yellow curve resembles the true impulse response function more closely than the orange curve, the SST-informed methods produce better estimates of ρ. For this scenario, the naïve method always overestimates the seafloor power received because its assumed stretching function always has larger temporal extent than the true stretching function. Therefore, deconvolving this function from

the observed signal produces an "overly-sharpened" seafloor return, leading to an overestimate of the seafloor power received. This is very similar to the overestimation effects produced by the naïve method in Figure 51 resulting from overestimates of STF. In general, Figure 51 and Figure 52 show similar ρ-estimation trends, wherein SST-informed approaches significantly outperform naïve approaches. However, the deconvolution-based estimates are noisier than the STF-based estimates because of increased sensitivity to noise when selecting powers from deconvolved signals.

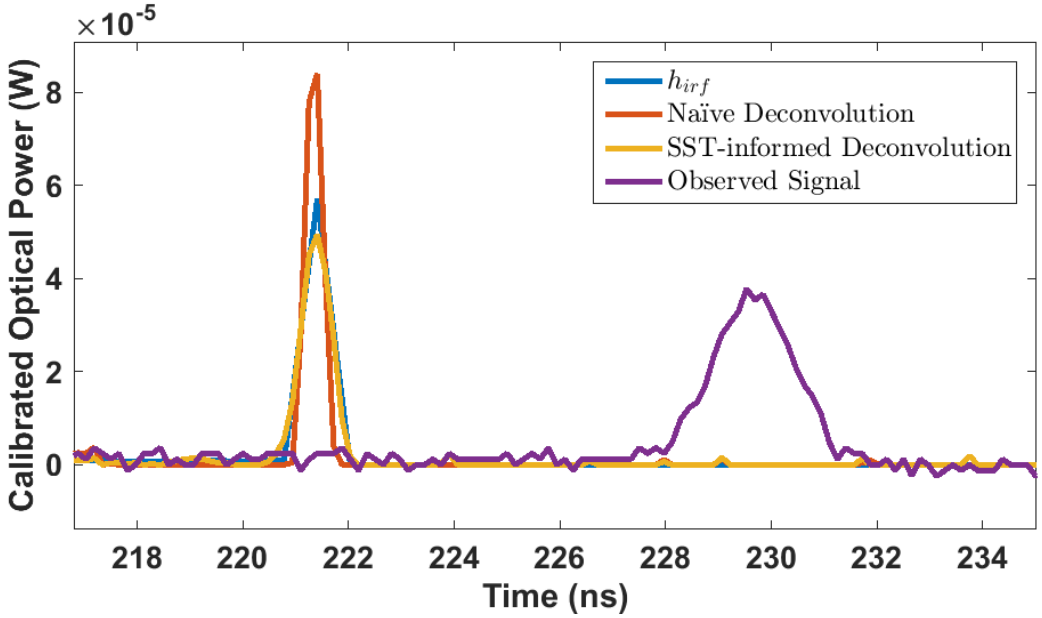

Figure 53: After using SST measurements to identify the interface transfer function, this function may be used to deconvolve the interface's effects from the calibrated seafloor signal (purple). The resulting signal (yellow) is a better representation of the true impulse response function (blue) than ignoring SST during deconvolution (orange).

The results presented in this section indicate that interface-induced stretching was successfully identified from waveforms collected by Pathfinder during wavy conditions. Pathfinder's co-temporally constructed DSMs were used to estimate pulse incidence on the surface, which was then regressed with the FWHM of the waveform's interface response. The slope of these regressions agreed well with expectation. Moreover, interface stretching was found to be strongly anti-correlated with interface reflection, agreeing with intuition. System identification of wavy interface transfer functions was

then performed, showing how the theory outlined in Chapter 3 may be applied to real data. In the absence of experimentally obtained reflectance data, simulations were performed with EOSL's radiometric simulator to show how identified system transfer functions may be used to improve estimates of ρ. For the low-frequency-tilt example considered, using identified interface transfer functions reduced ρ-estimation errors across seafloor depths from 1-20 m by 75%-82% on average.

4.5 Unified Restoration

Linear-mode, waveform-resolved systems can be viewed as single-pixel, ALB-imaging systems. Each pixel is produced by computing a seafloor coordinate and estimating its corresponding reflectance value from a transmitted pulse. Systems producing the best seafloor reflectance images will compute each pixel's coordinate and reflectance values most accurately. As referenced throughout this thesis, robustly accounting for air-water interface effects is a largely unaddressed problem in ALB, degrading systems' seafloor imaging capabilities. Coordinates computed by Equation 1 do not account for steering caused by non-flat interfaces; seafloor reflectances estimated by Equation 3 do not account for pulse-stretching effects introduced by non-flat, air-water interfaces. However, Pathfinder, using the novel processing techniques presented in this thesis, removes these limitations by using co-temporal, high-resolution SST measurements with its conventional green lidar. This hybrid-processing approach enables geometric reconstruction of seafloor coordinates and radiometric restoration of seafloor reflectance estimates. Unifying these two procedures produces a shift-variant restoration technique enhancing lidar-based seafloor imaging.

This thesis, until now, has purposefully separated ALB's geometric aspects from its radiometric aspects. However, these two are intricately intertwined when pertaining to seafloor imaging. Lidar-based seafloor images importantly depend on computed seafloor coordinates and reflectance estimates. When either aspect loses accuracy,

seafloor image quality degrades. As seen in Chapter 3 and Chapter 4, uncompensated SST adversely affects ALB both geometrically and radiometrically. ALB-system laser pulses are steered to unpredictable seafloor positions, producing coordinate computation errors; and, when detected, the pulses are unpredictably time-dilated, producing reflectance estimation errors. Therefore, uncompensated SST is one factor that limits ALB systems' ability to image the seafloor in two distinct ways. This thesis was designed to address this limitation by introducing new techniques to compute seafloor coordinates and reflectance estimates accurately even in the presence of waves. These techniques, presented as theory in Section 3.3 and Section 3.4, were validated by the results presented in Section 4.3 and Section 4.4, respectively. Therefore, when combined, these techniques should enhance seafloor image quality during wavy conditions.

Imaging through wavy SST, however, was not part of the experiments performed at the water tank facility (Section 4.1). Consequently, there is no experimental data with which to evaluate the geometric and radiometric techniques as pertaining to imaging. Instead, a simulation procedure was developed to do so, combining data from two separate collection campaigns at the water tank. One of these campaigns is the one detailed in Section 4.1, wherein Pathfinder was stationary and computed floor coordinates in the presence of waves. The other campaign is one that occurred in February of 2014, wherein Pathfinder was traversed and scanned to image an enlarged Georgia Tech (GT) logo mounted to a frame on the water tank's floor. Figure 54 shows a picture of this structure on the tank's floor during that campaign. Since both data collection campaigns were very similar, it is possible to blend data from each to simulate the effects of waves on Pathfinder's ability to image the GT logo. This may be accomplished by first creating a virtual water tank from the imaging campaign's data and then simulating waves on the surface equivalent to those experienced during the wavy data collection campaign. Pathfinder's ability to image the GT logo using the techniques presented in this thesis may then be analyzed during simulated wavy

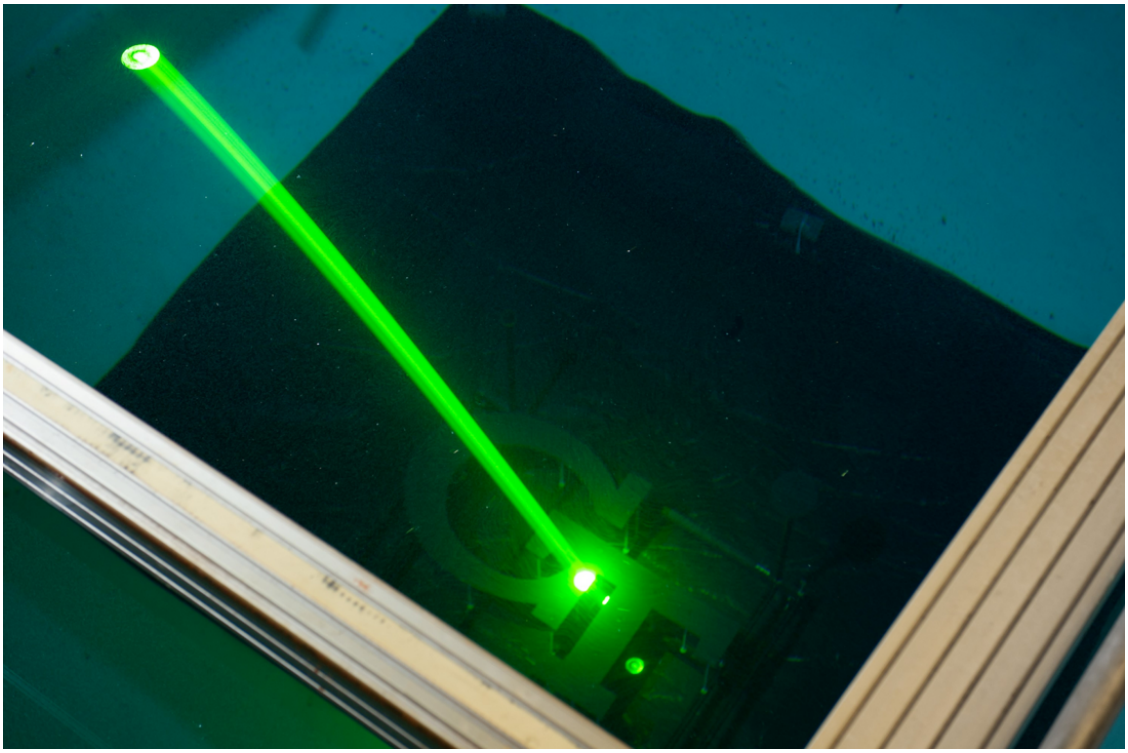

Figure 54: An enlarged Georgia Tech logo mounted on a frame at the bottom of the water tank was imaged during a previous data collection campaign at the water tank facility.

conditions in this virtual tank.

Figure 55 shows the floor point cloud produced from data collected during the 2014 imaging campaign. Here, points are colored by depth, with warmer colors (yellow) representing shallower depths and cooler colors (blue) representing deeper depths. The GT logo is clearly visible and raised approximately 60 cm above the tank's floor. The mounting frame is also visible, shown in green. The remaining points correspond to the tank floor (covered by the black tarp). The shadows, positions in the cloud where there are no points, arise from a combination of Pathfinder's scan pattern and the GT-mounted structure. Because a forward-looking arc pattern was used, the GT logo and frame cause point cloud dropouts in areas where pulses would have hit the the floor but instead were fully reflected by objects above it. Consequently, no signals reflect from these floor locations, effectively creating shadows. As seen from the axes labels, a forward-starboard-down coordinate system was used that was very similar

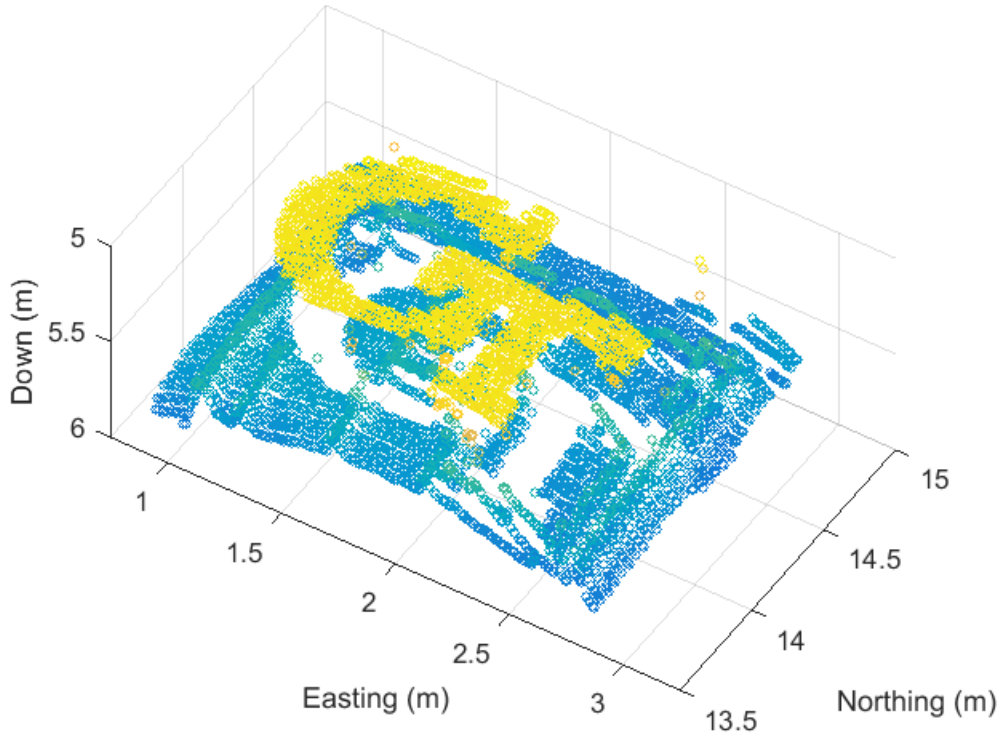

Figure 55: A floor point cloud produced from the 2014 data collection campaign.

to the one used in the wavy experiments. In fact, the axes were configured to be the same. The only difference between the two systems is their coordinate origin.

Seafloor images may be created from point clouds similar to Figure 55. This process usually involves generating raster images from the seafloor point cloud by binning, tinning, or kriging the coordinates [54]. Figure 56 shows one possible way to generate raster images using a binning procedure. Here, the top right image is a rasterized floor depth image. This image may be produced by first binning coordinates into 2cm-by-2cm bins (pixels) and then averaging the Down value of coordinates in each bin. Bins with no coordinates were assigned a Down value of 6 m. When point cloud coordinates also have attributed reflectance values, the same binning procedure may be used to create rasterized floor reflectance images. This may be done by averaging the reflectance estimates, instead of the Down value, in each bin. The

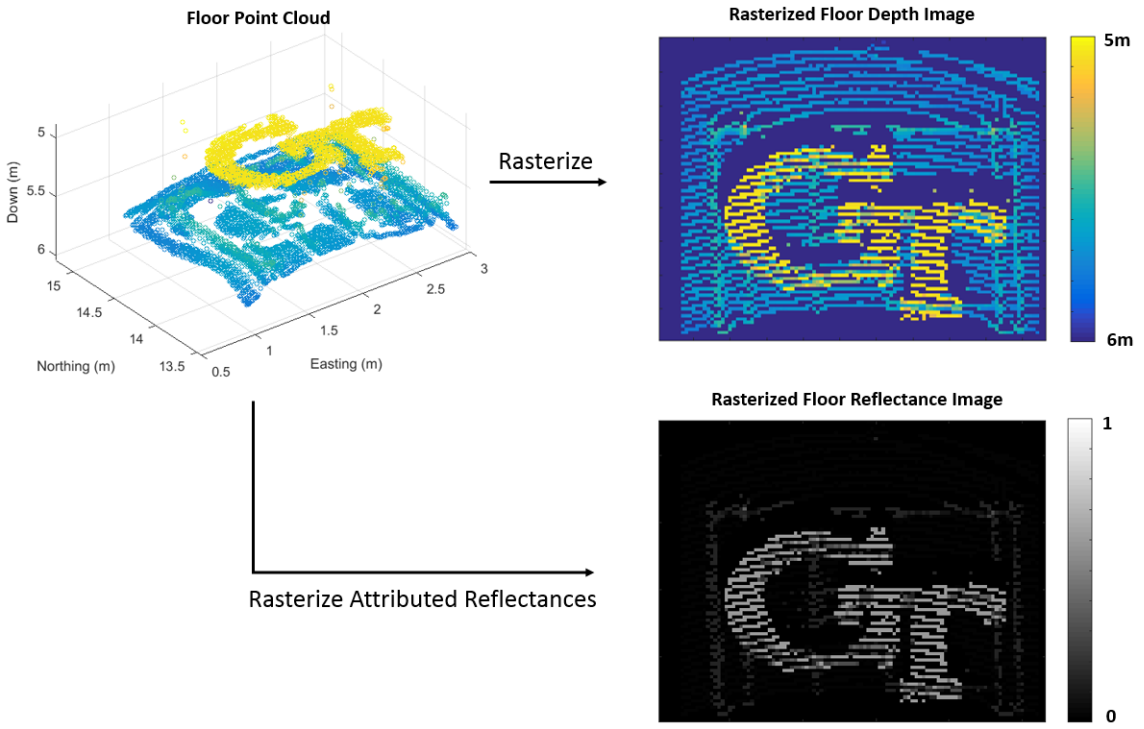

Figure 56: Seafloor point clouds may be rasterized to produce seafloor depth images. When reflectance values are attributed to points, rasterized seafloor reflectance images may also be produced.

image shown in the bottom right of Figure 56 was produced using that technique. In this case, however, the reflectance values attributed to each point are not real because there was no truth data. Therefore, this image was produced by assuming reflectance values of 0.6, 0.15, and 0.02 for the GT logo, the frame, and the floor, respectively. Bins with no coordinates were assigned reflectance values of 0.

A virtual water tank may then be created from the point cloud data and its (assumed) attributed reflectance data. Figure 57 shows one method to accomplish this. Here, depth profiles of the GT logo and the frame are derived from the point cloud. This may be done by extracting coordinates from the point cloud with depths only corresponding to those of interest. For example, to create the GT logo's depth profile, all coordinates with Down values between 5-5.1 meters were extracted from the point cloud and binned into 2cm-by-2cm bins. The average Down value of coordinates comprising a bin was then used as its value. The frame's depth profile was created

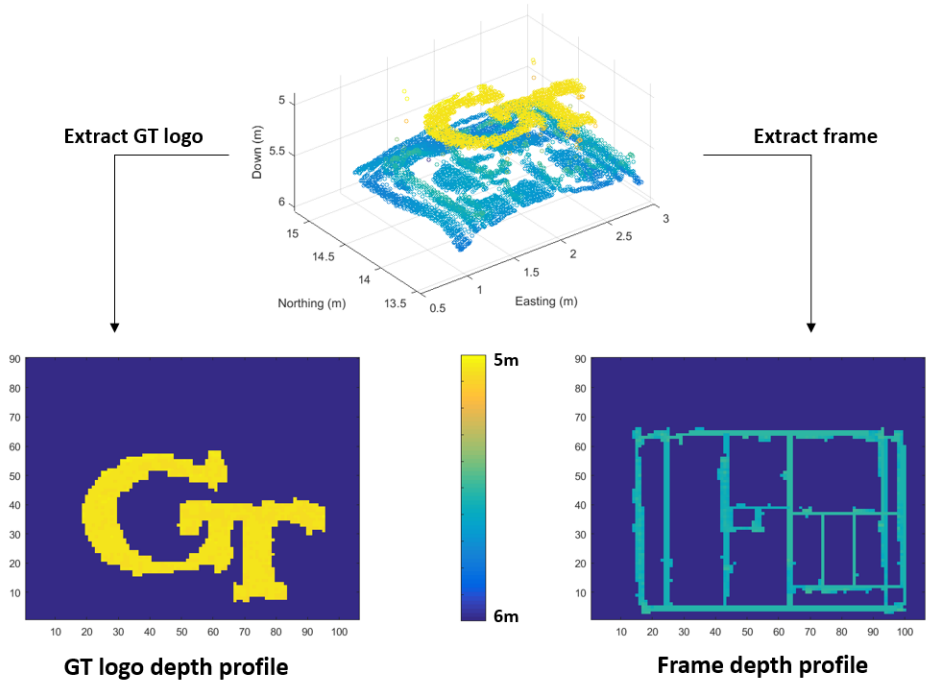

Figure 57: Seafloor point clouds may be rasterized to produce seafloor depth images. When reflectance values are attributed to points, rasterized seafloor reflectance images may also be produced.

similarly but used coordinates with Down values between 5.45-5.55 meters. In some locations of the frame's depth profile, shadows caused pieces of it to be missing. However, because the frame was built with straight pieces of aluminum, correcting this problem only required making straight lines to connect gaps in the profile. This was done by linearly interpolating the Down values of the known coordinates on either side of the shadow. These depth profiles, together with an assumed, constant, floor depth-profile of 5.6 m, may then serve as the floor topography of the virtual water tank. This information may be used to determine floor positions of rays traced through the water's surface during simulation. Importantly, because the coordinates used to create the profiles also have attributed reflectance values, any simulated ray determined to have intersected with the GT logo, frame, or floor may be assigned a reflectance value (e.g. 0.6, 0.15, or 0.02).

Pathfinder's scan pattern from the 2014 imaging campaign may be reproduced to

image the virtual tank's floor. This procedure involved translation in the Northing direction and scanning about the Down axis. Specifically, Pathfinder was translated in the Northing direction in increments of 5 cm from 11-12.5 m. At each Northing position, Pathfinder's scan angle was rotated from port to starboard. Rotation occurred in 13-arcminute increments (0.2167 degrees) from -1300 arcminutes to 1300 arcminutes (-21.67 degrees to 21.67 degrees). This procedure produced 6,231 unique combinations of Northing position and scan angle (hereafter called "firing positions"). To simulate laser pulses transmitted from the firing positions, rays may then be geometrically traced from the firing positions, through the water surface, and down to the depth profiles. The simulated in-water distance and reflectance value depend on which depth profile rays interacts with. By simulating wavy surfaces equivalent to those experienced during the wavy experiments, the hypothetical effects of imaging through wavy SST may be simulated by geometrically ray tracing through the simulated waves. Because the rays will be traced to different locations in the virtual water tank than they were during the actual data collection in 2014, simulated in-water depths and reflectance values will be different than those actually measured. These differences represent the effects of wavy SST.

Now that the virtual water tank has been established, the scan pattern has been replicated, and ray tracing can be used to determine where simulated laser pulses intersect the tank's floor during wavy conditions, the final step is to simulate waveforms modeling each unique scenario. Figure 58 shows a diagram of how this accomplished. First, the lidar's firing position is selected, establishing the orientation of the transmitted pulse's incident vector. Then a wavy surface is chosen from an acquisition in File 1, File 2, or File 3. As a simplifying assumption, the wavy surface is assumed to be a low-frequency tilt corresponding to the planar surface that would produce perfect beam steering to the NED coordinate computed from witness camera imagery. This planar surface's normal vector may then be used with the incident vector to ray trace

the laser pulse through the water surface to determine its refracted trajectory. The refracted beam is then propagated through the virtual tank to determine which depth profile it intersects. The traced in-water path length to the object and its attributed reflectance value are then reported as ray tracing results. These two values together with the surface normal's orientation (and in-air path length to the wavy surface) may be used to simulate a waveform modeling this scenario. This waveform represents the signal Pathfinder would theoretically detect when a laser pulse transmitted from the selected firing position interacts with the chosen surface orientation. This process may then be repeated for all 6,231 firing positions. Importantly, each file only contains 100 surface normal orientations, one corresponding to each of its acquisitions. Therefore, 6,231 firing positions' worth of surface orientations needed to be created. This was accomplished by repeating surface orientations after every 100 firing positions. For example, pulses transmitted from firing positions 1-100 each interact with a unique wavy surface. Then, the next 100 pulses, corresponding to firing positions 101-200, interact with the same respective surface orientations as used for firing positions 1-100. This process continues until firing position 6,231. While this creates a surface wave pattern that probably would not exist physically, the important result is that unique, ray tracing occurs at every firing position because the combination of incident vector, surface normal, in-air path length, in-water path length, and floor reflectance is always different.

Waveforms corresponding to each combination of firing position and surface orientation may be produced by repeating the process in Figure 58 for each file. These waveforms may then be processed to compute floor coordinates and reflectance estimates. Figure 59 shows how this may be done for two distinct processing paradigms. Here, simulated waveforms corresponding to the pertinent firing position and surface orientation are processed by either ignoring SST or by compensating for SST. Waveforms processed when ignoring SST model the naïve scenarios mentioned throughout

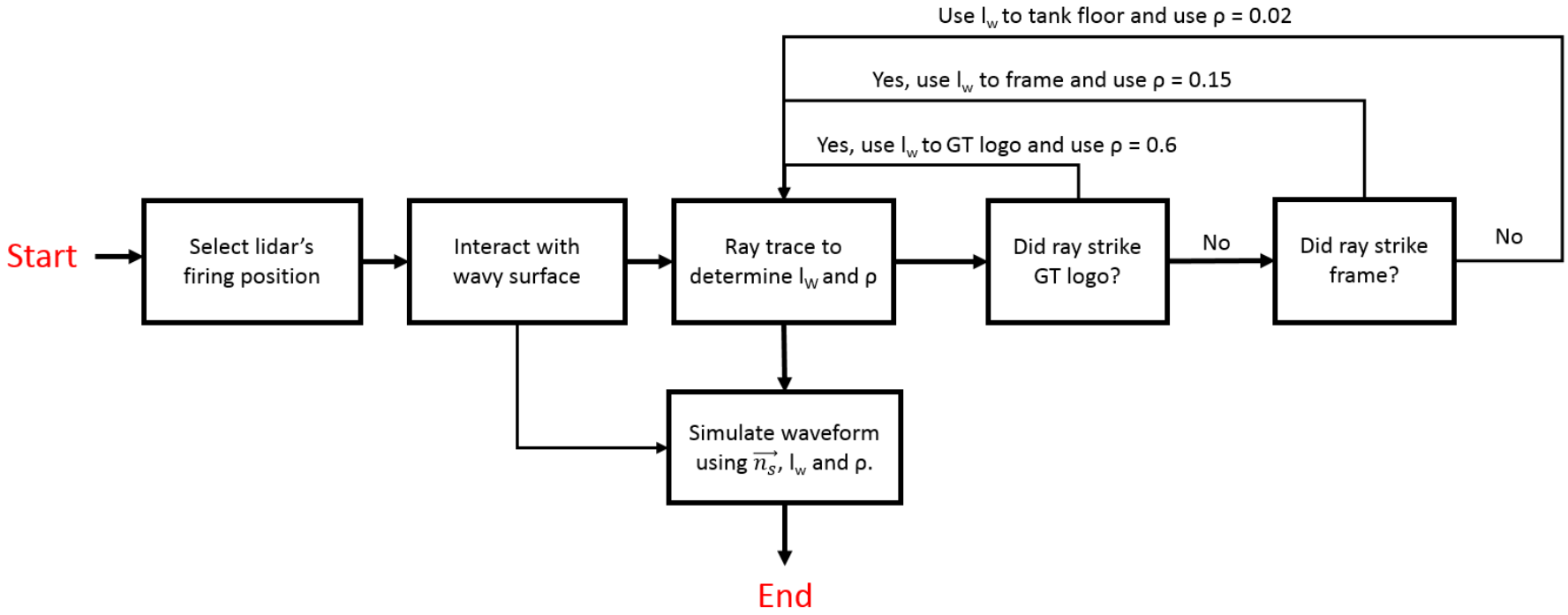

Figure 58: This process was used to simulate waveforms arising from the simulated wavy surfaces in a virtual water tank.

this thesis. Equation 1 is used to compute floor coordinates, and flat interface transfer functions are used when estimating ρ. Both the coordinates and reflectance estimates contain SST-induced errors that degrade image quality. On the other hand, waveforms processed when compensating for SST model the hybrid lidar scenarios mentioned throughout this thesis. Importantly, because the waves used for waveform simulation correspond to each acquisition's true wave surface, this processing scheme may use the GmAPD reconstructed surface normal corresponding to that wavy surface. Therefore, Equation 9 may be used when computing floor coordinates, and wavy interface transfer functions may be used when estimating ρ. Both the coordinates and reflectance estimates should contain less error than their naïve counterparts, consistent with the results presented in Sections 4.3 and 4.4. Consequently, by comparing both processing methods' produced images, SST-compensation techniques presented in this thesis may be evaluated against naïve seafloor imaging methods.

After performing a wavy simulation in the virtual tank for File 1 waves, a floor point cloud and its corresponding rasterized depth and reflectance images were generated ignoring SST. Figure 60 shows these results (compare to Figure 56). Here, the point cloud no longer contains a recognizable GT. Points have been blurred because the naïve coordinate computation technique may only compute floor coordinates along its pointing vector. In this example, that limitation manifests itself as the scanning pattern still being evident but the GT logo and frame features are not. These features are lost because wavy SST steers simulated beams to off-pointing-vector locations. This creates l_w values that when used in Equation 1 produce coordinates that do not correspond to the true positions causing signal reflections. Because of deteriorated point-cloud resolution, the corresponding raster images also exhibit severe blurring. The GT logo and frame are no longer recognizable. The reflectance image is also slightly darker than the original reflectance image, resulting from uncompensated interface stretching.

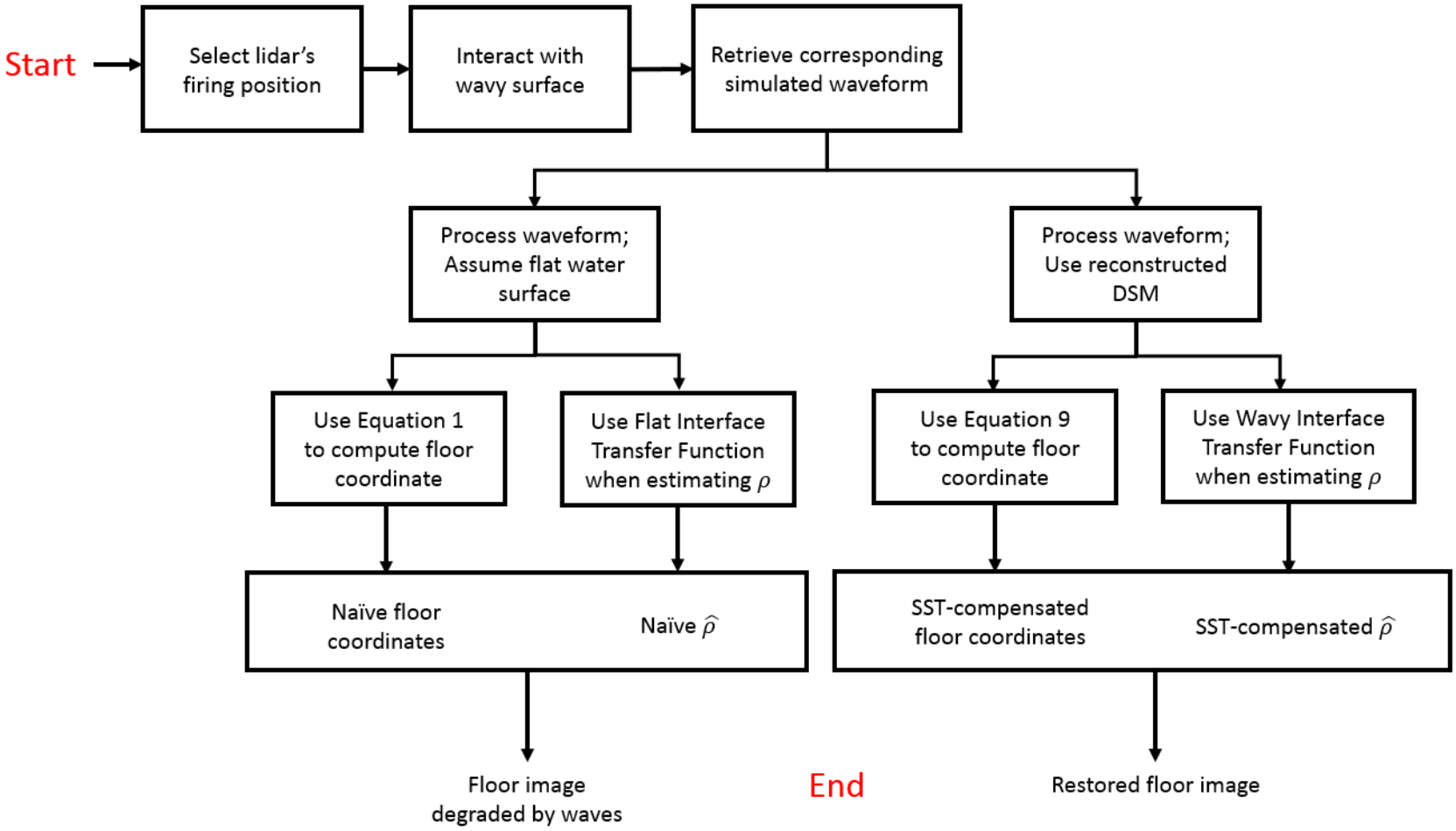

Figure 59: This process was used to evaluate the differences between observed and restored images. Observed images contain degradation due to pulse interaction with the simulated wavy air-water interfaces. Restored images use SST-compensation algorithms to geometrically reconstruct coordinates and radiometrically restore reflectance estimates.

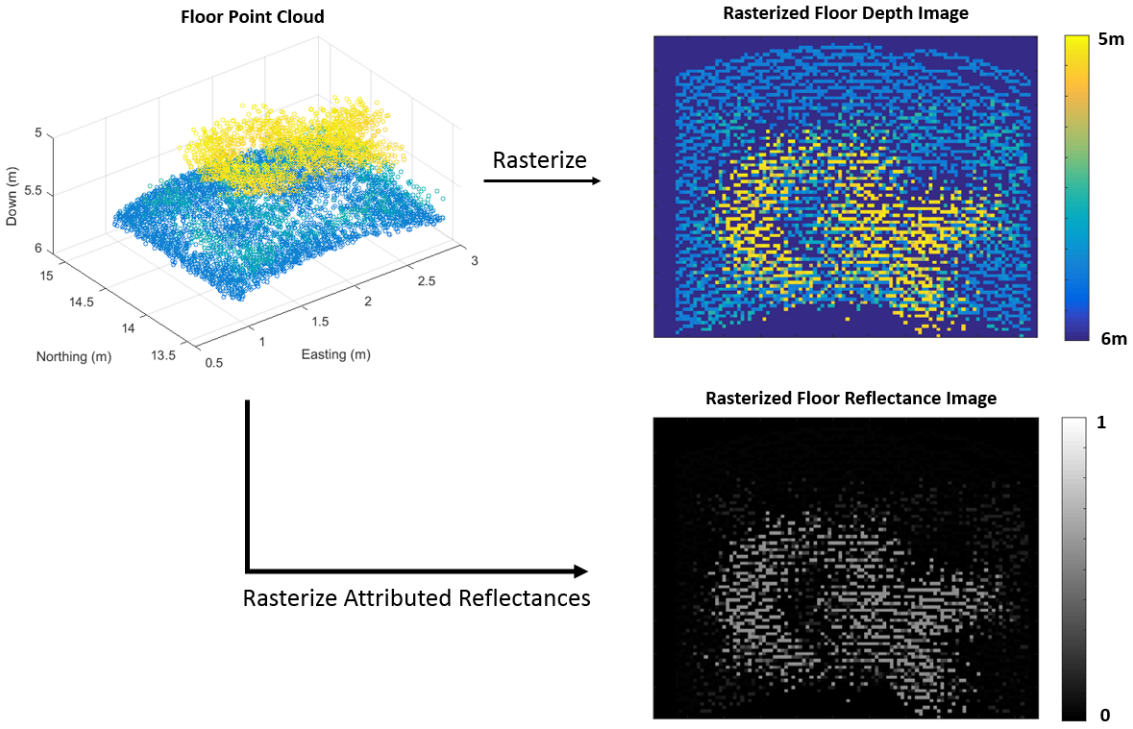

Figure 60: When left uncompensated, wavy SST degrades seafloor coordinate and reflectance measurements, causing degraded floor depth and reflectance images.

Figure 61 shows the true and observed reflectance images placed side-by-side, clearly illustrating the effects of wavy SST on lidar-based reflectance imaging. The true image contains sharp, distinct features while the observed image is an unrecognizable blur. When viewed as a linear systems problem, the true image has been convolved with the air-water-interface transfer function to produce the distorted and blurry observed image. Further complicating the problem is that this transfer function is shift-variant, as discussed in Chapter 3. However, the geometric and radiometric SST-compensation techniques presented in this thesis when used together enable identifying this shift-variant transfer function for each laser pulse. This identification makes image restoration possible. That is, unifying the geometric and radiometric techniques enables reversing the shift-variant transfer function's effects so as to restore observed reflectance images to ones that resemble their true images much more closely.

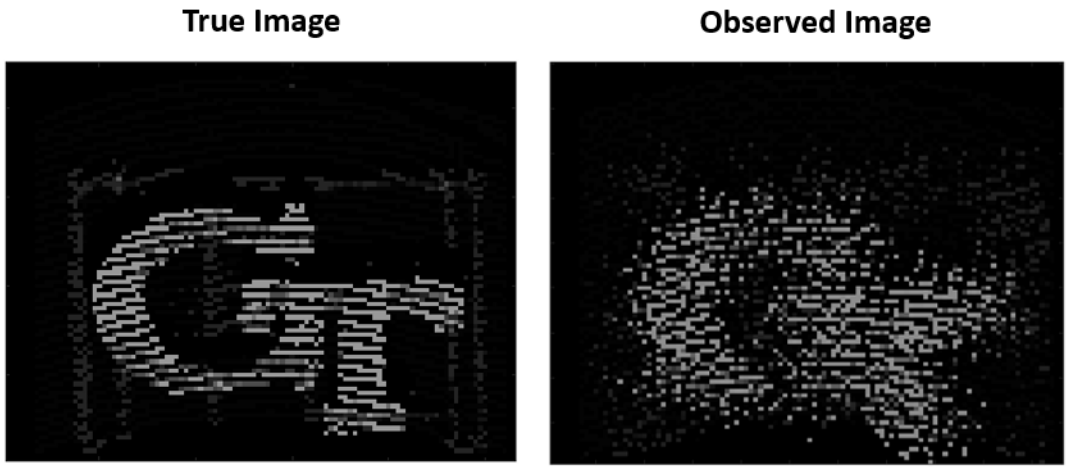

Figure 61: The shift-variant, air-water-interface transfer function degrades seafloor-reflectance image quality.

The following two-step procedure unifies the geometric reconstruction and radiometric restoration techniques into one shift-variant restoration technique for lidar-based seafloor imaging:

(1) Geometrically reconstruct coordinates in the observed image by using Equation 9.

(2) Radiometrically restore reflectance estimates attributed to each coordinate by using one of the three methods listed in Section 4.4.

After applying these two steps, a new rasterized reflectance image may then be generated. This restored image resembles the true image much more closely than the observed image. Importantly, this technique relies on having co-temporally constructed DSMs registered with waveform-resolved data. A hybrid lidar with a processing architecture like Pathfinder's is an ideal platform for this restoration procedure.

Now, return to the same simulation of File 1 waves in the virtual tank. These waveforms may now be processed in the second paradigm – wherein SST is compensated – and the two-step, restoration technique may be applied. Then, the effectiveness of the restoration may be evaluated by comparing the observed, restored, and true

images. For this restoration, the "6x6 DSM, PCA" method was used to reconstruct the surface orientation. Figure 62 shows the process of restoring the observed image.

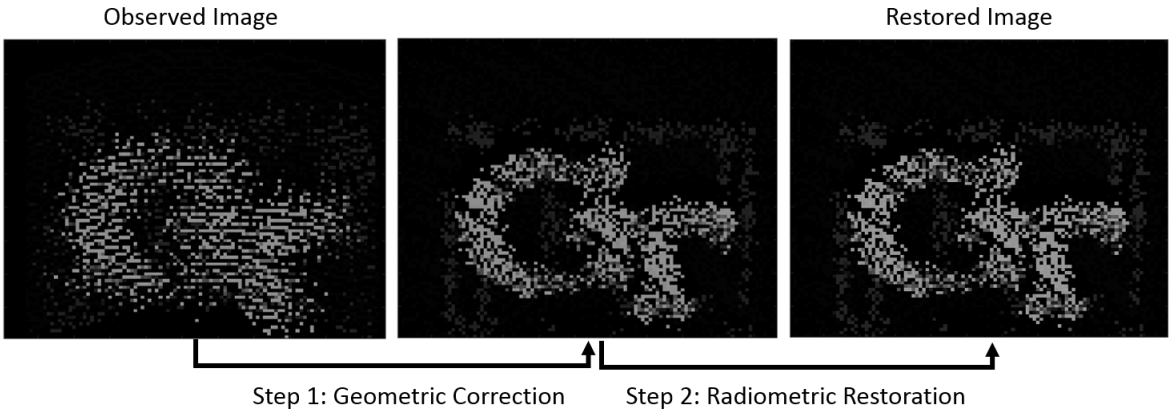

Figure 62: The unified, two-step restoration technique removes most of the image degradation introduced by wavy SST.

Here, Step 1 introduces the biggest perceivable change in the image. The observed image's unrecognizable GT logo and frame have been significantly sharpened. The letters are easily resolved and the frame's rigid structure is more evident. Next, Step 2 slightly brightens the image. This may be seen by comparing the histograms of reflectance estimates comprising the image, shown in Figure 63. The top histogram shows the values of reflectance estimates comprising the image without SST-compensation; the bottom histogram shows the values of reflectance estimates comprising the restored image. In both cases, the *STF* method was used when estimating ρ with Equation 3. The most noticeable difference between the histograms is the shift to the right of GT logo reflectance estimates in the bottom one. These values are closer to the true value of 0.6 than the naïve estimates are because the naïve reflectance estimates always assume a flat surface. This shift, along with other smaller right-shifts in the weaker reflectance values, cause the slight brightening of the reflectance image from Step 1 to Step 2.

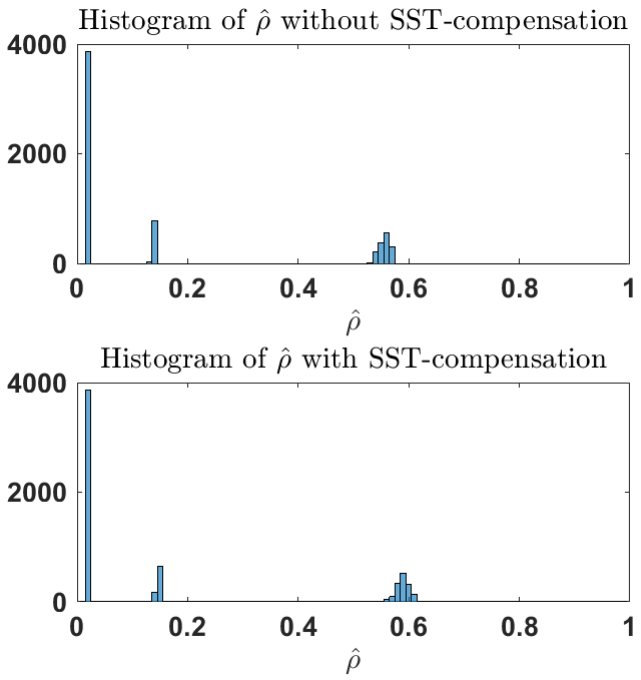

Figure 63: These reflectance estimate histograms illustrate the improvement in applying Step 2 of the restoration technique.

Therefore, from these results it may be concluded that the two-step restoration technique, combining geometric reconstruction and radiometric restoration, significantly enhances the degraded reflectance image. This enhancement directly correlates with a decrease in the SAS_{99} values of the coordinates comprising them. In the observed image, the average SAS_{99} value of coordinates was 52.61 cm; in the restored image, the average SAS_{99} value of coordinates was 44.34 cm. Figure 64 shows the observed, restored, and true images for comparison. It also shows the corresponding depth images. Depth images only require applying the restoration procedure's first step to be restored. For completeness, Figure 65 shows a diagram similar to Figure 56 and Figure 60 to enable quick comparison between the three scenarios – observed, restored, and true.

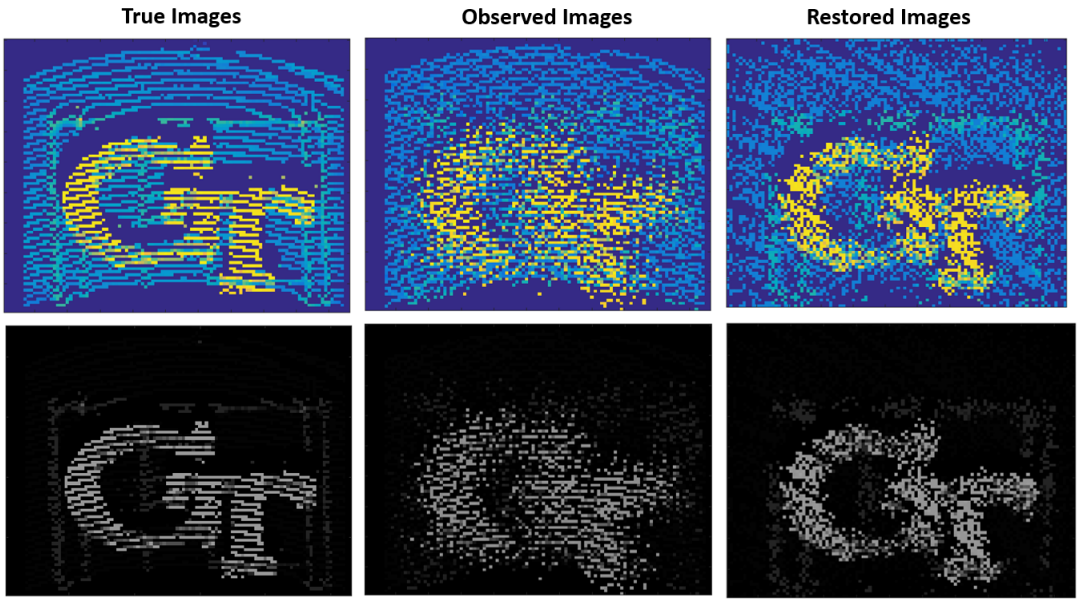

Figure 64: Observed, restored, and true images for simulated File 1 waves. The top row contains depth images and the bottom row contains reflectance images.

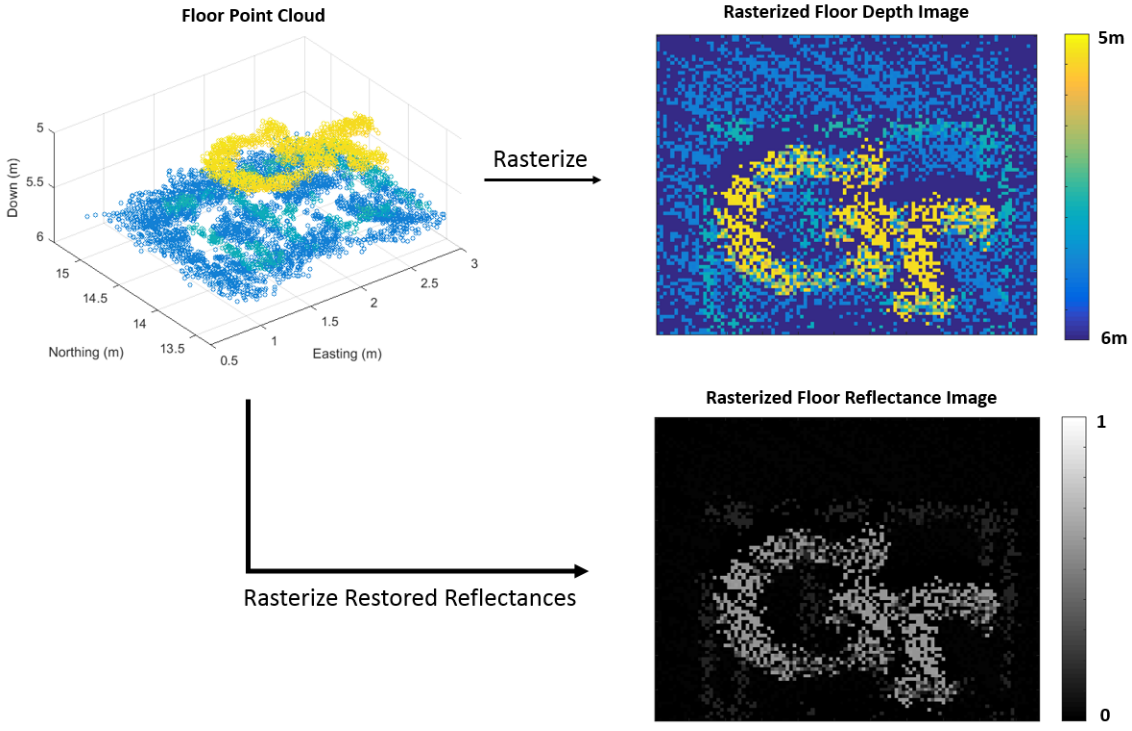

Figure 65: After applying the shift variant-restoration technique, restored depth and reflectance images resemble their respective true images much more closely.

Similar simulations were also performed for the waves recorded in File 2 and File 3.

The unified restoration procedure was then applied to the observed images to restore them. The true, observed, and restored images for these files are shown in Figure 66 and Figure 67, respectively. Although the observed images in these examples are not as degraded (because the waves were smaller) the restored images also exhibit significant enhancement after applying the restoration technique. In all cases, letters are easily resolved and the frame's rigid structure becomes more evident. Moreover, average SAS_{99} values of coordinates in all restored images are smaller than their respective observed images (File 2: 44.43 cm vs. 46.79 cm; File 3: 45.98 cm vs. 48.45 cm). This trend in SAS_{99} also applies to the observed images. Average SAS_{99} of File 2 (44.43 cm) is smaller than that of File 3 (45.98 cm), which is smaller than that of File 1 (52.61 cm). Consequently, image degradation of File 2 is less than that of File 3 which is also less than that of File 1. Therefore, average SAS_{99} may be used as a first-order image quality metric.

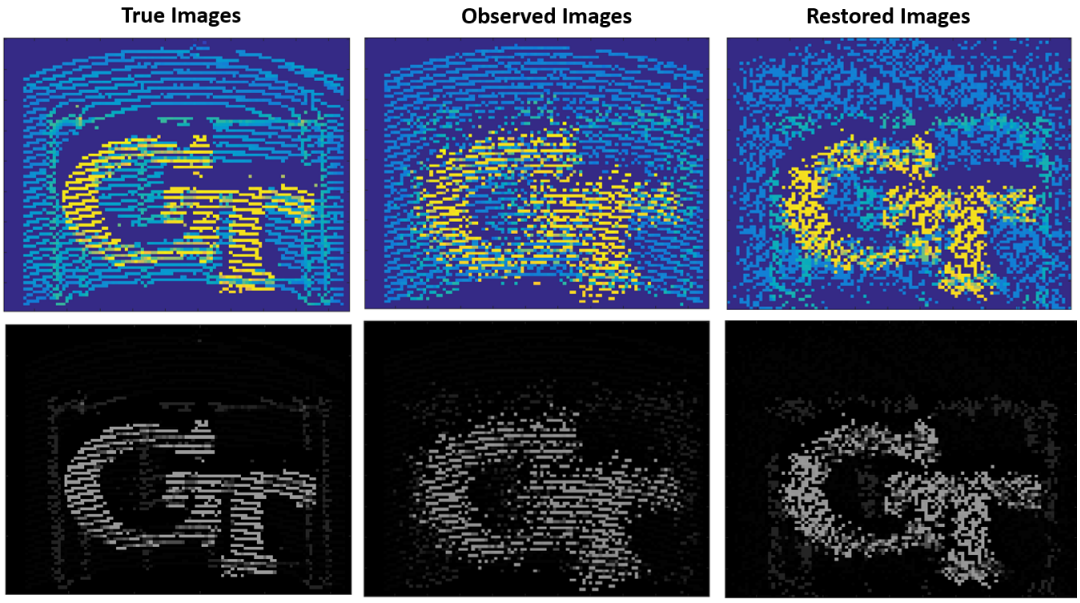

Figure 66: Observed, restored, and true images for simulated File 2 waves. The top row contains depth images and the bottom row contains reflectance images.

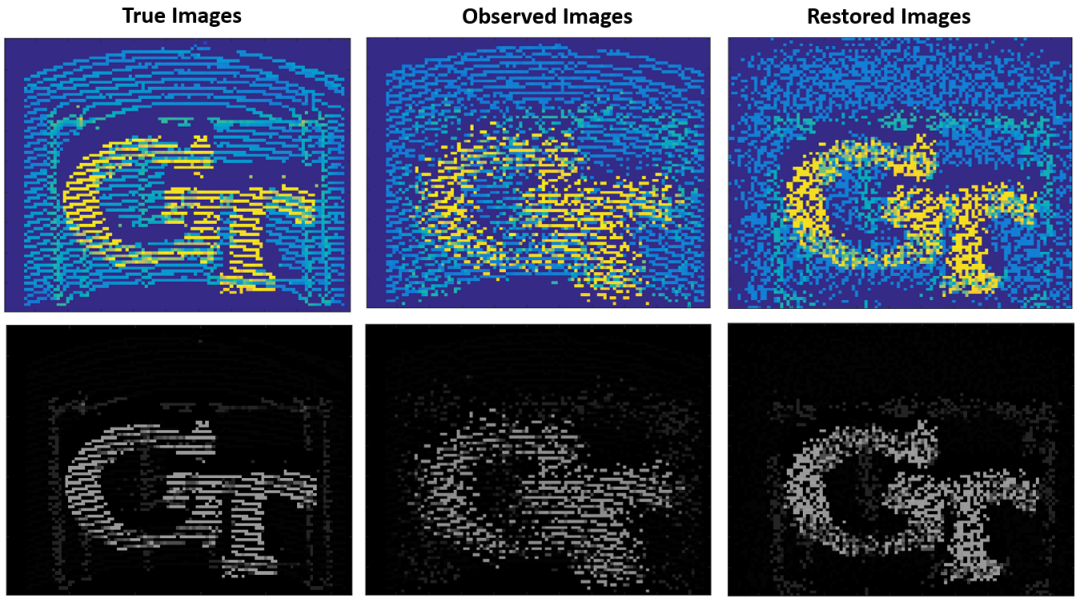

Figure 67: Observed, restored, and true images for simulated File 3 waves. The top row contains depth images and the bottom row contains reflectance images.

Because GmAPD reconstruction of the wavy surfaces was not perfect, restored images still contain some errors in coordinate positions and reflectance estimates. Therefore, it is instructive to observe the restored images resulting from perfect interface reconstruction. Figure 68 shows "perfectly restored" depth and reflectance images for File 1, File 2, and File 3 beneath the true images at the top. These perfectly restored images represent the best possible image restoration achievable by the unified restoration technique when waves are perfectly reconstructed.

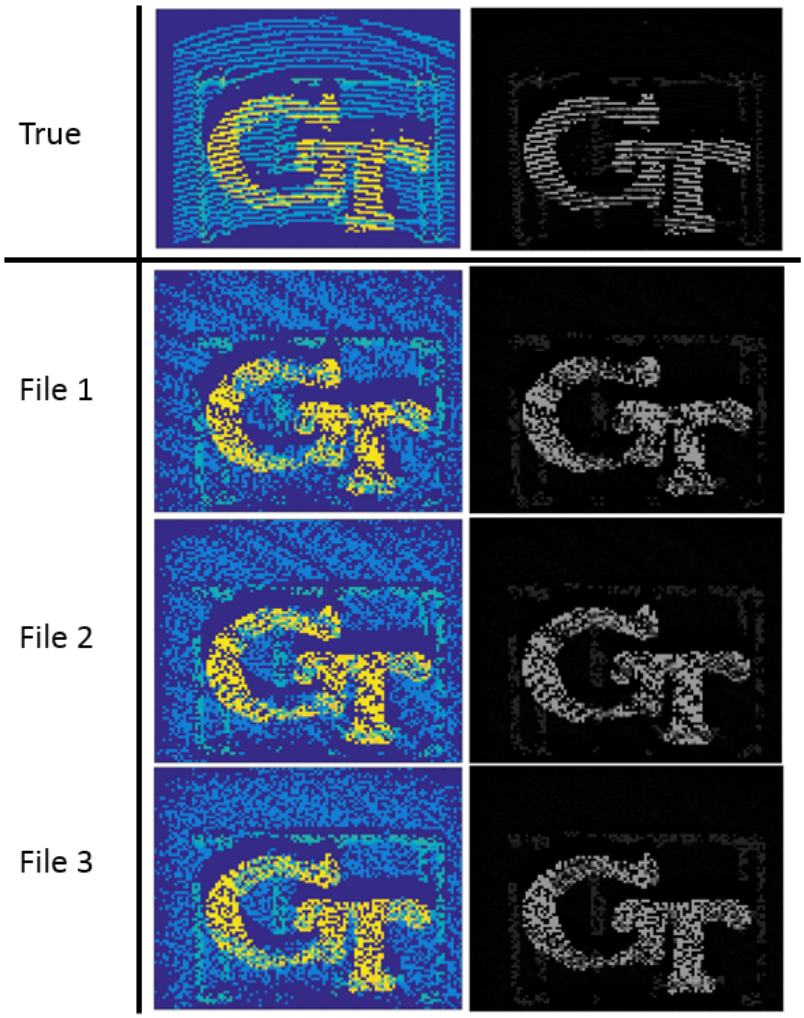

Figure 68: These depth and reflectance images were produced using the unified restoration technique after perfect reconstruction of the air-water-interface. These represent the best possible restoration achievable using this method.

The results presented in this section indicate that the geometric and radiometric SST-compensation strategies may be used together in a unified technique to improve lidar-based seafloor imaging. This unified technique is a two-step process, relying first on geometric reconstruction and then on radiometric restoration. Observed images with blurring degradation arising from the shift-variant, air-water-interface transfer function may be enhanced by applying this restoration procedure. In all three simulated cases, restored images closely resemble the true images. Had perfect reconstruction of the air-water-interface been achieved, the restoration procedure produces

images nearly identical to the true images, indicating that more image enhancement is possible by reducing seafloor coordinate error. Importantly, SAS_{99}, a coordinate accuracy metric, may also be used as seafloor-image quality metric. In all naïve seafloor images, the average SAS_{99} values of coordinates comprising them were larger than those in the restored images, indicating less accuracy. Consequently, their image quality was worse than that of the restored images. Moreover, all observed images exhibited the same trend. Observed images with less image degradation had smaller average SAS_{99} values, while those with more severe image degradation had larger average SAS_{99} values. Therefore, this shift-variant restoration technique should be coupled with interface reconstruction strategies that reduce the average SAS_{99} value of seafloor coordinates to produce better imagery.

CHAPTER V

CONCLUSIONS

This chapter summarizes the research presented in this thesis and offers directions for future work. These summaries identify my contributions to ALB and provide areas to build upon my work. This chapter begins with stating the goals of the thesis and how they were achieved. My research is then summarized and specific contributions are identified. The chapter then presents potential future work and concludes with a list of publications related to this research.

The goal of this thesis was to present a shift-variant restoration technique leveraging high-resolution interface modeling in lidar-based seafloor imaging. This technique is a restoration procedure for seafloor images degraded by wavy air-water interfaces. The novel geometric and radiometric SST-compensation strategies presented in this thesis are the basis for this restoration. When unified in a two-step process, wherein coordinates comprising the image are geometrically reconstructed and then the attributed reflectance estimates are radiometrically restored, the resulting procedure enhances degraded floor imagery. SST-compensation strategies also reduce coordinates' SAS_{99}. When smaller, this coordinate accuracy metric generally indicates better imagery. The novel processing architecture designed for the world's first hybrid lidar employing synchronized Geiger-mode and linear-mode lidars is an ideal platform for implementing this technique.

5.1 Summary

ALB systems have provided important intelligence, surveillance, and reconnaissance capabilities in coastal areas since their inception in the 1980s. Hardware and software

improvements over the past few decades have driven increases in system accuracy, resolution, and reliability. These improvements have also enabled the production of new data products, one of which is seafloor reflectance imagery. Lidar-based reflectance imagery depends on the accuracy of the seafloor coordinates and reflectance estimates comprising them. One accuracy-limiting factor is wavy SST, which affects seafloor reflectance images in two ways. First, images are geometrically distorted by uncompensated beam steering induced by the air-water interface. Second, images are radiometrically distorted by uncompensated pulse stretching induced by the air-water interface. These two distortions manifest themselves as severe blur in observed reflectance imagery. When viewed in the context of linear systems theory, wavy interface transfer functions cause this shift-variant image degradation. To reverse the interface's effects, the transfer function must be identified for each laser pulse. This may be accomplished by constructing high-resolution DSMs of the interface co-temporally when processing waveform-resolved data. Seafloor coordinates may then be geometrically reconstructed by ray tracing through the DSM; and, seafloor reflectance estimates may be radiometrically restored by first deconvolving the interface transfer function from the waveform-resolved signal and then using the resulting signal when inverting the radiative transfer equation. Unifying these two aspects into a two-step procedure produces an image restoration technique that significantly enhances lidar-based, seafloor-reflectance images degraded by wavy SST. One heuristic for evaluating the image enhancement is using coordinates' SAS_{99} values during restoration. A possible processing platform that may implement this technique is a hybrid lidar combining an IR, Geiger-mode system with a green, waveform-resolved system.

5.2 Original Contributions

- New geo-location equation - A newly-derived seafloor-coordinate-computation equation that accommodates for arbitrary beam steering at the air-water interface during real-time data collection.

- New total propagated uncertainty model - A newly derived uncertainty model that for the first time characterizes the effects of air-water-interface uncertainty on seafloor coordinate uncertainty.

- Improvement of coordinates computed during wavy conditions - Achieved up to 40% reduction in floor coordinate error when applying geometric reconstruction techniques during observed wavy conditions.

- Identification procedure of wavy air-water interface transfer functions - This procedure enables identifying wavy interface transfer functions from combinations of DSM and waveform-resolved data. The resulting transfer functions may be deconvolved from detected signals to improve seafloor reflectance estimates.

- Shift-variant, image-restoration technique - A unified, two-step procedure combining the geometric and radiometric SST-compensation strategies that significantly restores imagery degraded by wavy SST.

- Identification of SAS_{99} as an image quality metric - SAS_{99} had previously only been suggested as a measure of coordinate accuracy. When used to assess image quality, images containing coordinates with smaller SAS_{99} values were found to have less degradation than those with larger SAS_{99} values. SAS_{99} may therefore be used as a heuristic for selecting interface reconstruction strategies that minimize it to enhance image restoration.

- Hybrid-lidar processing architecture - A data processing architecture designed to synchronize interface measurements with waveform-resolved signals, enabling

registration of co-temporally constructed interface DSMs with waveforms.

- Hybrid-lidar co-incidence processing algorithms - New histogram-trimming methods that use waveform-resolved data to de-noise Geiger-mode data.

- Hybrid-lidar, waveform-resolved processing algorithms - New methods to compute seafloor coordinates by performing parallelized ray tracing through interface DSMs in a mixed-mode computing architecture [46].

5.3 Future Work

This thesis continues to push the capabilities of ALB system design and performance. Surveys employing contributions presented in this work may achieve the following:

- higher survey accuracies by implementing the geometric correction technique;

- cheaper surveys by implementing the new TPU model in real-time;

- extension of the operational window of surveys while remaining within IHO requirements by implementing the geometric correction technique and TPU model in real time; and,

- detection of smaller features in seafloor imagery by applying unified restoration technique.

These advancements were shown to be possible for the experimental and simulated conditions specified in this thesis. However, not all theory was validated experimentally. Future work should necessarily include this. A first step may be to validate the geometric and radiometric techniques as they pertain to imaging in a controlled experiment. One possible way to accomplish this is to return to the water tank facility and re-deploy the GT logo and frame after having characterized its reflectance. Pathfinder may then be translated above the tank and its laser scanned in an airborne-like manner while waves disturb the surface. The resulting observed and restored images may

then be analyzed as they were in this thesis. The restored images should exhibit significant enhancement.

The geometric and radiometric techniques should also be validated in an airborne deployment. The effects of sea spray on GmAPD interface measurements may then be characterized and managed appropriately. Moreover, because the green footprint on the surface will be much larger, the ability to detect sub-footprint SST structures may also be analyzed. In this thesis, spacing between GmAPD measurements was so small that typical ranging errors caused severe distortions in sub-footprint normal vectors. Thus, a simplifying assumption was put in place to construct only planar DSMs. In the airborne case, spacing between measurements will be much larger, allowing for removal of this assumption. The resulting DSMs may then be inspected for high-frequency content. If DSM accuracy and resolution are sufficient, introducing high-frequency SST corrections may be possible. Another simplifying assumption used in this thesis was the 0.1-second wave epoch. This value should be re-evaluated after performing airborne measurements and adjusted appropriately if necessary. Finally radiometric restoration capabilities may also be analyzed when water column scattering and stretching affect the shape of the seafloor returned signal. In this thesis, water column scattering and stretching were assumed as negligible because of the tank's extremely clear water. In real-world, airborne-deployed scenarios, aside from Hawaiian-like waters, scattering in the water column will also degrade reflectance estimates.

Finally, this thesis only skimmed the surface of hybrid lidar capabilities. Tremendous potential exists both in bathymetric and topographic applications. Regarding bathmetry, this thesis only explored the capabilities of an array-based IR, Geiger-mode lidar for surface characterization. However, if green Geiger-mode technology, or other green, array-based measurements, were to enter the field of ALB, then radiometric correction of seafloor rugosity may also become possible. By synchronizing a

waveform-resolved green system with a green Geiger-mode system, the seafloor signal from the waveform-resolved system could be used to gate the Geiger-mode system so as to accept only seafloor signal photons. This may be done in a manner very similar to the novel, co-incidence processing technique for IR interface returns presented in this thesis. Regarding topography, Geiger-mode systems have become increasingly prevalent as the system of choice. However, their measurements still suffer from significant noise. One way to de-noise that data and improve system accuracy would be to add a waveform-resolved lidar operating synchronously with their current system and use the waveform-resolved signal to gate their Geiger-mode measurements. Once again, this procedure would be similar to the novel co-incidence processing technique developed in this work.

5.4 Publications, Conference Proceedings, and Technical Reports

The following papers I have authored or co-authored are directly related to research presented in this thesis:

- D. Carr, "A study of the target detection capabilities of an airborne lidar bathymetry system," Master's thesis, Georgia Institute of Technology, 2013.
- G. Tuell and D. Carr, "New Procedure for Estimating Field-of-View Loss in Bathymetric Lidar," in *Imaging and Applied Optics, OSA Technical Digest*, July 2013.
- D. Carr and G. Tuell, "Estimating field-of-view loss in bathymetric lidar: application to large-scale simulations," *Appl. Opt.*, vol. 53, pp. 4716-4721, July 2014.
- G. Tuell, R. James, R. Ortman, C. Valenta, D. Carr, and J. Zutty, "Qualification testing of the agilent m9703a digitizer for use in a bathymetric lidar," in

emphGeoscience and Remote Sensing Symposium (IGARSS), 2014 IEEE International, pp. 2703-2705, July 2014.

- G. Tuell, D. Carr, N. Guida, M. O'Shaughnessy, "Procedures and Algorithms for Raytracing Lidar Measurements Through An Irregular Sea Surface," Technical Report to NOAA, May 2015.

- G. Tuell, D. Carr, N. Guida, M. O'Shaughnessy, "On the Relationship between Resolution of Sea Surface DEMs and Accuracy of Refracted Angle based on Analysis of Empirical Data," Technical Report to NOAA, July 2015.

- G. Tuell, D. Carr, N. Guida, M. O'Shaughnessy, "Strategies for Mitigating Sea Surface Effects in the Workflow of Deployed Topo-Bathy Lidar Systems," Technical Report to NOAA, Sept 2015.

- R. Ortman, D. Carr, R. James, D. Long, M. O'Shaughnessy, C. Valenta, and G. Tuell, "Real-time, Mixed-mode Computing Architecture for Waveform-resolved Lidar Systems with Total Propagated Uncertainty," in *SPIE Laser Radar Technology and Applications XXI*, April 2016.

- G. Tuell and D. Carr, "A Hybrid Lidar Approach to Compensation of Sea Surface Beam Steering for Bathymetric Lidar," in *Geoscience and Remote Sensing Symposium (IGARSS), 2016 IEEE International*, July 2016.

APPENDIX A

SUPPLEMENTARY MATH

To determine the expression for χ, start by extracting the SBF coordinate equation from Equation 9 and explicitly solve for the incident unit vector, resulting in:

$$\vec{i} = \begin{bmatrix} \cos(\theta)\sin(\phi_A) \\ \sin(\theta)\sin(\phi_A) \\ \cos(\phi_A) \end{bmatrix}$$

Next, assume:

$$\vec{n_s} = \frac{1}{norm} \begin{bmatrix} A \\ B \\ -1 \end{bmatrix}$$

where:

$$norm = \sqrt{A^2 + B^2 + 1}$$

Then, use Equation 23 to solve for $\vec{r}$, which results in:

$$\vec{r} = \begin{bmatrix} \cos(\theta)\sin(\phi_A) \\ \sin(\theta)\sin(\phi_A) \\ \cos(\phi_A) \end{bmatrix} + \chi \begin{bmatrix} A \\ B \\ -1 \end{bmatrix}$$

where:

$$\chi = \frac{\eta\left(\frac{-\sin(\phi_A)(A\cos(\theta)+B\sin(\theta))-\cos(\phi_A)}{norm}\right) - \sqrt{1+\eta^2\left(\left(\frac{-\sin(\phi_A)(A\cos(\theta)+B\sin(\theta))-\cos(\phi_A)}{norm}\right)^2-1\right)}}{norm}$$

APPENDIX B

TPU DERIVATIONS FOR OLS

To determine expressions for J_I, J_o, and Σ_I, start with the OLS surface-normal system-of-equations (in implicit form):

$$f(\vec{v},\vec{x}) = A_{sys}\vec{x} - \vec{b} = 0$$

$$f(\vec{v},\vec{x}) = A_{sys} = \begin{bmatrix} x_1 - \bar{x} & y_1 - \bar{y} \\ x_2 - \bar{x} & y_2 - \bar{y} \\ . & . \\ . & . \\ x_n - \bar{x} & y_n - \bar{y} \end{bmatrix} \vec{x} - \begin{bmatrix} z_1 - \bar{z} \\ z_2 - \bar{z} \\ . \\ . \\ z_n - \bar{z} \end{bmatrix} = 0$$

where:

$$\vec{v} = [x_1\ y_1\ z_1\ x_2\ y_2\ z_2\ ...\ x_n\ y_n\ z_n]^T$$

$$\vec{x} = [A\ B]^T.$$

J_o is the partial derivative of f with respect to the output vector $\vec{x}$, and may be expressed as

$$J_o = \left[\frac{\partial f}{\partial \vec{x}}\right] = \left[\frac{\partial}{\partial \vec{x}}(A_{sys}\vec{x} - \vec{b})\right] = A_{sys}.$$

J_I is the partial derivative of f with respect to the input vector $\vec{v}$, and may be expressed as

$$J_I = \left[\frac{\partial f}{\partial \vec{v}}\right] = \left[\frac{\partial f}{\partial x_1}\frac{\partial f}{\partial y_1}\ \frac{\partial f}{\partial z_1}\ \ldots\ \ldots\ \frac{\partial f}{\partial x_n}\ \frac{\partial f}{\partial y_n}\ \frac{\partial f}{\partial z_n}\right]$$

To see how to fill its entries, consider the partial derivatives of the ith coordinate entry $(x_i\ y_i\ z_i)$:

$$\left[\frac{\partial f}{\partial x_i}\right] = \frac{\partial}{\partial x_i}\left(\begin{bmatrix} x_1 & y_1 \\ x_2 & y_2 \\ . & . \\ . & . \\ x_i & y_i \\ . & . \\ . & . \\ x_n & y_n \end{bmatrix}\begin{bmatrix} A \\ B \end{bmatrix}\right) = \begin{bmatrix} 0 & 0 \\ 0 & 0 \\ . & . \\ . & . \\ 1 & 0 \\ . & . \\ . & . \\ 0 & 0 \end{bmatrix}\begin{bmatrix} A \\ B \end{bmatrix} = \begin{bmatrix} 0 \\ 0 \\ . \\ . \\ A \\ . \\ . \\ 0 \end{bmatrix}$$

$$\left[\frac{\partial f}{\partial y_i}\right] = \frac{\partial}{\partial y_i}\left(\begin{bmatrix} x_1 & y_1 \\ x_2 & y_2 \\ . & . \\ . & . \\ x_i & y_i \\ . & . \\ . & . \\ x_n & y_n \end{bmatrix}\begin{bmatrix} A \\ B \end{bmatrix}\right) = \begin{bmatrix} 0 & 0 \\ 0 & 0 \\ . & . \\ . & . \\ 0 & 1 \\ . & . \\ . & . \\ 0 & 0 \end{bmatrix}\begin{bmatrix} A \\ B \end{bmatrix} = \begin{bmatrix} 0 \\ 0 \\ . \\ . \\ B \\ . \\ . \\ 0 \end{bmatrix}$$

$$\left[\frac{\partial f}{\partial z_i}\right] = \frac{\partial}{\partial z_i}\left(-\begin{bmatrix} z_1 \\ z_2 \\ . \\ . \\ z_i \\ . \\ . \\ z_n \end{bmatrix}\right) = \begin{bmatrix} 0 \\ 0 \\ . \\ . \\ -1 \\ . \\ . \\ 0 \end{bmatrix}$$

Therefore, the partial derivatives of f with respect to x_i, y_i, and z_i are column vectors with one nonzero entry in the ith position (A, B, -1, respectively), which means J_I may be expressed as

$$J_I = \begin{bmatrix} A & B & -1 & 0 & ... & & ... & & ... & & 0 \\ 0 & ... & 0 & A & B & -1 & 0 & ... & & ... & 0 \\ . & & & & & & & & & & 0 \\ 0 & ... & & ... & & ... & & 0 & A & B & -1 \end{bmatrix}$$

Finally, Σ_I is the variance-covariance matrix of all the inputs, i.e. all the coordinates, which may be expressed as:

$$\Sigma_I = \begin{bmatrix} \sigma_{x_1}^2 & \sigma_{x_1}\sigma_{y_1} & \sigma_{x_1}\sigma_{z_1} & ... & ... & \sigma_{x_1}\sigma_{z_n} \\ \sigma_{y_1}\sigma_{x_1} & \sigma_{y_1}^2 & \sigma_{y_1}\sigma_{z_1} & & ... & \sigma_{y_1}\sigma_{z_n} \\ \sigma_{z_1}\sigma_{x_1} & \sigma_{z_1}\sigma_{y_1} & \sigma_{z_1}^2 & & ... & \sigma_{z_1}\sigma_{z_n} \\ . & & & & & . \\ . & & & . & & . \\ . & & & & . & . \\ \sigma_{z_n}\sigma_{x_1} & \sigma_{z_n}\sigma_{y_1} & \sigma_{z_n}\sigma_{z_1} & ... & ... & \sigma_{z_n}^2 \end{bmatrix}.$$

Assuming the ith coordinate entry $(x_i\ y_i\ z_i)$ is independent of the jth coordinate entry $(x_j\ y_j\ z_j)$ for $i \neq j$, Σ_I reduces to

$$\Sigma_I = \begin{bmatrix} \sigma_{x_1}^2 & \sigma_{x_1}\sigma_{y_1} & \sigma_{x_1}\sigma_{z_1} & 0 & ... & & ... & 0 \\ \sigma_{y_1}\sigma_{x_1} & \sigma_{y_1}^2 & \sigma_{y_1}\sigma_{z_1} & 0 & ... & & ... & 0 \\ \sigma_{z_1}\sigma_{x_1} & \sigma_{z_1}\sigma_{y_1} & \sigma_{z_1}^2 & 0 & ... & & ... & 0 \\ 0 & 0 & 0 & . & & & & . \\ . & . & . & & & & & . \\ . & . & . & & . & & & 0 \\ . & . & . & & & \sigma_{x_n}^2 & \sigma_{x_n}\sigma_{y_n} & \sigma_{x_n}\sigma_{z_n} \\ . & . & . & & & \sigma_{y_n}\sigma_{x_n} & \sigma_{y_n}^2 & \sigma_{y_n}\sigma_{z_n} \\ 0 & 0 & 0 & & & \sigma_{z_n}\sigma_{x_n} & \sigma_{z_n}\sigma_{y_n} & \sigma_{z_n}^2 \end{bmatrix}.$$

Then, recognizing that the ith 3x3 block on the diagonal is the TPU matrix for the ith coordinate in the system of n equations, Σ_I may be expressed as

$$\Sigma_I = \begin{bmatrix} \Sigma_1 & & ... & 0 \\ . & \Sigma_2 & & . \\ . & & . & . \\ 0 & & ... & \Sigma_n \end{bmatrix},$$

where,

$$\Sigma_i = \begin{bmatrix} \sigma_{x_i}^2 & \sigma_{x_i}\sigma_{y_i} & \sigma_{x_i}\sigma_{z_i} \\ \sigma_{y_i}\sigma_{x_i} & \sigma_{y_i}^2 & \sigma_{y_i}\sigma_{z_i} \\ \sigma_{z_i}\sigma_{x_i} & \sigma_{z_i}\sigma_{y_i} & \sigma_{z_i}^2 \end{bmatrix}.$$

APPENDIX C

PERSPECTIVE TRANSFORMATION

To derive Equation 60, start by defining the following notation:

- (y, x) = pixel in the yth *row* and xth *column* in witness camera images
- $t_1 \ldots t_4$ are the true NED coordinates of the frame corners (1 = bottom left; 2 = top left; 3 = top right; 4 = bottom right)
- $t_i = [N_i \ E_i \ D_{frame}]^T$
- $c_1 \ldots c_4$ are the witness camera's pixels corresponding to frame corners 1-4
- $c_i = (row, column)$
- $x_\ell(y)$ is the pixel column corresponding to the frame's left edge in row y
- $x_r(y)$ is the pixel column corresponding to the frame's right edge in row y
- $\Delta_x(y)$ is the horizontal distance in pixels between the frame's left and right edges in row y
- $s_x(y)$ is a horizontal scaling function for coordinates in row y
- h is the number of pixels per meter in the horizontal direction at the frame's bottom edge

Using this notation, the Down coordinate may be expressed as

$$D = t_i(3) = D_{frame}.$$

The Northing coordinate may be expressed as

$$N = \underbrace{\frac{t_2(1) - t_1(1)}{c_2(1) - c_1(1)}}_{\text{slope}} y + \underbrace{t_2(1) - c_2(1)\frac{t_2(1) - t_1(1)}{c_2(1) - c_1(1)}}_{\text{intercept}}.$$

Equating this expression for N with Equation 60 yields

$$v_1 = \text{slope}$$

$$v_0 = \text{intercept}$$

The Easting coordinate is less straightforward because the horizontal perspective shrinks moving from the bottom to the top of the image. Consequently, the following functions are used to determine how much the perspective changes:

(1) In row y, the column containing the frame's left edge may be expressed as

$$x_\ell(y) = \frac{c_2(2) - c_1(2)}{c_2(1) - c_1(1)} y + c_1(2) - c_1(1)\frac{c_2(2) - c_1(2)}{c_2(1) - c_1(1)}.$$

(2) Similarly, the column containing the frame's right edge may be expressed as

$$x_r(y) = \frac{c_4(2) - c_3(2)}{c_4(1) - c_3(1)} y + c_3(2) - c_3(1)\frac{c_4(2) - c_3(2)}{c_4(1) - c_3(1)}.$$

(3) From these two equations, the horizontal distance in pixels between the frame's left and right edges in row y may be expressed as

$$\Delta_x(y) = x_r(y) - x_\ell(y).$$

(4) The horizontal scale factor, which determines how much horizontal coordinates shrink in the camera's perspective, may be expressed as

$$s_x(y) = \frac{\Delta_x(c_2(1))/\Delta_x(c_1(1)) - 1}{c_2(1) - c_1(1)} y + 1 - c_1(1) \frac{\Delta_x(c_2(1))/\Delta_x(c_1(1)) - 1}{c_2(1) - c_1(1)}.$$

(5) The conversion from pixels to meters at the frame's bottom edge may be expressed as:

$$h = \frac{c_4(2) - c_1(2)}{t_4(2) - t_1(2)} \text{ [pixels/m].}$$

(6) The horizontal distance in pixels from the frame's center to the laser's position, may now be expressed as

$$d_{center,beam}(y, x) = x - x_\ell(y) - \frac{\Delta_x(y)}{2}.$$

Using these functions, the Easting coordinate may then be expressed as

$$E = \frac{1}{h} \left(\frac{d_{center,beam}(y, x)}{s_x(y)} + x_\ell(y) - x_\ell c_1(1) + \frac{\Delta_x(y)}{2} \right) + t_1(2)$$

Equating this expression for E with Equation 60 yields

$$h_1 = \frac{1}{h s_x(y)}$$

$$h_0 = \frac{-(x_\ell(y) - \frac{\Delta_x(y)}{2})}{h s_x(y)} + \frac{x_\ell(y) - x_\ell c_1(1) + \frac{\Delta_x(y)}{2}}{h} + t_1(2)$$

Thus, the laser beam's NED coordinate computed from a witness camera image may be expressed as

$$\begin{bmatrix} N \\ E \\ D \end{bmatrix} = \begin{bmatrix} v_0 + v_1(y) \\ h_0 + h_1(x) \\ D_{frame} \end{bmatrix} = \begin{bmatrix} v_0 + v_1(row) \\ h_0 + h_1(col) \\ D_{frame} \end{bmatrix}$$

APPENDIX D

ACCUMULATOR ARRAY RESOLUTION

The following table contains the expected number of GmAPD measurements per accumulator array pixel for various combinations of array resolutions (rows) and camera FOVs (columns) for an airborne system.

Table 8: GmAPD measurements per accumulator array pixel

	9.4 mrad	**18.8 mrad**	**26 mrad**
2 x 2	75	37	24
3 x 3	33	16	11
4 x 4	18	9	6
5 x 5	12	6	3
6 x 6	8	4	2

These numbers were generated assuming the following:

1: Aircraft altitude = 400 m
2: Aircraft velocity = 50 m/s
3: 20 Hz $<$ Circular scan rate $<$ 40 Hz
4: Pointing vector is directly fore or aft
5: 20-degree off-nadir incidence
6: 10 kHz $<$ Pulse repetition rate $<$ 20 kHz
7: 7-mrad beam divergence
8: GmAPD camera's photon detection efficiency = 0.3
9: GmAPD FPA resolution = 32 x 32
10: 0.1-second wave epoch
11: Camera's entire FOV must encompass green footprint to register measurements

APPENDIX E

FLAT INTERFACE DSMS

Figure 69 shows Pathfinder's ability to reconstruct the water surface with 2x2 DSMs. Here, three side-view snapshots are shown of DSMs corresponding to 1.3 seconds, 4.7 seconds, and 8.2 seconds into the experiment. In all three cases, the DSM's mean water level is approximately 0.8-m Down and the OLS-computed surface normal is approximately $[0,0,-1]^T$. Figure 70 shows isometric, front, top, and side views of a 2x2 DSM corresponding to 3 seconds into the experiment. These figures are representative of all DSMs constructed during flat conditions. DSMs with other resolutions are shown in Appendix F.

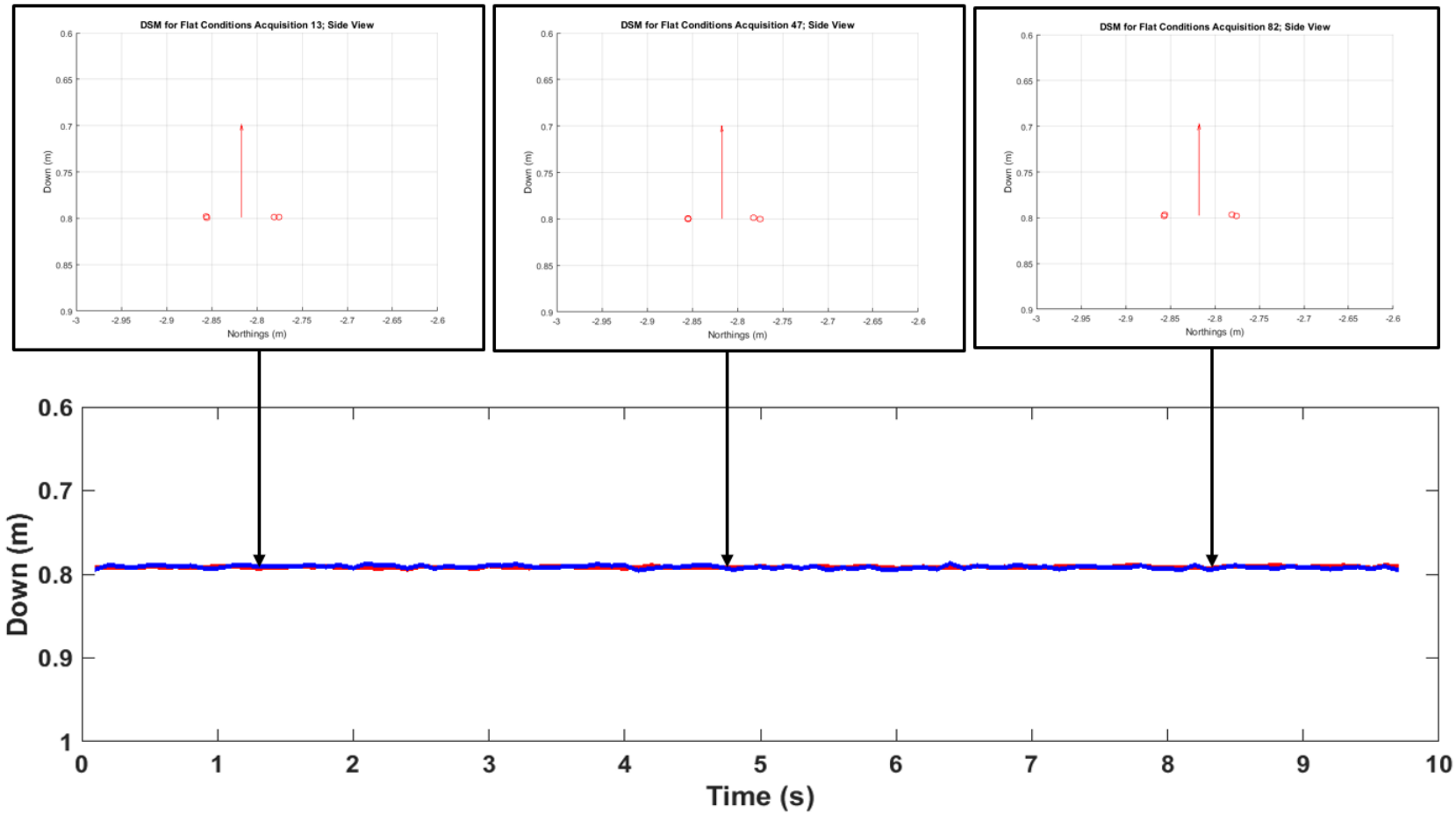

Figure 69: 2x2 DSMs constructed during flat conditions are shown corresponding to their acquisition time during the experiment.

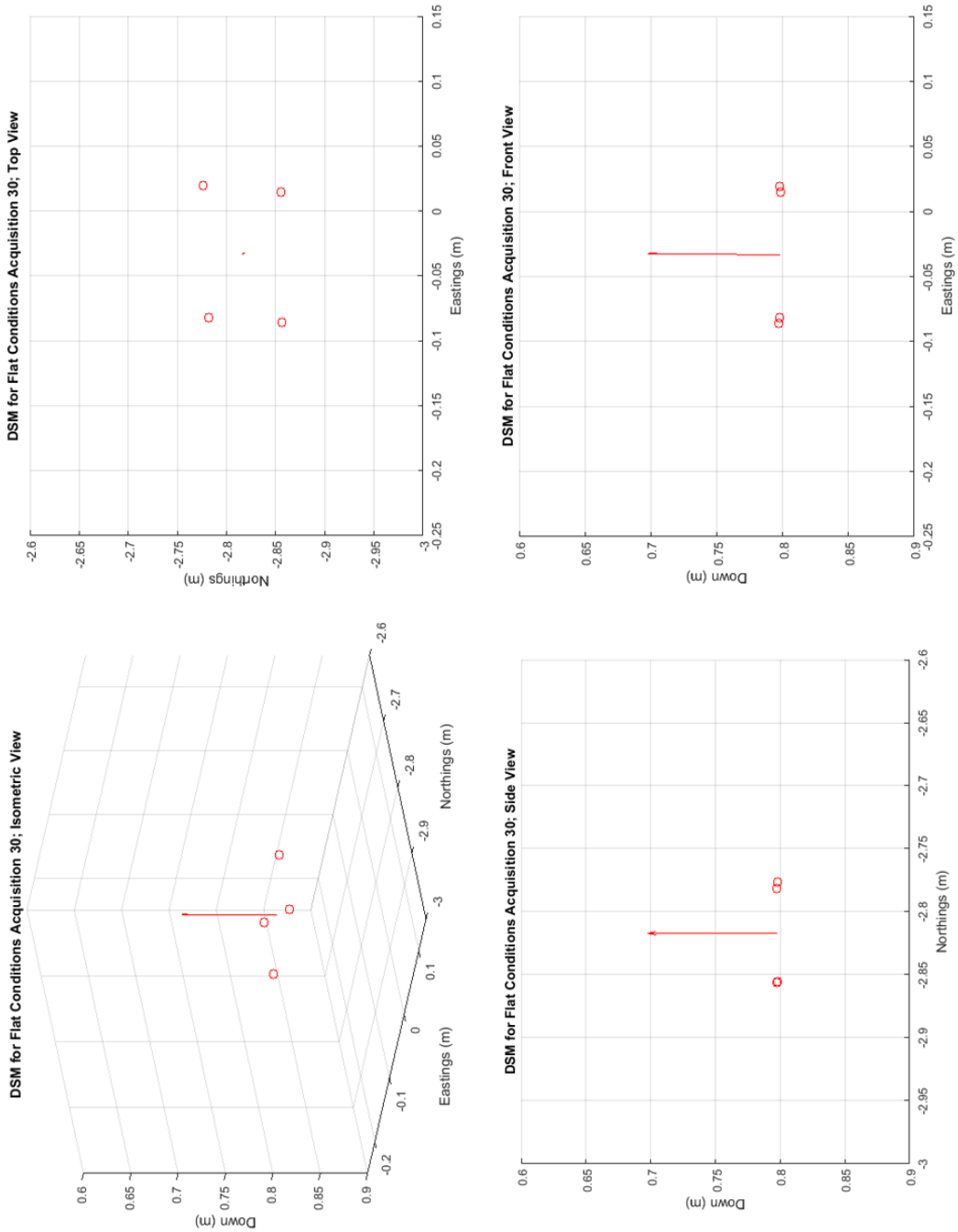

Figure 70: Isometric, top, front, and side views of a 2x2 DSM constructed during flat conditions.

APPENDIX F

WAVY INTERFACE DSMS

- Figure 71 shows Pathfinder's ability to reconstruct the water surface with 4x4 DSMs for File 1 waves. Three side-view snapshots are shown of DSMs corresponding to 2.3 seconds, 5.8 seconds, and 8.2 seconds into the experiment.

- Figure 72 shows Pathfinder's ability to reconstruct the water surface with 3x3 DSMs for File 2 waves. Three side-view snapshots are shown of DSMs corresponding to 2.3 seconds, 5.8 seconds, and 8.2 seconds into the experiment.

- Figure 73 shows Pathfinder's ability to reconstruct the water surface with 5x5 DSMs. Here, three side-view snapshots are shown of DSMs corresponding to 1.5 seconds, 5.6 seconds, and 8.5 seconds into the experiment.

These figures are meant to provide a representative visualization of DSM behavior during wavy conditions. DSMs are centered at the mean water level and have planar orientation corresponding to the wave's slope. For these figures, each surface-normal unit vector was computed with OLS. To gain a 3D perspective of the DSMs, Figure 74 shows isometric, front, top, and side views of a 6x6 DSM corresponding to the acquisition recorded 3 seconds into File 1.

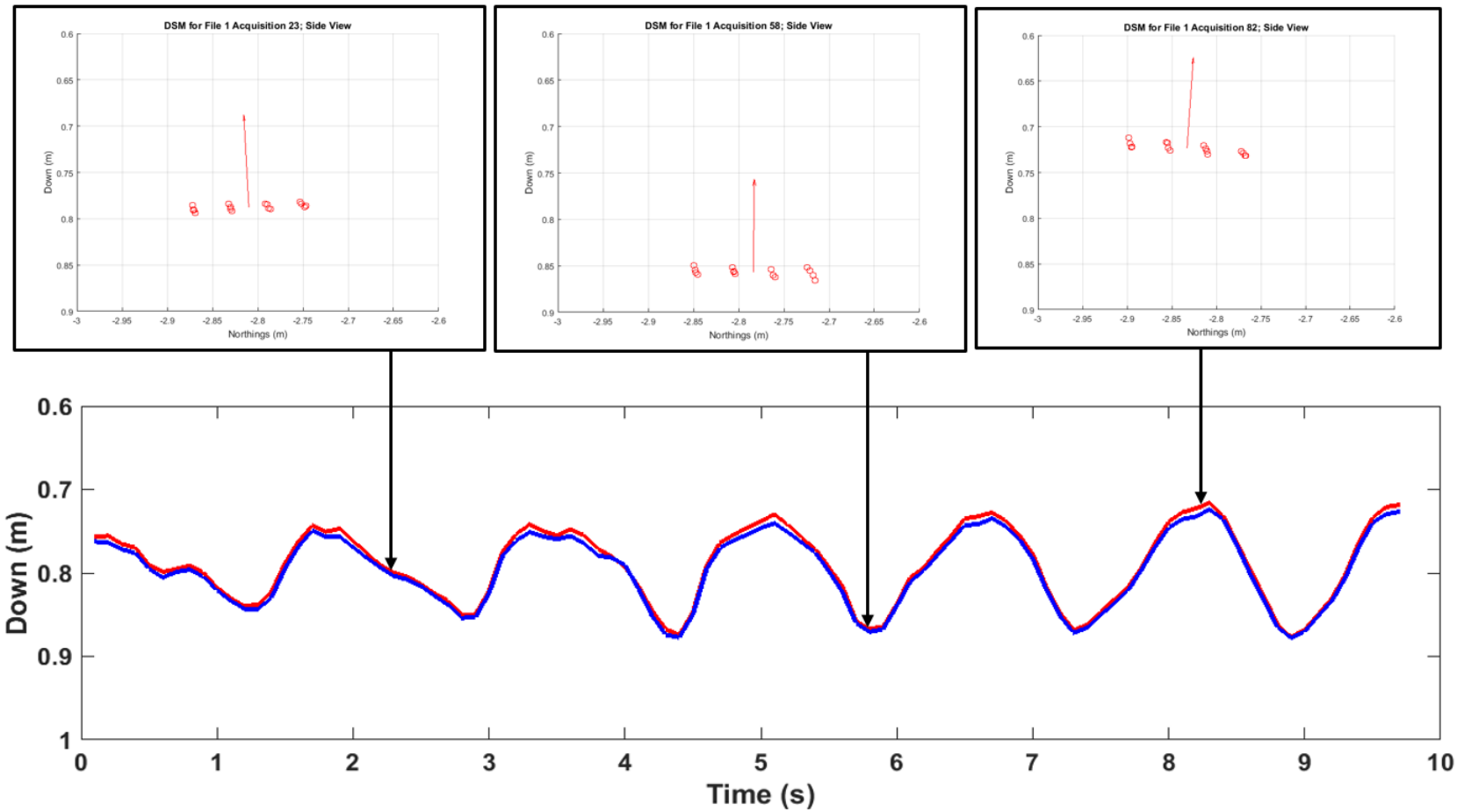

Figure 71: 4x4 DSMs constructed during wavy conditions are shown corresponding to their acquisition time during File 1.

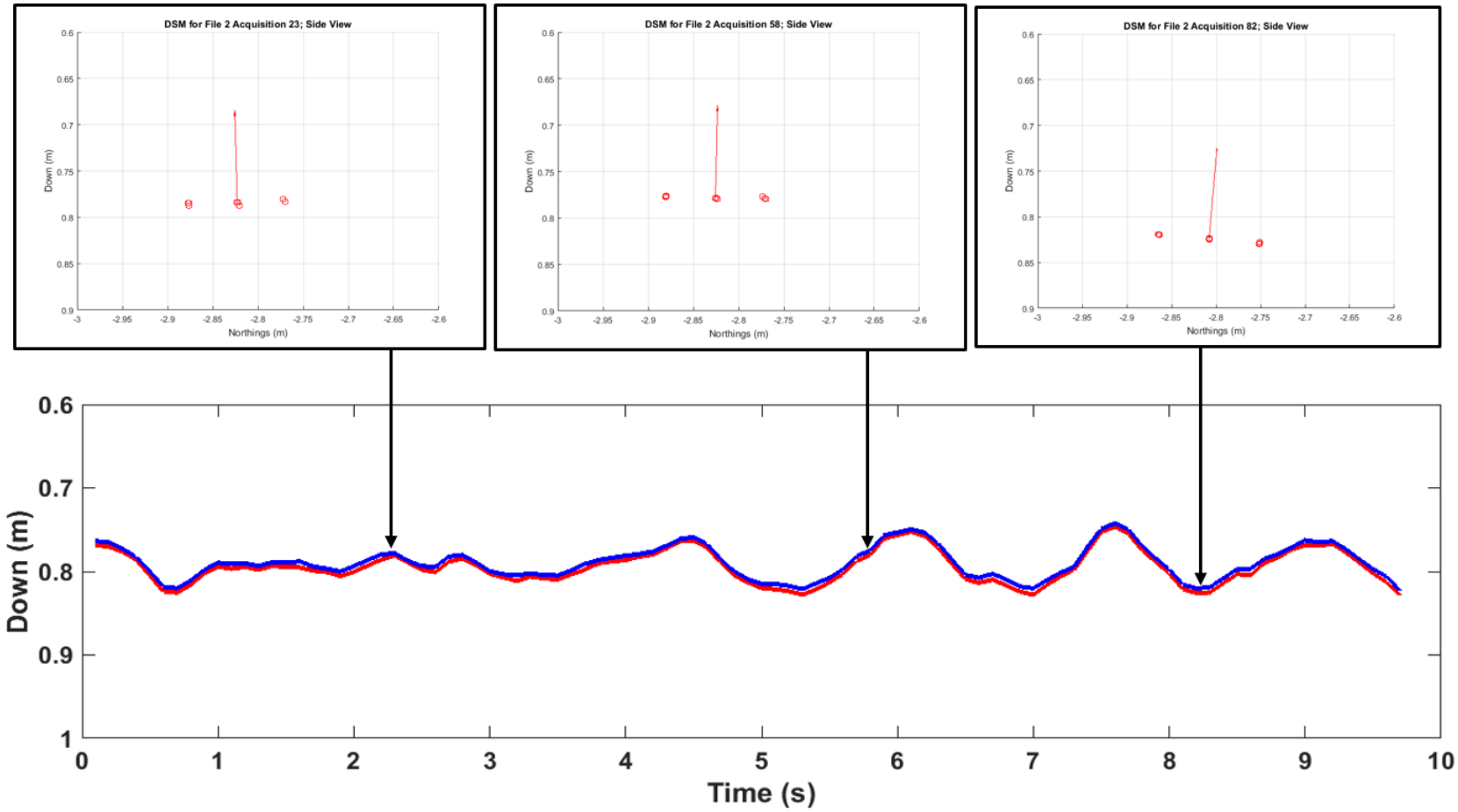

Figure 72: 3x3 DSMs constructed during wavy conditions are shown corresponding to their acquisition time during File 2.

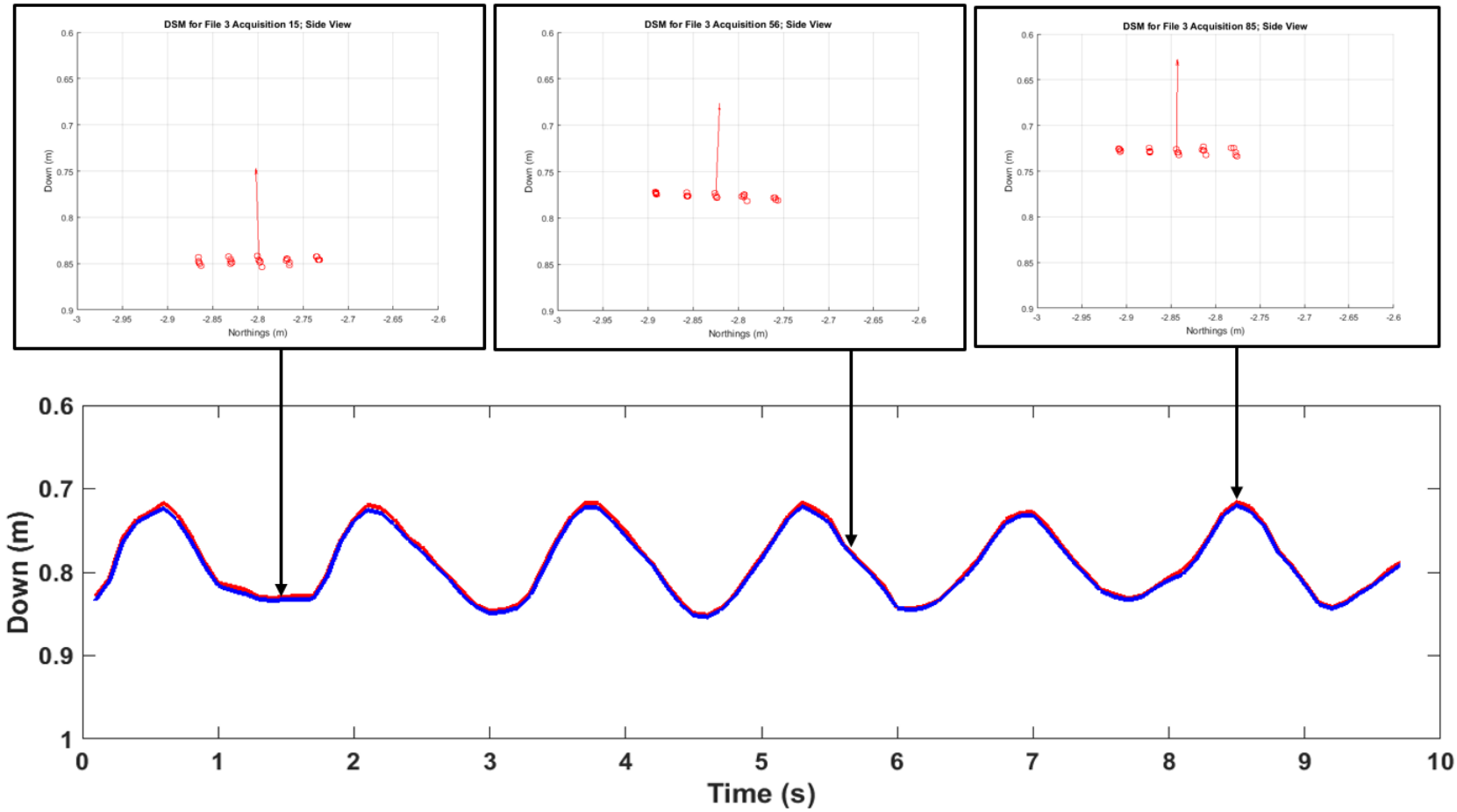

Figure 73: 5x5 DSMs constructed during wavy conditions are shown corresponding to their acquisition time during File 3.

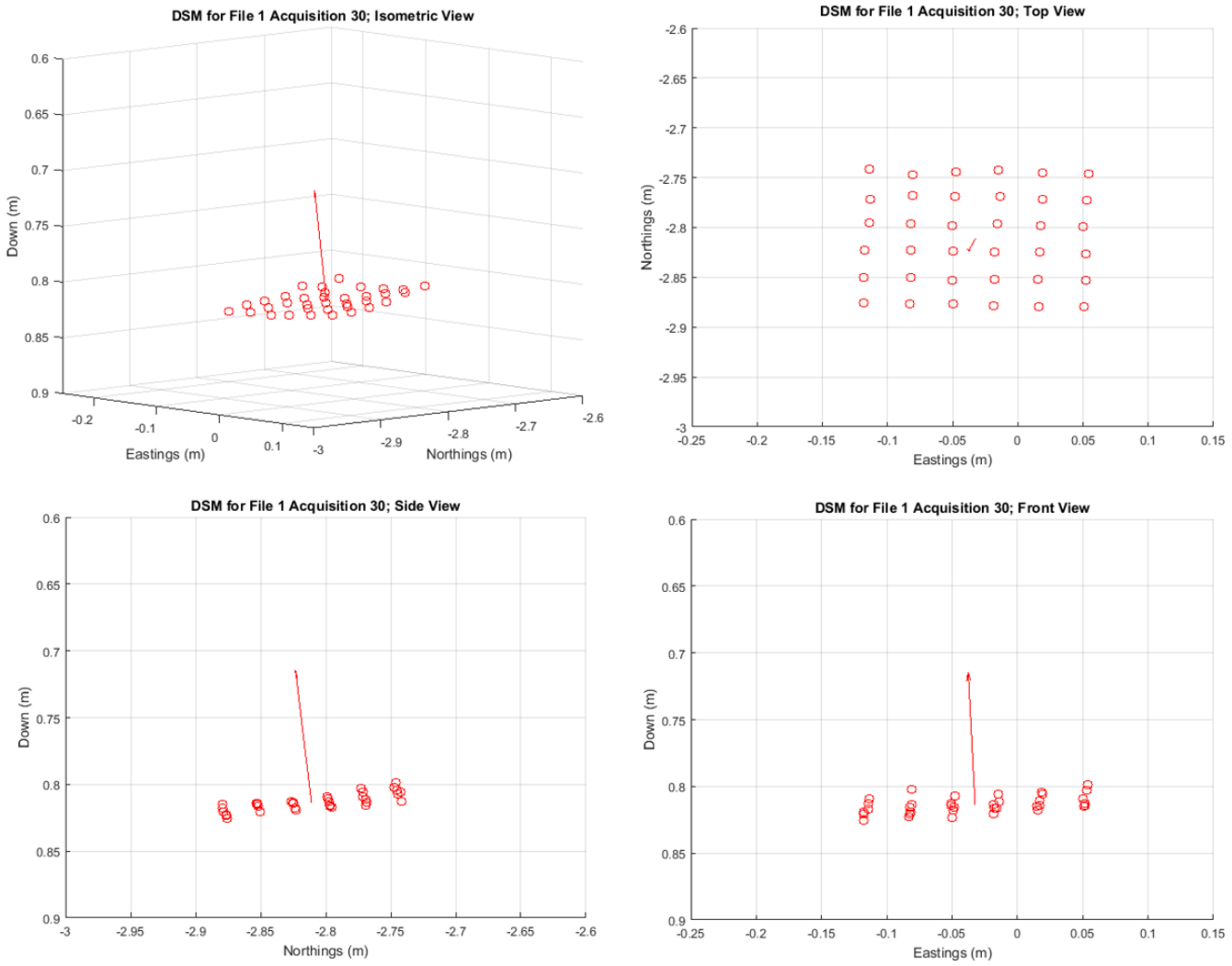

Figure 74: Isometric, top, front, and side views of a 6x6 DSM constructed during File 1 waves.

REFERENCES

[1] P. F. McManamon, G. Kamerman, and M. Huffaker, "A history of laser radar in the united states," in Proc. SPIE, vol. 7684, April 2010, pp. 76 840T–76 840T–11. [Online]. Available: http://dx.doi.org/10.1117/12.862562

[2] NASA, "Remote sensing and lasers," March 1998. [Online]. Available: http://www.nasa.gov

[3] G. Hickman and J. Hogg, "Application of an airborne laser for near-shore bathymetric measurements," Remote Sensing of the Environment, vol. 1, pp. 47–58, 1969.

[4] G. P. Sorenson, R. C. Honey, and J. R. Payne, "Analysis of the use of airborne laser radar for submarine detection and ranging," SRI Report No. 5583, 1966, (confidential).

[5] L. M. Ott, H. Krumboltz, and A. K. Witt, "Detection of submerged submarine by an optical ranging and detection system and detection of pulses by a submarine," Proc. 8th U.S. Navy Symp. of Military Oceanography, vol. 2, May 1971, (confidential).

[6] G. Guenther, "Meeting the accuracy requirements in airborne bathmetry." Dresden, Germany: Proceedings of the 20th EARSeL Symposium: Workshop on Lidar Remote Sensing of Land and Sea, June 2000.

[7] L. L. Cunningham, "Test report on pulsed light airborne depth sounder (plads)," Naval Oceanographic Office Tech. Note 6620-102-72, 1972.

[8] H. H. Kim, P. Cervenka, and C. Lankford, "Development of an airborne laser bathymeter," NASA Tech. Note TND-8079, 1975.

[9] M. Bristow, "Ccrs program," Laser Hydrography user requirements workshop minutes, January 1975.

[10] R. H. Abbot and M. F. Penny, "Air trials of an experimental laser bathymeter," Tech. Note WRE-TN-1509, 1975.

[11] J. Vosburgh and J. Banic, "Airborne laser surveys of the northwest passage," in Proc. XIIIth International Hydro. Conf., 1987.

[12] W. J. Lillycrop, L. E. Parson, L. L. Estep, P. E. LaRocque, G. C. Guenther, M. D. Reed, and C. L. Truitt, "Field testing of the u.s. army corps of engineers airborne lidar hydrographic survey system," in Proc. U.S. Hydro. Conf. '94, April 1994.

[13] C. Setter and R. J. Willis, "Lads - from development to hydrographic operations," in Proc. U.S. Hydro. Conf. '94, April 1994.

[14] K. Koppari, K. Karlsson, and U. Karlsson, "Airborne laser depth sounding in sweden," in International Hyddo. Rev. LXXI, vol. 2, 1994.

[15] P. E. LaRocque and G. R. West, "Airborne laser hydrography: an introduction," in Proc. ROPME/PERSGA/IHB Workshop on Hydrographic Activities in the ROPME sea area and Red Sea, 1999.

[16] N. Quadros, "Unlocking the characteristics of bathymetric lidar sensors," LiDAR Magazine, vol. 3, no. 6, pp. 62–67, 2013.

[17] G. C. Guenther, R. W. L. Thomas, and P. E. LaRocque, "Design considerations for achieving high accuracy with the shoals bathymetric lidar system," Proc. SPIE Laser Remote Sensing of Natural Waters: From Theory To Practice, vol. 2964, pp. 54–71, 1996. [Online]. Available: http://dx.doi.org/10.1117/12.258353

[18] G. C. Guenther, P. E. LaRocque, and W. J. Lillycrop, "Multiple surface channels in scanning hydrographic operational airborne lidar survey (shoals) airborne lidar," Proc. SPIE Ocean Optics XII, vol. 2258, pp. 422–430, 1994. [Online]. Available: http://dx.doi.org/10.1117/12.190084

[19] E. Yang, P. E. LaRocque, G. C. Guenther, D. Reid, W. Pan, and K. Francis, "Shallow water depth extraction - progress and challenges." Norfolk, Virginia: Proceedings of the 2007 U.S. Hydrographic Conference, 2007.

[20] M. P. Lee, "Benthic mapping of coastal waters using data fusion of hyperspectral imagery and airborne laser bathymetry," Ph.D. dissertation, University of Florida, 2003.

[21] G. H. Tuell, J. Y. Park, J. Aitken, V. Ramnath, V. Feygels, G. Guenther, and Y. Kopilevich, "Shoals-enabled 3d benthic mapping," vol. 5806. Proc. SPIE, 2005, pp. 816–826. [Online]. Available: http://dx.doi.org/10.1117/12.607010

[22] G. H. Tuell, "Counter mine lidar uav-based system (clubs), annual report for fy 2006." U.S. Navy, Office of Naval Research, 2006.

[23] G. H. Tuell and J. Y. Park, "Use of shoals bottom reflectance images to constrain the inversion of a hyperspectral radiative transfer model," vol. 5412. Proc. SPIE, 2004, pp. 185–193. [Online]. Available: http://dx.doi.org/10.1117/12.564929

[24] G. H. Tuell, J. Y. Park, J. Aitken, V. Ramnath, and V. Feygels, "Adding hyperspectral to charts: Early results," in Proc. US Hydrographic Conf, 2005.

[25] B. F. Aull, A. H. Loomis, D. J. Young, R. M. Heinrichs, B. J. Felton, P. J. Daniels, and D. J. Landers, "Geiger-mode avalanche photodiodes for three-dimensional imaging," Lincoln Laboratory Journal, vol. 13, no. 2, pp. 335–349, 2002.

[26] M. Fuller, "Airborne lidar geiger mode vs traditional linear," April 2015, (Presentations APSG 33). [Online]. Available: http://www.apsg.info

[27] R. M. Marino and W. R. Davis, "Jigsaw: a foliage-penetrating 3d imaging laser radar system," Lincoln Laboratory Journal, vol. 15, no. 2, pp. 335–350, 2005.

[28] G. Tuell, K. Barbor, and J. Wozencraft, "Overview of the coastal zone mapping and imaging lidar (czmil): a new multisensor airborne mapping system for the u.s. army corps of engineers," in Proc. SPIE, vol. 7695, pp. 76 950R–76 950R–8. [Online]. Available: http://dx.doi.org/10.1117/12.851905

[29] A. Payment, V. Feygels, and E. Fuchs, "Proposed lidar receiver architecture for the czmil system," in Proc. SPIE, vol. 7695, 2010, pp. 76 950Y–76 950Y–9.

[30] A. Ekelund, "Topo/bathy lidar lidar sensors and applications." 15th Annual JALBTCX Airborne Coastal Mapping and Charting Workshop, June 2014.

[31] E. Fuchs and A. Mathur, "Utilizing circular scanning in the czmil system," in Proc. SPIE, vol. 7695, 2010, pp. 76 950W–76 950W–10. [Online]. Available: http://dx.doi.org/10.1117/12.851936

[32] "Iho standards for hydrographic surveys, 5th edition," Special Publication No. 44, February 2008.

[33] D. A. Carr and G. H. Tuell, "Estimating field-of-view loss in bathymetric lidar: application to large-scale simulations," Appl. Opt., vol. 53, no. 21, pp. 4716–4721, July 2014.

[34] "Light detection and ranging (lidar) sensor model supporting precise geopositioning," NGA Standardization Document, August 2011.

[35] G. H. Tuell, "Counter mine lidar uav-based system (clubs) - year 2 (extended)." U.S. Navy, Office of Naval Research, 2007.

[36] V. I. Feygels, J. Y. Park, J. Aitken, M. Kim, A. Payment, and V. Ramnath, "Coastal zone mapping and imaging lidar (czmil): first flights and system validation," in Proc. SPIE, vol. 8532, 2012, pp. 85 321C–85 321C–10. [Online]. Available: http://dx.doi.org/10.1117/12.2007325

[37] G. C. Guenther, Airborne laser hydrography: system design and performance factors. Rockville, MD: U.S. Dept. of Commerce, National Oceanic and Atmospheric Administration, National Ocean Service, Charting and Geodetic Services, 1985.

[38] N. Jerlov, Marine Optics, ser. Elsevier Oceanography Series. Elsevier Science, 1976. [Online]. Available: https://books.google.com/books?id=tzwgrtnW_lYC

[39] J. M. Wozencraft, "Requirements for the coastal zone mapping and imaging lidar (czmil)," in Proc. SPIE, vol. 7695, 2010, pp. 76 950Q–76 950Q–7. [Online]. Available: http://dx.doi.org/10.1117/12.851891

[40] J. W. Pierce, E. Fuchs, S. Nelson, V. Feygels, and G. Tuell, "Development of a novel laser system for the czmil lidar," in Proc. SPIE, vol. 7695, 2010, pp. 76 950V–76 950V–6. [Online]. Available: http://dx.doi.org/10.1117/12.851933

[41] K. J. Petri, "Laser radar reflectance of chesapeake bay waters as a function of wind speed," in IEEE Transactions on Geoscience Electronics, vol. 15, no. 2, April 1977, pp. 87–96.

[42] Y. I. Kopilevich, V. I. Feygels, and A. I. Surkov, "Mathematical modeling of input signals for oceanographic lidar systems," in Proc. SPIE, vol. 5155, 2003, pp. 30–39. [Online]. Available: http://dx.doi.org/10.1117/12.506980

[43] Y. I. Kopilevich and A. G. Surkov, "Mathematical modeling of the input signals of oceanological lidars," J. Opt. Technol., vol. 75, no. 5, pp. 321–326, May 2008. [Online]. Available: http://jot.osa.org/abstract.cfm?URI=jot-75-5-321

[44] V. I. Feigels, B. Evans, L. Feygels, G. C. Guenther, and Y. I. Kopilevich, "Prediction of bathymetric lidar performance with ocean scientific 2001 simulation code," in Proc. SPIE, vol. 4488, 2002, pp. 61–70. [Online]. Available: http://dx.doi.org/10.1117/12.452826

[45] G. H. Tuell, V. Feygels, Y. Kopilevich, A. D. Weidemann, A. G. Cunningham, R. Mani, V. Podoba, V. Ramnath, J. Y. Park, and J. Aitken, "Measurement of ocean water optical properties and seafloor reflectance with scanning hydrographic operational airborne lidar survey (shoals): Ii. practical results and comparison with independent data," in Proc. SPIE, vol. 5885, pp. 58 850E–58 850E–13. [Online]. Available: http://dx.doi.org/10.1117/12.619215

[46] R. L. Ortman, D. Carr, R. James, D. Long, M. O'Shaughnessy, C. R. Valenta, and G. H. Tuell, "Real-time, mixed-mode computing architecture for waveform-resolved lidar systems with total propagated uncertainty," in Proc. SPIE Laser Radar Technology and Applications XXI, vol. 9832, 2016.

[47] I. P. Diabin, B. M. Golubitskii, V. V. Bacherikov, V. E. Kagain, and I. A. Makarov, "Use of logarithmic fast-response photodetector in optical radar," Soviet Journal of Optical Technology, vol. 46, pp. 36–38, Jun. 1979.

[48] E. Fuchs and G. Tuell, "Conceptual design of the czmil data acquisition system (das): integrating a new bathymetric lidar with a commercial spectrometer and metric camera for coastal mapping applications," in Proc. SPIE, vol. 7695, 2010, pp. 76 950U–76 950U–12. [Online]. Available: http://dx.doi.org/10.1117/12.851919

[49] G. Tuell, R. James, R. Ortman, C. Valenta, D. Carr, and J. Zutty, "Qualification testing of the agilent m9703a digitizer for use in a bathymetric lidar," in Geoscience and Remote Sensing Symposium (IGARSS), 2014 IEEE International, July 2014, pp. 2703–2705.

[50] D. A. Carr, "A study of the target detection capabilities of an airborne lidar bathymetry system," Master's thesis, Georgia Institute of Technology, 2013.

[51] N. Pfeifera and C. Briese, "Geometrical aspects of airborne laser scanning and terrestrial laser scanning," International Archives of Photogrammetry, Remote Sensing and Spatial Infromation Sciences, vol. 36, pp. 311–319, 2007.

[52] C. Parrish, "Lidar 101," August 2011, lidar and Height Mod Workshop, Silver Spring, MD.

[53] Y. I. Kopilevich, V. I. Feygels, G. H. Tuell, and A. Surkov, "Measurement of ocean water optical properties and seafloor reflectance with scanning hydrographic operational airborne lidar survey (shoals): I. theoretical background," in Proc. SPIE, vol. 5885, 2005, pp. 58 850D–58 850D–9. [Online]. Available: http://dx.doi.org/10.1117/12.618923

[54] M. Lee and G. Tuell, "A technique for generating bottom reflectance images from shoals data." Biloxi, MS: U.S. Hydrographic Conference, 2003.

[55] G. H. Tuell and J. Y. Park, "Use of shoals bottom reflectance images to constrain the inversion of a hyperspectral radiative transfer model," in Proc. SPIE, vol. 5412, 2004, pp. 185–193. [Online]. Available: http://dx.doi.org/10.1117/12.564929

[56] J. Y. Park, V. Ramnath, V. Feygels, M. Kim, A. Mathur, J. Aitken, and G. Tuell, "Active-passive data fusion algorithms for seafloor imaging and classification from czmil data," in Proc. SPIE, vol. 7695, 2010, pp. 769 515–769 515–10. [Online]. Available: http://dx.doi.org/10.1117/12.851991

[57] V. Ramnath, V. Feygels, Y. Kopilevich, J. Y. Park, and G. Tuell, "Predicted bathymetric lidar performance of coastal zone mapping and imaging lidar (czmil)," in Proc. SPIE, vol. 7695, 2010, pp. 769 511–769 511–12.

[58] S. Peeri, J. V. Gardner, L. G. Ward, and J. R. Morrison, "The seafloor: A key factor in lidar bottom detection," IEEE Transactions on Geoscience and Remote Sensing, vol. 49, no. 3, pp. 1150–1157, March 2011.

[59] G. H. Tuell, "Toward real-time total propagated error in bathymetric lidar." 14th Annual JALBTCX Airborne Coastal Mapping and Charting Workshop, August 2013.

[60] I. NovAtel, "Gps position accuracy measures," December 2003. [Online]. Available: http://www.novatel.com/assets/Documents/Bulletins/apn029.pdf

[61] C. Mobley, Light and Water: Radiative Transfer in Natural Waters. San Diego, CA: Academic, 1994.

[62] H. M. Tulldahl and K. O. Steinvall, "Simulation of sea surface wave influence on small target detection with airborne laser depth sounding," Appl. Opt., vol. 43, no. 12, pp. 2462–2483, Apr 2004.

[63] S. Kizilkaya, "Optical propagation through the ocean surface," Master's thesis, Pennsylvania State University, 2012.

[64] H. Abdallah, N. Baghdadi, J.-S. Bailly, Y. Pastol, and F. Fabre, "Wa-lid: A new lidar simulator for waters," Geoscience and Remote Sensing Letters, IEEE, vol. 9, no. 4, pp. 744–748, 2012.

[65] T. Allouis, J.-S. Bailly, and D. Feurer, "Assessing water surface effects on lidar bathymetry measurements in very shallow rivers: a theoretical study." Geneva, Switzerland: Proceedings of the Second Space for Hydrology Workshop, November 2007.

[66] N. J. Guida, "A new technique for 3d modeling of water surfaces using a geiger-mode receiver," Master's thesis, Georgia Institute of Technology, 2015.

[67] M. A. Itzler, M. Entwistle, X. Jiang, M. Owens, K. Slomkowski, and S. Rangwala, "Geiger-mode apd single-photon cameras for 3d laser radar imaging," in 2014 IEEE Aerospace Conference, March 2014, pp. 1–12.

[68] D. G. Fouche, "Detection and false-alarm probabilities for laser radars that use geiger-mode detectors," Appl. Opt., vol. 42, no. 27, pp. 5388–5398, Sep 2003. [Online]. Available: http://ao.osa.org/abstract.cfm?URI=ao-42-27-5388

[69] Z. Zhang, Y. Zhao, Y. Zhang, L. Wu, and J. Su, "A real-time noise filtering strategy for photon counting 3d imaging lidar," Opt. Express, vol. 21, no. 8, pp. 9247–9254, Apr 2013. [Online]. Available: http://www.opticsexpress.org/abstract.cfm?URI=oe-21-8-9247

[70] H. Badino, D. Huber, Y. Park, and T. Kanade, "Fast and accurate computation of surface normals from range images," in Robotics and Automation (ICRA), 2011 IEEE International Conference on, May 2011, pp. 3084–3091.

[71] R. B. Rusu, "Semantic 3d object maps for everyday manipulation in human living environments," Ph.D. dissertation, Computer Science department, Technische Universitaet Muenchen, Germany, October 2009.

[72] A. S. Glassner, Ed., An Introduction to Ray Tracing. London, UK, UK: Academic Press Ltd., 1989.

[73] G. C. Guenther and R. W. Thomas, "Effects of propagation-induced pulse stretching in airborne laser hydrography," in Proc. SPIE, vol. 0489, 1984, pp. 287–296.

[74] J. Chen, Z. Ding, and F. Yuan, "Theoretical uncertainty evaluation of stereo reconstruction," in 2008 2nd International Conference on Bioinformatics and Biomedical Engineering, May 2008, pp. 2378–2381.

[75] G. D. Leo, C. Liguori, and A. Paolillo, "Propagation of uncertainty through stereo triangulation," in Instrumentation and Measurement Technology Conference (I2MTC), 2010 IEEE, May 2010, pp. 12–17.

[76] S. Harsdorf and R. Reuter, "Stable deconvolution of noisy lidar signals," in Proc. of EARSeL-SIG-Workshop LIDAR, no. 1, 2000, pp. 88–95.

[77] J. Wu, J. van Aardt, and G. P. Asner, "A comparison of signal deconvolution algorithms based on small-footprint lidar waveform simulation," in IEEE Transactions on Geoscience and Remote Sensing, vol. 49, no. 6, June 2011, pp. 2402–2414.

VITA

Domenic Anthony Carr was born in Alexandria, Virginia to Todd and Tori Carr. After graduating as a Valedictorian from Hayfield Secondary School in 2007, he enrolled at the University of Virginia. He then received his B.S. in Electrical and Computer Engineering (ECE) and an Economics minor in 2011, and was awarded the William L. Everitt Student Award of Excellence upon graduation. He began his graduate studies at Georgia Tech in August 2011, serving as a graduate research assistant in the Electro-Optical Systems Laboratory at Georgia Tech Research Institute. After receiving his M.S. in ECE in May 2013, he decided to pursue his Ph.D in ECE. During the next three years, he worked on active electro-optical intelligence, surveillance, and reconnaissance research projects primarily under the supervision of Dr. Grady Tuell. He was a member of the Dr. Tuell-led team that won GTRI's IRAD of the year in 2013. He was also an active member of the OSA and SPIE student chapters, serving as SPIE President for 1 year and Vice President for 2 years.